BEHAVIOUR OF ACCESSORY MONAZITE AND AGE SIGNIFICANCE DURING METAMORPHISM AND PARTIAL MELTING DURING GRENVILLE OROGENY: AN EXAMPLE FROM OTTER LAKE AREA, CENTRAL METASEDIMENTARY BELT, QC

A thesis submitted to the

Faculty of Graduate and Postdoctoral Studies

In partial fulfillment of the requirements for the

Master of Science Degree in Earth Sciences

Ottawa – Carleton Geoscience Centre

Department of Earth Sciences

Faculty of Science

University of Ottawa

ABSTRACT

The accretionary Mesoproterozoic Grenville Orogeny (ca. 1300 – 980 Ma) involving the Central Metasedimentary Belt is a key building block of the eastern Laurentian margin. A petrographic, mineralogical, geochemical and geochronological study of the migmatite complex in Otter Lake (QC) within the Marble Domain is used to resolve regional metamorphic and magmatic events primarily recorded in the leucosome accessory minerals (i.e. monazite). The relationship between the different stages of monazite and garnet growth and dissolution during the tectonic evolution of the orogenic history for the interpreted metasomatic (injected) and anatectic (in situ) monazite-bearing neosomes from this study supports published thermochronological work in the area and challenges the claim that the Central Metasedimentary Belt was not heated above 500 °C during the Ottawan phase. Instead, the region shows Grenville magmatic and anatectic events were overprinted by high-temperature, fluid-rich Ottawan-phase metamorphism recorded within both injected (monazite-bearing) and in situ (monazite- and garnet-bearing) neosomes.

EXTENDED ABSTRACT

A detailed petrographic, mineralogical, geochemical and geochronological study of three rock suites within the Marble Domain of the Central Metasedimentary Belt in Quebec (CMB-Q) is used to place age constraints on regional metamorphic and magmatic events primarily recorded in the leucosome accessory minerals (i.e. monazite). The three rocks suites include (1) amphibolite with associated diorite migmatite, (2) K-feldspar gneiss and (3) stromatic Grt-Bt-Sil gneiss. The peraluminous S-type neosomes include the calc-alkaline injected neosomes and shoshonitic in situ neosomes from Suites 1 and 3, respectively. Based on field and petrographic results the allanite- and titanite-bearing diatexite K-feldspar lacks monazite. For this reason emphasis was placed on the monazite-bearing samples. The injected (granodiorite and quartz-monzonite from Suites 1 and 3, respectively) neosomes are typical of magmas originating from convergent margins ascribed to the release of (K, LILE and LREE)-rich fluids with partial melting from the crustal slab whereas the in situ (garnet quartz-monzonite and garnet monzonite, Suite 3) neosomes are metasomatized mantle-derived metapelites.

91 *in situ* U-Th-Pb EMPA chemical ages from 22 monazites within four samples were collected: injected and in situ neosomes from Suites 1 and 3. Three texturally distinct injected and in situ monazite domains have been identified: leucosome, matrix and inclusions in garnet (in situ neosomes). Furthermore, two types of geochemically distinct monazites have been recognized (1) (Th + LREE)-rich injected neosomes formed during melt recrystallization reflecting the alkaline nature and presence of an external source (i.e. Chevreuil and Kensington-Skootamatta plutons along the N-S trending Cayamant Deformation Zone) or from the breakdown of phosphate minerals and (2) (Y + HREE)-rich in situ neosomes formed at the expense of Y and HREE released from garnet dissolution.

Garnet mineral chemistry from three in situ neosome samples within Suite 3 shows two geochemically distinct almandine-rich garnet types (Grt1 and Grt 2). Grt1 is more pyrope-rich

relative to the almandine- and spessartine-rich Grt2. Reverse rimward zoning (Mg, Fe and/or Mn) due to diffusional exchange and/or network transfer reactions between garnet and biotite during cooling and retrograde metamorphism.

Monazite U-Th-Pb geochronology data reveal that this area was affected by numerous magmatic and anatectic events during the tectonic evolution of the Grenville Orogeny. Garnet growth was initiated at or after ca. 1218 Ma during regional prograde metamorphism marking the end of the Elzevir Orogeny. The large, porphyroblastic (Grt1) garnets formed during regional peak Shawinigan metamorphism at ca. 1155 ± 14 Ma (Th- and LREE-rich monazite). Upon cooling, garnet growth ceased and/or broke down releasing Y + HREE back into system, coeval with the end of the Shawinigan Orogeny at ca. 1136 ± 16 Ma (Y- and HREE-rich monazite). The younger ca. 1063 ± 6 Ma (Y- and HREE-rich monazite) is coeval with the emplacement of the Kensington-Skootamatta plutons.

Both Grt1 and to a greater extent Grt2 (which are thought to have grown at same time as Grt1) were reset during peak Ottawan phase metamorphism at ca. 1048 ± 10 Ma recorded in the Th- and LREE-rich monazite. The ca. 1048 ± 10 Ma monazite crystallization age represents the high-temperature (650 – 700 °C) peak Ottawan metamorphism. The younger ca. 1014 – 942 Ma monazite ages from the in situ (Y- and HREE-rich monazite) neosomes can be attributed to extensive hydrothermal alteration related to crystallization in the upper crust after significant exhumation and cooling during orogenic collapse (ca. 1020 Ma).

ACKNOWLEDGEMENTS

I owe many thanks to Dr. David. A. Schneider for taking me on as one of his own students and helping me through this process. I truly appreciate everything you have done for me. Thank you! I would like to thank Dr. Richard Cox for giving me the opportunity to pursue my M.Sc. at the University of Ottawa and for funding for this project through the Natural Sciences and Engineering Research Council of Canada (NSERC) and the University of Ottawa.

I appreciate the help and support from everyone in the Department of University of Ottawa throughout this process, including Patricia Rasmussen (Health Canada Research Chair) and Mark Chenier (Research Associate) for ICP-MS. I owe a special thank you to Peter Jones (Carleton University) and Glenn Poirier (University of Ottawa) for their assistance with microprobe data collection, your time and insight is very much appreciated.

I must also mention the following people for their knowledgeable advice during this journey: Dr. Bill Arnott, Dr. Fred Gaidies, Dr. Paula Piilonen, and Amanda Van Lankvelt. I thank all my colleagues here at the University of Ottawa and those at Carleton University for making this a memorable experience- one that I shall never forget.

Many friends have helped me through these difficult years. Their support and care helped me overcome setbacks and stay focused on my graduate studies. I greatly value their friendship and I deeply appreciate their belief in me.

My extended family has aided and encouraged me through this endeavour. A special acknowledgement to one of the strongest women I have come to know and admire, Madeleine Séjourné. Merci Grand-Maman chérie d'amour!

But above all, none if this would have been possible without the love, patience, and support from my immediate family Michel, Michelle and Marc-André (Dré) Séjourné, to whom I dedicate this thesis. You have been a constant source of love, support, strength and encouragement all these years. Thank you for staying by my side and for cheering me on through this journey. Thank you for being you and for making me a better me, love you more!

TABLE OF CONTENTS

LIST OF FIGURES

LIST OF TABLES

APPENDICES

Figures

Tables

CHAPTER 1: INTRODUCTION

Most collision zones involve slices of continental crust that have been reworked during several, possibly unrelated, episodes. Rocks of the Grenville Orogenic cycle in North America are interpreted to have resulted from Himalayan-style collision between Laurentia and another continent, probably Amazonia, at ca. 1100 Ma (Hynes and Rivers 2010). The exposed late Mesoproterozoic rocks represent the products of a long-lived continental-margin and associated back arc as well as remnants of one or more accreted island-arc terranes (Hynes and Rivers 2010). Evidence for the late Mesoproterozoic accretionary Grenville Orogen (ca. 1300 – 980 Ma) lies within the Central Metasedimentary Belt (CMB) which was a key building block of the eastern Laurentian margin (Rivers 1997). During the later metamorphic episodes, relics of the early history are progressively erased. Moreover, according to authors such as Beaumont et al. (2006) and Rivers (2008a), the ca. 100 Ma duration of the collisional Grenvillian Orogeny make it a large, hot, long-duration orogen, and, since much of the orogen is deeply eroded, it provides an excellent opportunity to study the nature of processes in the deep crust.

Widespread middle to lower crustal metamorphism and anatexis typically result from large-scale continental collisions (Brown 2001). This large-scale rearrangement of mass and heat during orogeny consequently exerts a strong influence on metamorphism, deformation, melting and magmatism (Brown 2001). The resulting heterogeneous crustal architecture preserved in many metamorphic terranes is important for characterization of exposed middle crust anatectic migmatites (Brown 2001). The formation of anatectic migmatites with pelitic and/or volcanic protoliths involves mainly mica dehydration-melting reactions, with or without fluid influx, and retrograde reactions (e.g. Spear et al. 1999; Milord et al. 2001). Melt segregation from the site of partial melting is followed either by in situ crystallization or by the

later fractional crystallization and mobilization of melts with more evolved compositions (Milord et al. 2001). The study of these corresponding processes is of particular interest because of their inferred role as a geochemical and geochronological link between high-grade metamorphism and the generation of large-scale granitic bodies (e.g. Solar and Brown 2001).

A comprehensive understanding of the link between high-grade anatexis of the Grenville Orogen and the subsequent generation of large-scale bodies requires not only good geological data but also precise geochronological control on the texturally-defined age of events and the rates and durations of associated igneous, metamorphic, and deformation processes (e.g. Corriveau et al. 1990; Corriveau and Gorton 1993; Corriveau and van Breeman 2000; Kennedy et al. 2010; Schneider et al. 2013). Igneous and metamorphic rocks contain abundant minerals, for example monazite, which may be used to elucidate petrogenetic and geochronological histories (e.g. Montel 1993, 2000; Crowley et al. 2005).

Monazite, a light-rare earth (LREE) phosphate accessory mineral, of low abundance and small size (Parrish 1990), occurs in a wide range of rocks, including high-grade metamorphic gneisses, metaluminous to peraluminous granites, metapelites, and pegmatites (Overstreet 1967; Spear and Pyle 2002), which are consistent with rocks observed in the Central Metasedimentary Belt in Québec (CMB-Q). Multiple age and/or compositional domains can be preserved within a single thin section; even within a single grain preserving the complex geological history (Dahl et al. 2005). Fluid-related coupled dissolution-reprecipitation processes can modify the composition and reset the U-Th-Pb geochronometer of monazite and other orthophosphate minerals (Pyle and Spear 2003; Williams and Jercinovic 2002). Because Pb diffusion in monazite is slow (e.g. Cherniak et al. 2000), the composition and texture of each monazite generation may reflect geological processes active at the time of monazite formation (Williams

et al. 2007). Thus, monazite geochemistry and geochronology can shed light on the prograde and retrograde history of a wide range of rocks, including those observed in the CMB-Q (Suzuki and Adachi 1991; Montel et al. 1996; Cocherie et al. 1998).

Migmatite terranes, like the Otter Lake area in the Marble Domain of the CMB-Q in the Grenville Province (Figure 1), represent exposed middle orogenic crust that exhibits evidence of melting and melt segregation expressed as heterogeneous rocks composed of different parts: paleosome (protolith) and neosome (leucosome and melanosome), the latter formed by partial melting (e.g. Sawyer 2008). Further evidence of melting and melt segregation is demonstrated in the form of intrusive granitoids, formed from the partial melting of surrounding host rocks, these dikes, sills, and batholiths form as a result of melt trapped during migration to shallower levels (Brown 2007). Corriveau and Leblanc (1995) proposed that plastic marble-rich country rock in the CMB-Q favoured ponding of K-rich magmas to form composite plutons at midcrustal levels. Thus, the Otter Lake area serves as a natural laboratory in which the effects of partial melting of middle and lower orogenic crust can be observed directly, resulting in the characterization of melts originating from orogenic and/or magmatic sources via *in situ* or from an external (injected) partial melting and/or fractional crystallization.

In this study petrographic, mineralogical, geochemical and geochronological information from migmatites and granitic rocks from the Otter Lake area are studied in order to determine host rock protoliths, constrain the age of metamorphic (anatectic) and/or magmatic events that should be recorded mostly in the accessory minerals (i.e. monazite) of the neosome portions of the rock. The monazite-bearing neosome crystallization ages using U-Th-Pb electron microprobe analysis (EMPA) chemical dating was chosen because this *in situ* analytical technique is inexpensive, fast, and non-destructive of textural relationships (Harrison et al.

2002), analysis of different chemical and/or age domains within an individual grains is feasible and can be coupled with their textural petrographic characteristics (e.g. Montel et al. 1993; Catlos et al. 2002).

Mineral analyses of garnet and monazite were performed because garnet and monazite are the major repositories of HREE and Y (Kohn et al. 2005). When monazite contains relatively abundant HREE and Y it can suggest: (1) monazite started to grow before garnet growth, (2) garnet growth ceased while monazite growth persisted or (3) garnet broke down during prograde or retrograde reactions releasing these elements for monazite formation (e.g. Spear and Pyle 2002; Kohn and Malloy 2004). Since Y can be measured with the EMP, analysis of Y can provide insight into the relationship between monazite relative to garnet growth and/or consumption (Pyle et al. 2001, Williams et al. 2007).

This study summarizes the chemical and textural features of the monazite and garnet. Combining these data with U-Th-Pb EMP ages from different monazite generations permits the unravelling of the relationships between granitoids and amphibolites, diorite migmatites and pelitic gneisses in the Otter Lake study area. Additionally, this study demonstrates the interplay between magmas of both crustal and mantle-derived provenances via processes of anatexis (partial melting) and magma differentiation (crystal fractionation).

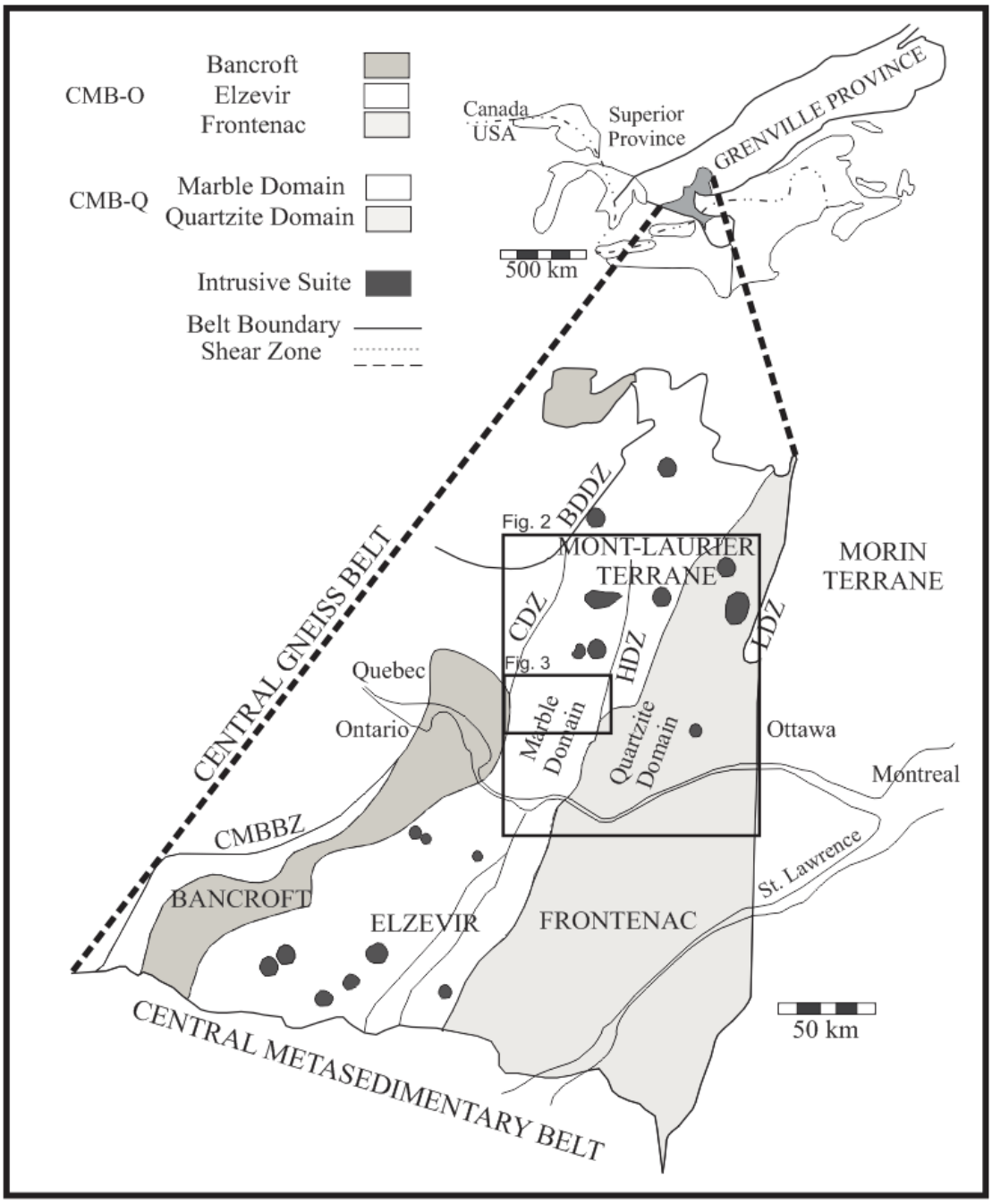

Figure 1: Geological map of southwestern Grenville Province showing the location of terranes and domains in the Central Metasedimentary Belt (CMB). The deformation zones are the BDDZ Baskatong-Désert; CMBBZ, Central Metasedimentary Belt boundary zone; CDZ, Cayamant; HDZ, Heney; and LDZ, Labelle. Magmatic corridors in Québec (CMB-Q) are defined in text, here defined as the (Kensington) intrusive suite. The study area, in Otter Lake (Fig. 3), within the Marble domain (modified from Corriveau et al. 1998). Boxes outline the Central Metasedimentary Belt in Québec (CMB-Q; Figure 2) and the studied Otter Lake area within the Marble Domain of the CMB-Q (Figures 3).

CHAPTER 2: GRENVILLE PROVINCE IN SOUTHERN CANADA

The southwestern part of the Grenville Province in Ontario and Québec is characterized by intense deformation, mainly upper amphibolite and lower granulite polyphase metamorphism associated with northwest-directed thrusting of accretionary rocks (Busch et al. 1997; Ketchum et al. 1998; Carr et al. 2000; Indares et al. 2000; Boggs and Corriveau 2004). The Mesoproterozoic evolution of the convergent Grenville orogeny (ca. 1300 – 950 Ma; Davidson 1995) within the western Grenville Province is marked by three main metamorphic events (Elzevir, Shawinigan and Grenvillian), although these events are not necessarily orogen-wide (Rivers 2008). The metavolcanic and metasedimentary rocks with abundant marble in the CMB-Q mark the onset of the first orogenic pulse beginning with tholeiitic to calc-alkaline volcanism and sedimentation from the early Elzevir Orogeny (Moore and Thompson 1980), from 1245 – 1220 Ma (Heumann et al. 1986; van Breeman and Davidson 1989; Corriveau et al. 1990). The volcanic rocks that comprise the CMB formed outboard of Laurentia at ca. 1280 – 1270 Ma and their formation was approximately coeval with that of related sedimentary basins. These arcs were amalgamated during the Elzevir orogeny, to form the CMB (Carr et al. 2000). The pulse of gabbroic and granitic plutonism at this time is believed to have stitched the different arc fragments in the CMB (Carr et al. 2000).

The second metamorphic event is marked by the beginning of convergent high P-T regional (peak) metamorphism that affected the whole area during the Shawinigan Orogeny (1190 – 1140 Ma) (Corrigan and van Breeman 2000; Carr et al. 2000). Peak metamorphism was recorded to be around 950°C based on orthopyroxene-garnet thermometer and ~ 10 kbar from Al in orthopyroxene and garnet-aluminosilicate-silica-plagioclase barometers (Boggs 1996) in the Mont-Laurier terrane (Tollo et al. 2004).

The third metamorphic event is the Grenvillian Orogeny which includes the Ottawan phase (1090 – 1020 Ma) and the Rigolet phase (1005-980 Ma) (Rivers 1997; Rivers et al. 2002). Widespread upper amphibolite- to granulite-facies metamorphism and partial melting (1050 – 1000 Ma; Carr et al. 2000) are associated with the Ottawan phase (Slagstad et al. 2005). According to Carr et al. (2000), the terranes were accreted to, and in some cases obducted onto the Laurentian margin. The accreted terranes underwent Himalayan-style orogenesis during the Ottawan phase of the Grenvillian orogeny (Carr et al. 2000; Rivers 2008; Rivers 2012). The Rigolet phase occurred near the northwestern margin of the Grenville Front, the lowest unit in the orogenic stack recorded in the Central Gneiss Belt (CGB) (Wynne-Edwards 1972; Rivers et al. 2002; Rivers 2008, 2009, 2012). The CGB, to the west, contains parauchthonous low- to medium-pressure amphibolite- and granulite-facies assemblages (Rivers 2008) defining a final contractional pulse (ca. 1010 – 980 Ma), ending with extensional collapse at ca. 1020 Ma (McLelland et al. 2010).

In the case of the Grenville Province, compressional Ottawan normal-sense displacement was initiated and the shear zones became listric in the mid crust (Rivers 2008, 2012). Younger accreted terranes, such as the Marble-Domain of the Mont-Laurier terrane in the CMB-Q, that lacks evidence for penetrative Grenvillian metamorphism and deformation, except in their basal shear zones, define the orogenic lid (Rivers 2009). The orogenic lid of the Grenville Province occurs in two areas: 1) in the northeast, and 2) in the southwest, including part of the CMB (including the CMB-Q) (Rivers 2008).

Rivers (2008) claims the CMB-Q was not heated above ca. 500 °C during the Ottawan phase interpreted as part the orogenic lid, but a recent study by Schneider et al. (2013) noted that there exists portions of the orogenic suprastructure that were unusually warm (>500 °C) but did

not undergo significant Grenvillian penetrative deformation. An approach to determine the early Grenvillian tectonics from the geology of the CMB-Q in the Otter Lake area involves the identification of the Chevreuil and the Kensington-Skootamatta intrusive suites as chronometric field markers for documentation of the site, style of emplacement, and degree of deformation of these plutonic bodies relative to the metamorphic conditions preserved in the host rocks (Corriveau and van Breeman 2000). Furthermore, the nature of emplacement of the Chevreuil and Kensington-Skootamatta suites can be used as strain markers for this portion of the orogenic lid and as such, help constrain the nature of emplacement for the leucosomes as forming either via partial melting or via magmatic injection into the rocks of the marble-domain along the Cayamant deformation zone (CDZ) to the west of the Mont-Laurier terrane in the CMB-Q.

Relationship between the Cayamant Deformation Zone and the Chevreuil and Kensington-Skootamatta Magmatic Suites

The Central Metasedimentary Belt (CMB) in southern Ontario and Québec consists of several fault-bounded domains and terranes, each with their own distinctive magmatic history and stratigraphy (Wynne-Edwards 1972; Carr et al. 2000; Corriveau and van Breeman 2000). The lithological boundary separating the western-side of the CMB-Q (Fig. 2) in the Mont-Laurier terrane (Marble Domain) is abrupt and marked by the N-S trending CDZ (Corriveau et al. 1996). At depth, the CDZ is defined as the SE-dipping, crustal scale Baskatong ramp, interpreted as a suture accommodating strain during and after accretion of the CMB-Q (Martignole et al. 2000; Blein et al. 2003).

During the polyphase-reactivation history of the Grenville province (e.g. Elzevir, Shawinigan and Grenvillian), syn- to post-tectonic magmatism consistent with a post-collisional intraplate extensional magmatic event, between the peak Shawinigan metamorphism and the

onset of the Grenville orogeny, is represented by the onset of the sheet-like arrays of monzonite, diorite, and gabbro intrusions of the 1170 – 1160 Ma and Chevreuil magmatism in the CMB-Q (Rivers 1997; Corriveau and van Breeman 2000). The subcircular, crescent-shaped, K-rich 1089-1076 Ma alkaline rocks from the Kensington-Skootamatta suite are characterized by syenite plutons including biotite-rich monzonite, diorite, pyroxenite, and skarns that define the magmatic corridor along these north-trending shear zones (Corriveau et al. 1990, 1994; Corriveau and Gorton 1993; Corriveau and Morin 2000; Fig. 1). Corriveau and Leblanc (1995) debated that the K-rich alkaline plutons would not be present in the CMB-Q had it not been for the presence of marble, a cap being required to force these low viscosity, hot magmas to pond, a heat source required to promote partial melting and anatexis in the CMB-Q.

Geology of the Otter Lake area, Québec

The study area includes parts of the western and central Marble Domain within the CMB-Q, Figure 3. Rocks in the Otter Lake area are dominated by mafic to felsic metavolcanic rocks, clastic metasedimentary and marble rocks that define the principal supracrustal rocks in the CMB along with geochemically distinct suites of plutonic rocks (Hynes and Rivers 2010).

The metamorphic grade across the central Marble Domain was estimated to be dominantly upper amphibolite facies with local granulite facies (orthopyroxene in gneiss and amphibolite) during the Elzevir and Ottawan phases of the Grenville Orogeny (Kretz 1994; Kretz et al. 1999). Max P-T estimates are variably reset during the 1190 – 1140 Ma Shawinigan orogenic event to equilibration conditions given below (Corriveau and van Breeman 2000; Boggs and Corriveau 2004). Kretz (1994, 1997 and 2007) indicated temperature and pressure estimates of 700 ± 50 °C and 7 ± 0.5 kbar in addition to Perkins et al. (1982) who gave similar metamorphic condition estimates 650 - 700 °C and 5 - 7 kbar.

Bimodal U-Pb zircon and monazite age populations on selected migmatites were obtained via LA-ICPMS from the Marble and Quartzite Domains at ca. 1230 Ma and 1180 - 1140 Ma implying that the metamorphism and anatexis took place during the accretionary Shawinigan Orogeny preserved in the leucosomal portions of the migmatite populations (Schneider et al. 2013). Barfod et al. (2005) interpreted a Lu-Hf isotopic age of 1031 ± 6 Ma from apatite from the nearby Yates mine to represent the age of peak Ottawan-phase metamorphism and corresponds to 650-700 °C under fluid-rich conditions. Kennedy et al. (2010) recorded two younger thermal ion mass spectrometry (TIMS) titanite ages from the Yates Uranium prospect at 1014.8 ± 2.0 Ma and 998.0 ± 4.5 Ma from a Ca-Ti skarn, consistent with post-peak formation. Only a few studies (e.g. Barfod et al. 2005; Kennedy et al. 2010; Schneider et al. 2013) before this study recorded metamorphic REE-phosphate geochemistry and geochronology to resolve the timing of these polyphase metamorphic events with reference to textural microstructures and host rock protoliths within the Otter Lake area of the CMB-Q.

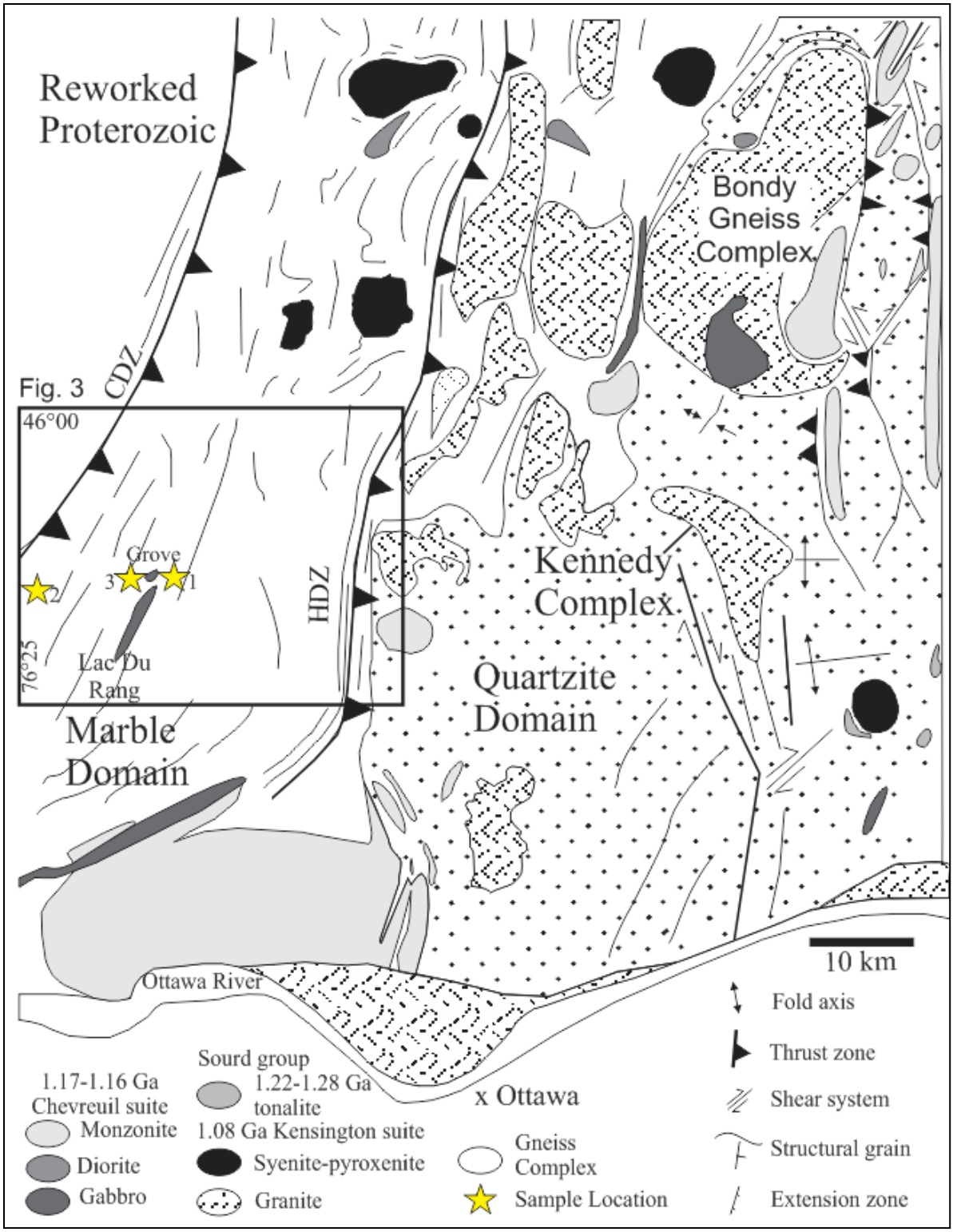

Figure 2: Geological map of the Central Metasedimentary Belt in Québec within the Grenville Province showing the distribution of plutons and gneiss complexes in the Marble and Quartzite domains (modified from Corriveau et al. 1998). Kensington–Skootamatta intrusive plutons and dykes are undeformed whereas the Chevreuil suite plutons (e.g. Lac du Rang in the Otter Lake study area) are elongated. The studied outcrop locations (1-3) represented by stars in the box.

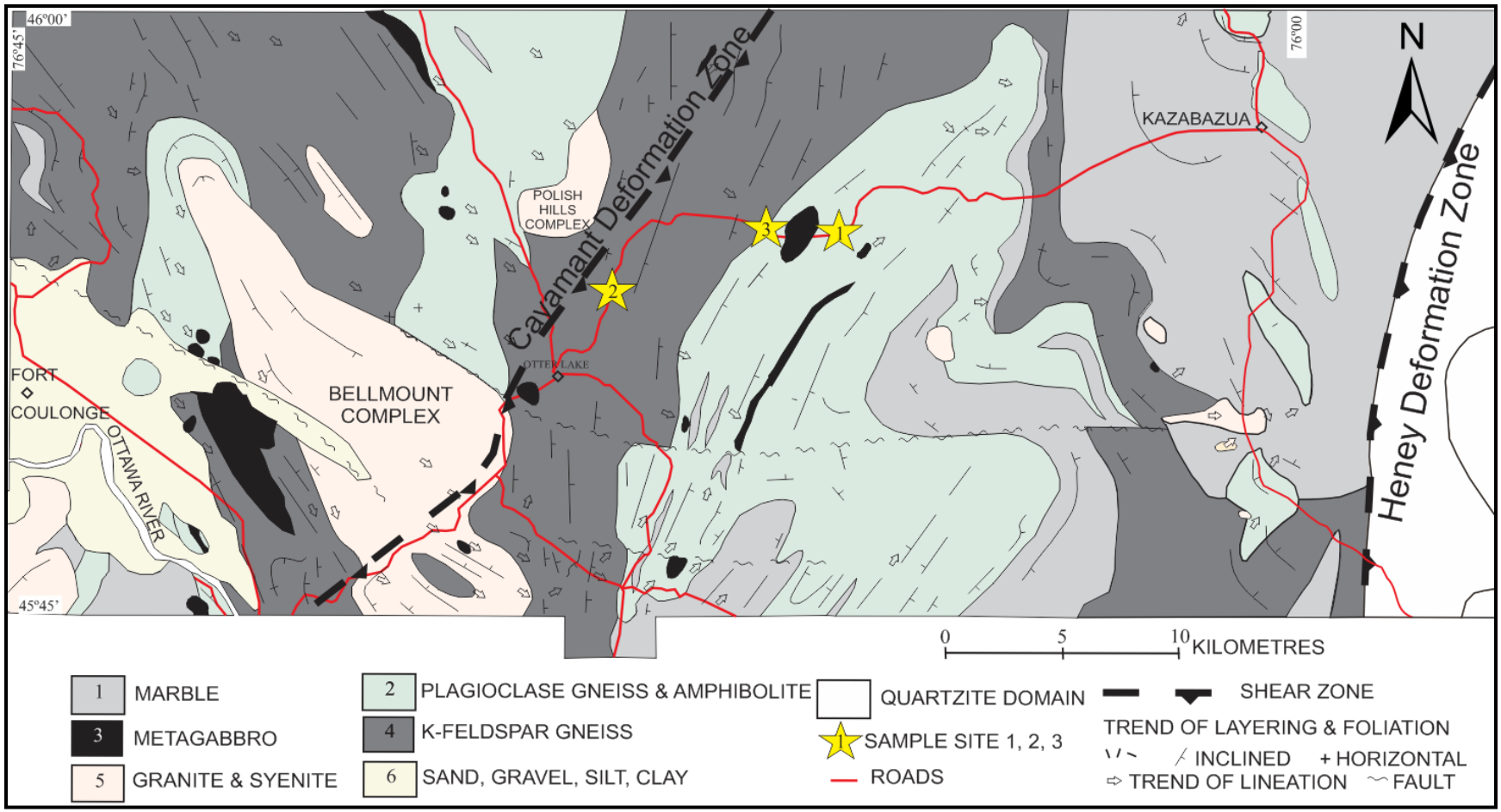

Figure 3: Geological map of the Otter Lake area in the Marble-Domain of the Central Metasedimentary Belt in Québec showing sample locations for each studied outcrop (1-3), modified after Kretz (1977, 1990). Group 1: marble and skarn, 2: felsic and mafic gneiss, amphibolite, granulite, quartzite, with combinations of sillimanite, garnet, hornblende, clinopyroxene, orthopyroxene, representing a sequence of interlayered clastic sedimentary and volcanic rock, 3: metagabbro, 4: K-feldspar gneiss, mainly veined gneiss, and 5: granitic and syenitic rock ranging from granodiorite to nepheline syenite (Kretz 1959; 1978; 1980; 1990; 1994a; 2005; 2007; Kretz et al. 1989a).

CHAPTER 3: METHODS

Field and Petrographic Methods

Representative samples from three outcrops were taken along road transects off Highway 301 between Otter Lake and Danford Lake, QC (Table A1). Samples were divided into groups based on outcrop location and subsequently defined as 'suite' of rocks. Representative polished thin sections (30 μm thick) were made based on textural and lithological variation which could then be analyzed under the optical microscope and electron microprobe (EMP). Before using the electron microprobe, a petrographic study of the three suites was conducted using petrographic techniques.

Whole-rock Analysis

The analysis of whole-rock samples, using glass discs, for x-ray fluorescence (XRF) analysis was carried out to investigate the bulk chemical analyses of major (Si, Ti, Al, Fe, Mn, Mg, Ca, Na, K, and P) and trace (Cr, V, Ni, Rb, Sr, Ba, Y, Zr, Nb, Pb, Th and U) elements, whereas inductively coupled plasma mass spectrometer (ICP-MS) methods were applied for rare earth element (REE; La-Lu) analyses using pressed pellets.

In order to do this, samples were crushed using a steel-jaw crusher then pulverized to a fine, homogeneous powder in an agate ring mill for major and minor element geochemical XRF analyses on thirteen hand samples; Suite 1 (n = 5), Suite 2 (n = 3) and Suite (n = 5), which were fused into glass discs using the Claisse at the University of Ottawa with a 4:1 ratio of tetrahydroborate to sample rock powder. The samples were bombarded using a high power X-ray tube, where secondary x-rays (fluorescent) emitted by the sample determined the elements present. Estimated two-sigma (2σ) uncertainty on major element oxides is ± 2 - 4% of the values measured.

The pulverized rock samples were sent to the University of Toronto, briquetted into pressed pellets bound by a small amount of resin for heavy element analysis (above Iron) using methods outlined by Longerich (1993). The pressed pellets were dissolved in poly-carbonate tubes using warm aqua-regia on a block heater for three days. The silicate precipitate was centrifuged and the clear liquid sample was extracted using a precision pipette and diluted using 1% HNO_3 containing In, Rh and Bi which were used as internal standards. Trace element concentrations were analyzed on a Perkin Elmer DRC ICP-MS at the Geobiology and Health Lab at the University of Ottawa using methods outlined by Longerich et al. (1990, 1993). The 2σ uncertainty is estimated at ± 5 - 10% for trace elements, and ~10% for each REE. Results for both XRF and ICP-MS are presented and discussed in Chapter 5.

Electron Microprobe Analysis

Mineral analyses of garnet and monazite were performed to determine compositional elemental changes in order to obtain estimates for metamorphic conditions and to further correlate these changes with observed petrographic textures. Garnet analyses were performed at the University of Ottawa whereas monazite mineral and geochronology analyses were performed at Carleton University. Thin sections were washed to remove impurities (i.e. grease from fingerprints) and carbon coated. Prior to analysis, digital BSE (back-scattered electron) images were collected at 512 x 512 pixel resolution with an Electron Optic Services digital imaging system consisting of a 4Pi Analysis Inc. Specimens were also examined with an EDX system to confirm mineral identifications (i.e. distinguish monazite from zircon).

Garnet Analysis

Quantitative analyses of major and trace elements (Si, Ti, Al, Fe^{2+}, Mn, Mg, Ca, Na, K, P and Y) in garnets were made on an automated 5 spectrometer JEOL 8230 SuperProbe electron

microprobe by the wavelength dispersive X-ray analysis method (WDX), raw data included in enclosed CD-ROM (Appendix III). Operating conditions were 20kV accelerating voltage, 20 nA beam current for oxides and silicates and the common matrix ZAF corrections were applied. Counting times were 10-20 seconds. Background measurements were made at 50% peak counting time on each side of the analyzed peak. Background positions were carefully selected to avoid instances of peak overlap. Composition was analyzed along a rim-to-rim line transect through garnet with a 10 μm step size in order to evaluate compositional zoning. Garnet end-member compositions (almandine, grossular, pyrope and spessartine) were measured, whereas andradite was calculated using the measured stoichiometry from the data. A suite of well characterized natural and synthetic minerals and compounds were used as calibration standards for garnet EMP analysis (Tables A3 and Table A4).

Monazite Analysis

Quantitative electron microprobe spot analyses of monazite major and minor element (P, Ca, Si, Ce, La, Nd, Pr, Sm, Eu, Gd, Tb, Dy, Ho, Er, Tm, Yb, Lu, Th, Y, U, Sr, and Fe) concentrations from four thin sections were carried out using the automated 4 spectrometer Cameca Camebax MBX electron probe by the wavelength dispersive X-ray analysis method (WDX). Operating conditions were 20kV accelerating voltage and 20 nA beam current for oxides and silicates. Specimens were analyzed using a rastered electron beam 5x5 to 10x10 microns in size. Counting times were 15-60 seconds or 40,000 accumulated counts. Background measurements were made at 50% peak counting time on each side of the analyzed peak. To avoid or minimize instances of elemental peak overlap, background x-ray lines were chosen following the procedures outlined by Exley (1980), Roeder (1985), and Scherrer (2000). Raw x-ray data were converted to elemental weight percent (wt %) by the Cameca PAP matrix

correction program (Pouchou and Pichoir 1991). A suite of well characterized natural and synthetic minerals and compounds were used as calibration standards, given in Table A2. Results are presented in both wt % and cations per 4.00 atoms of oxygen as atoms per formula unit (apfu) summarized in Tables 5 and 6. Monazite from the granodiorite (Suite 1) and quartz-monzonite (Suite 3) samples are presented in Table 5 whereas the garnet-bearing (quartz-) monzonite (Suite 3) samples are presented in Table 6.

It should be stressed that careful electron microprobe analysis for REE involves a considerable investment of time and energy if the analytical levels are below 1 wt %. At levels of 0.1 to 1 wt %, the analytical results are still reasonably good, but the problems of overlap correction and background measurement become increasingly important at the lower levels. The problem of accurate measurement of background (Parrish 1990) and overlap correction for concentrations less than 0.1 wt % are very significant, and results at this level should be viewed with scepticism.

Electron microprobe chemical analyses of U, Th, and Pb on monazites provides an *in situ*, non-destructive method of dating individual domains that also offer the geochronological advantages of high spatial resolution and small analytical volume. It is assumed that monazite is initially rich in U and Th but lacks initial Pb, also known as common Pb. Common Pb is incorporated into the crystal lattice at the time of crystallization. This is especially common with monazite (Parrish 1990).

Monazites selected for chemical U-Th-Pb geochronological dating were analyzed at 15 kV, 70 nA with a rastered electron beam 5x5 to 10x10 microns in size. The elements Th, U, Pb and Y were measured simultaneously and were the only elements measured. PAP matrix corrections were carried out using an average monazite composition for elements other than Th,

U and Pb using the Cameca Trace program (Montel et al. 1996). At the beginning of each analytical session (i.e. each time a monazite calibration is made), at least one and in most case, several standard grains were dated along with the unknown grains. These standard grains were analyzed every couple of unknown chemical age (Table A5 and Table A6) for which trace element compositions and the geological age have been constrained independently and ratios concordant.

Apparent U-Th-Pb chemical ages were derived from measured U:Th:Pb ratios. The determination of "domain specific" data and error follow the weighted average function in Isoplot/Ex (Ludwig 2000), using its criterion for elimination of statistical outliers. The uncertainties on individual spot analyses (point by point) range from ± 8 to ± 63 Ma with an average of ± 34 Ma (2σ), calculated from the chemical dating equation of Montel et al. (1996) from propagating 2σ level of confidence in elemental concentrations using Isoplot Excel add-in (Ludwig 2000).

CHAPTER 4: FIELD RELATIONSHIPS AND PETROGRAPHY

Field relationships within the amphibolite and diorite migmatite (Suite 1), K-feldspar gneiss (Suite 2) and stromatic Grt-Bt-Sil gneiss (Suite 3) and their associated neosomes from this study focus primarily on monazite enclosed in various domains, such as: inclusions in garnet, in the matrix (mostly biotite), and in the leucosome. The spatial relationship of monazite located within these domains is important because the microstructures have been used to establish a pattern of relative timing for mineral growth using U-Th-Pb EMPA chemical age dating for this region. Described below are the general field relationships and pertinent petrographic descriptive features and textures from the studied rocks with emphasis on the monazite-bearing samples.

Suite 1 - Amphibolite and Diorite Migmatite (Metatexite)

Suite 1 is a 150 m-wide by 20 m-high (at maximum height) road cut. The designation "diorite" migmatite from the 'amphibolite and diorite migmatite' is here used to refer to thin (3 – 30 cm-wide) intermediate to felsic grey to white diorite and granodiorite leucosomes (e.g. diorite) surrounded by amphibolite paleosome. Most commonly, the granodiorite leucosomes are oriented parallel to or at a small angle with the foliation of the host lithology (Figure 4). The fine- to medium-grained amphibolite paleosome is composed of large amphibole crystals, minor clinopyroxene, surrounded by plagioclase and quartz consistent with medium to coarse K-feldspar and quartz-rich grey monazite granodiorite leucosome, up to 20 cm-wide, that appear to 'flow' into the larger felsic granodiorite leucosome, illustrated in Figure 4.

Suite 1 exhibits crudely aligned hornblende and biotite with clusters of clinopyroxene (Figure 5c) in the amphibolites associated with a network of relatively later (cross-cutting) granodiorite leucosomes with large K-feldspar (Fig. 4). Locally, these amphibolites display relic clinopyroxene breaking down to amphibole and annealing fabrics suggestive of a prolonged

high-temperature environment following transitional granulite- to upper amphibolite-facies metamorphism (Fig. 5a-b). Representative petrographic mineral assemblages, including retrograde minerals, are listed in Table 1 and field sample descriptions are summarized in Table A1.

Plagioclase is weakly to moderately sericitized in all samples. Some also show curved albite law twins (Fig. 6a). Alteration of hornblende to sericite was observed throughout the amphibolite paleosomes (Fig. 5d). All minerals appear to be sharing grain boundaries with one another, with biotite or muscovite occurring along these grain boundaries. Anhedral hornblende prisms and cross-sections are strongly pleochroic (yellow to pale green to dark green), corroded by biotite and sericite and occasionally altered to chlorite. Quartz films occupy the interstitial space between plagioclase and K-feldspar in the granodiorite leucosome (Fig. 6c). Eye-shaped quartz porphyroblasts (augen; Fig. 6d) in the sheared diorite leucosome define the biotite foliation (e.g. Sawyer 2002).

The monazite granodiorite leucosome (Fig. 4) is medium- to coarse-grained. A small portion of coarse feldspar laths define a flow foliation and contact between the quartz-rich leucosome and matrix is sericitized hornblende (Fig. 5c-d). Quartz, in the leucosome, is interstitial to plagioclase in the form of large anhedral crystals and has curved, bulging grain-boundaries and also exhibits undulose extinction. Some plagioclase crystals show curved albite-law twins (Fig. 6a).

Large euhedral monazite crystals (up to 450 μm in diameter) preserve prismatic crystal shapes (Fig. 6b). Monazite displays high birefringence, high relief with few displaying minor yellow discolouration along the contours of the crystals in plane polarized light. Analyzed

monazite crystals occur at junction points between biotite, plagioclase, and K-feldspar also within highly sericitized plagioclase in contact with carbonates and chlorite.

At the outcrop scale, the boundary between the adjacent amphibolite and diorite migmatite is defined by sharp irregular contacts. The amphibolite paleosome is considered finer grained than the neosome and, in some places, the host rock occurs as fragments in the leucosomes (Fig. 4). The foliation in the country rocks invariably becomes concordant with the contacts of these felsic leucosomes and the border zones are either recrystallized or highly altered (Fig. 5c). Petrographic observations show that the leucosome occupies the dilatant structure itself, and has a partial envelope of highly altered and sericitized hornblende (Fig. 5c) along contact boundaries. Yet the amphibole from the amphibolites further away from these boundaries lack penetrative deformation.

Based on field and petrographic observations, the neosome from the amphibolite (paleosome) and diorite migmatite represent both in situ (diorite and granodiorite) and injected (monazite granodiorite) leucosomes. The sharp contact between the weakly deformed coarser-grained granodiorite (RAC22) and the fine- to medium-grained amphibolite is well preserved alluding to a cross-cutting relationship between the relatively younger granodiorite leucosome (diatexite) and older amphibolite host rock (Fig. 5c). The absence of a cross-cutting relationship between the amphibolite and the diorite migmatite leucosomes, which are sheared, could possibly indicate an in situ provenance for this metatexite migmatite.

Suite 2 - K-feldspar Gneiss (Diatexite)

This suite is a 10 m-wide outcrop consisting of a fine- to medium-grained migmatite with gneissic banding (Fig. 7) defined by alternating layers of fine-grained K-feldspar- and quartz-rich segregations (leucosome) with medium-grained mafic layers of plagioclase + biotite ± dark

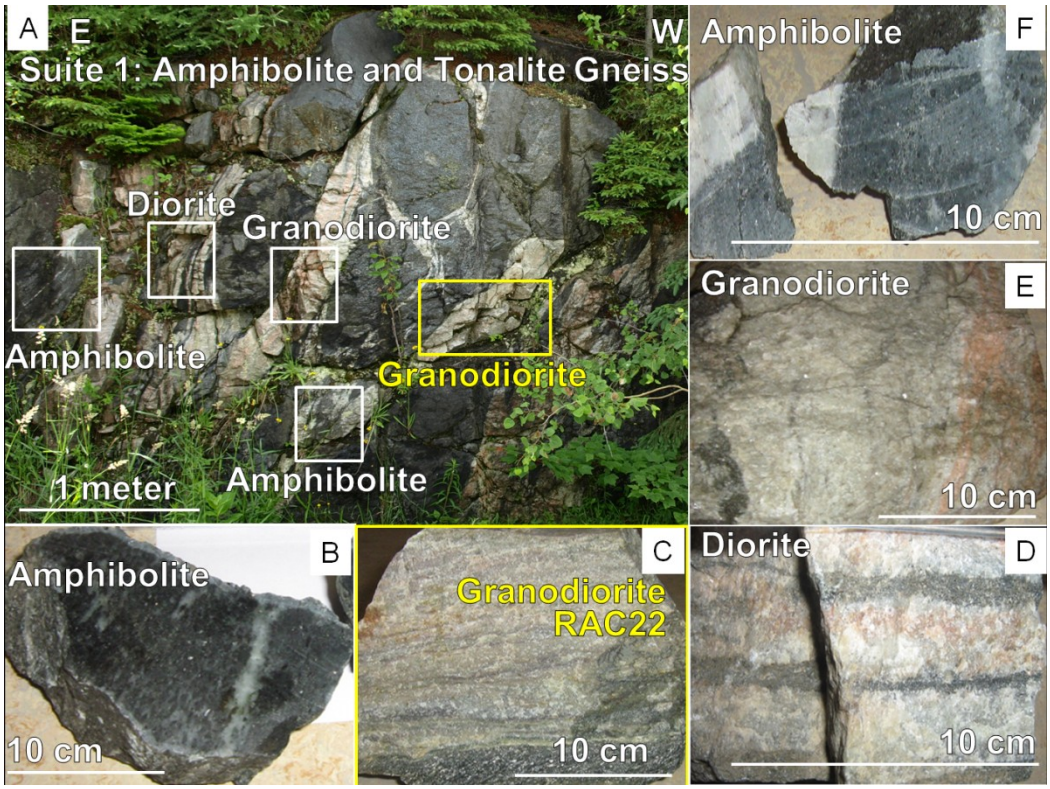

Figure 4: Field images from the studied Otter Lake area show representative sample locations within amphibolite and diorite migmatite (Suite 1; A). The fine- to medium-grained amphibolite paleosome (B, F) is comprised of large amphibole crystals surrounded by plagioclase and quartz which define the foliation, consistent with medium to coarse K-feldspar and quartz-rich segregation (leucosome) foliation, such as diorite (D). Mafic selvages are present at some of the paleosome - leucosome contacts. Small granodiorite leucosomes (RAC22; C) up to 20 cm wide appear to 'flow' (injected) into the larger granodiorite (E) leucosome. Samples highlighted in yellow are monazite-bearing whereas white sample labels indicate monazite-absent samples. Mineral abbreviations are after Whitney and Evans (2010).

Table 1: Petrographic mineral (estimated modal %) values from each thin section from the three studied suites are summarized below. The studied monazite-bearing sample mineral estimates are represented in bold. S1-S3: Suite 1-3; t- trace; Aln- allanite; Ap- apatite; Bt- biotite; Cc- calcite; Chl- chlorite; Cpx- clinopyroxene; Grt- garnet; Hbl- hornblende; Kfs- K-feldspar; Mnz- monazite; Ms- muscovite; Ox- oxides; Qtz- quartz; Ser- sericite; Sil- sillimanite; Ttn- titanite. Mineral abbreviations are after Whitney and Evans (2010).

	Section #	**Qtz**	**Pl**	**Kfs**	**Bt**	**Hbl**	**Cpx**	**Grt**	**Ser**	**Ms**	**Sil**	**Aln**	**Ttn**	**Chl**	**Ap**	**Cc**	**Zrn**	**Mnz**	**Ox**
S1	RAC 23 Granodiorite	30	30	20	15				4	<1								t	
S1	RAC 22 Granodiorite	40	30	20	5				5	<1				<1				t	
S1	RAC 21 Granodiorite	30	30	10	3		10		15	2									
S1	RAC 20 Granodiorite	30	30	10	5		10		10	5									
S1	08-07-09-2 Amphibolite	10	15	10	5	45	5		4					4			<1		<1
S1	08-07-09-3 Granodiorite	30	50	5					10	5									
S1	08-07-09-4 Amphibolite	15	20	10	5	40	5		<1	<1				<1			<1		<1
S1	RAC 9 Diorite	30	20	8	20		5		10	<1				5			<1		
S1	RAC 6 Diorite	35	20	10	10	10			4	5				4			<2		
S2	RAC 2 Qtz-Monzonite	20	30	10	20	2	<1		7	2		<1	5	<1			t		<1
S2	RAC 1 Monzodiorite	30	20	25	5	5			1	<1		1	2	<1	2	<1	<1		5
S3	12695 Qtz-Monzonite	30	25	15	20				<3	<1					4		<1	<1	
S3	RAC 18 Monzonite	40	30	15	5				9	1									
S3	RAC 10 Granite	30	5	25	5			10	<1	<5	15			<1	1		<1	<1	
S3	RAC 13 Monzonite	25	10	15	30			10	<1	<1	5				1		<1	<1	
S3	RAC 3 Qtz-Monzonite	35	30	5	10			5	7	3	2				1		<1	<1	
S3	RAC 8 Qtz-Monzonite	20	17	5	30			20	<3	<1	1				1		<1	<1	

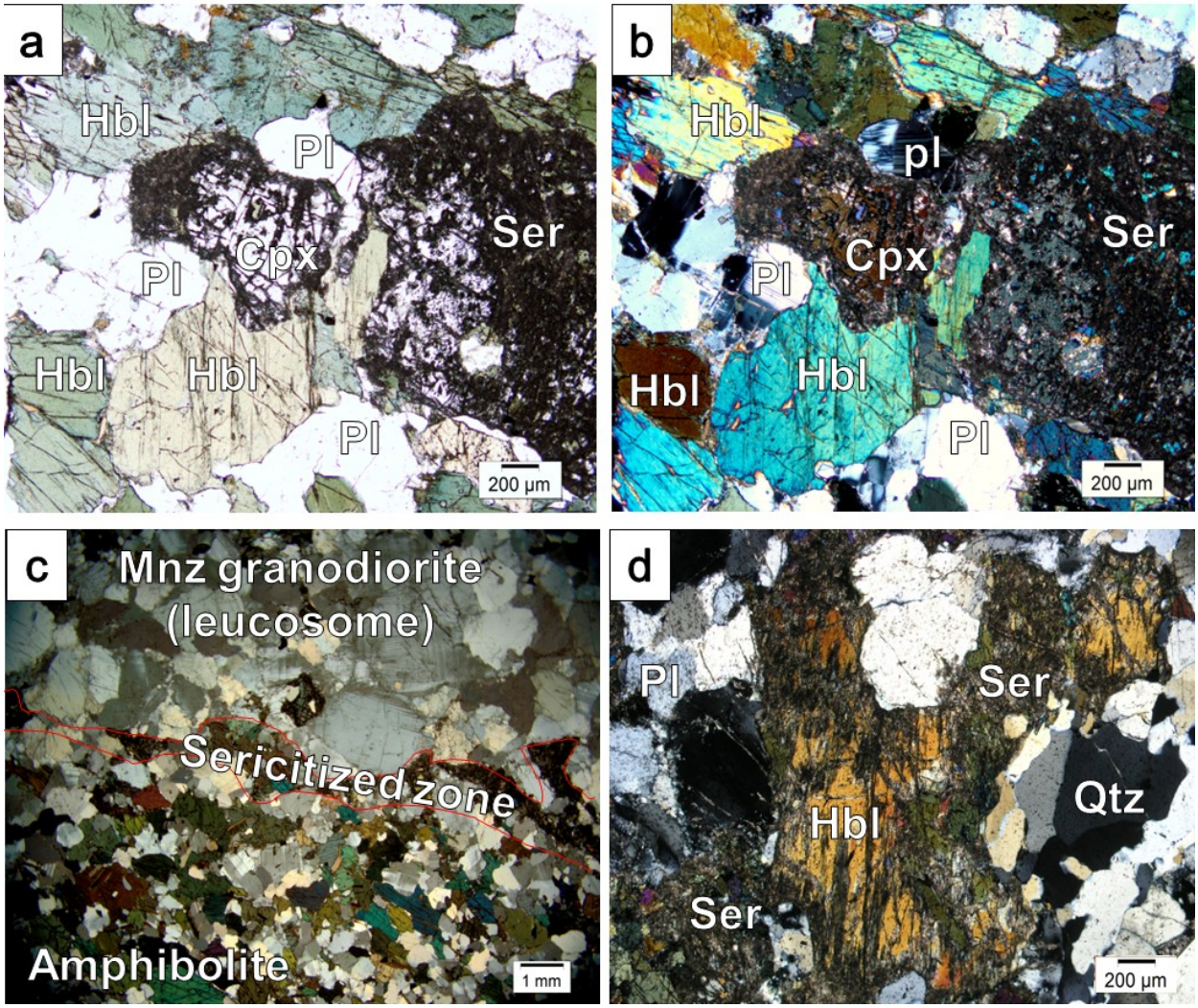

Figure 5: Photomicrograph thin section textures from the amphibolite and diorite migmatite (Suite 1), representing key contact and alteration features (**a**) plane-polarized photomicrograph and (**b**) cross-polarized photomicrograph images within the diorite migmatite which displays amphibolite foliation defined by biotite and amphibole. The amphibolites (± clinopyroxene) show locally developed amphibole and sericite rims on relict clinopyroxene. (**c**) Cross-polarized photomicrograph of a small portion of coarse feldspar laths which define a flow foliation and contact between the quartz-rich leucosome separated from the matrix by the sericitized hornblende zone. (**d**) Anhedral quartz crystals occupy the interstitial space between plagioclase and hornblende with secondary sericite replacing hornblende. Mineral abbreviations are after Whitney and Evans (2010).

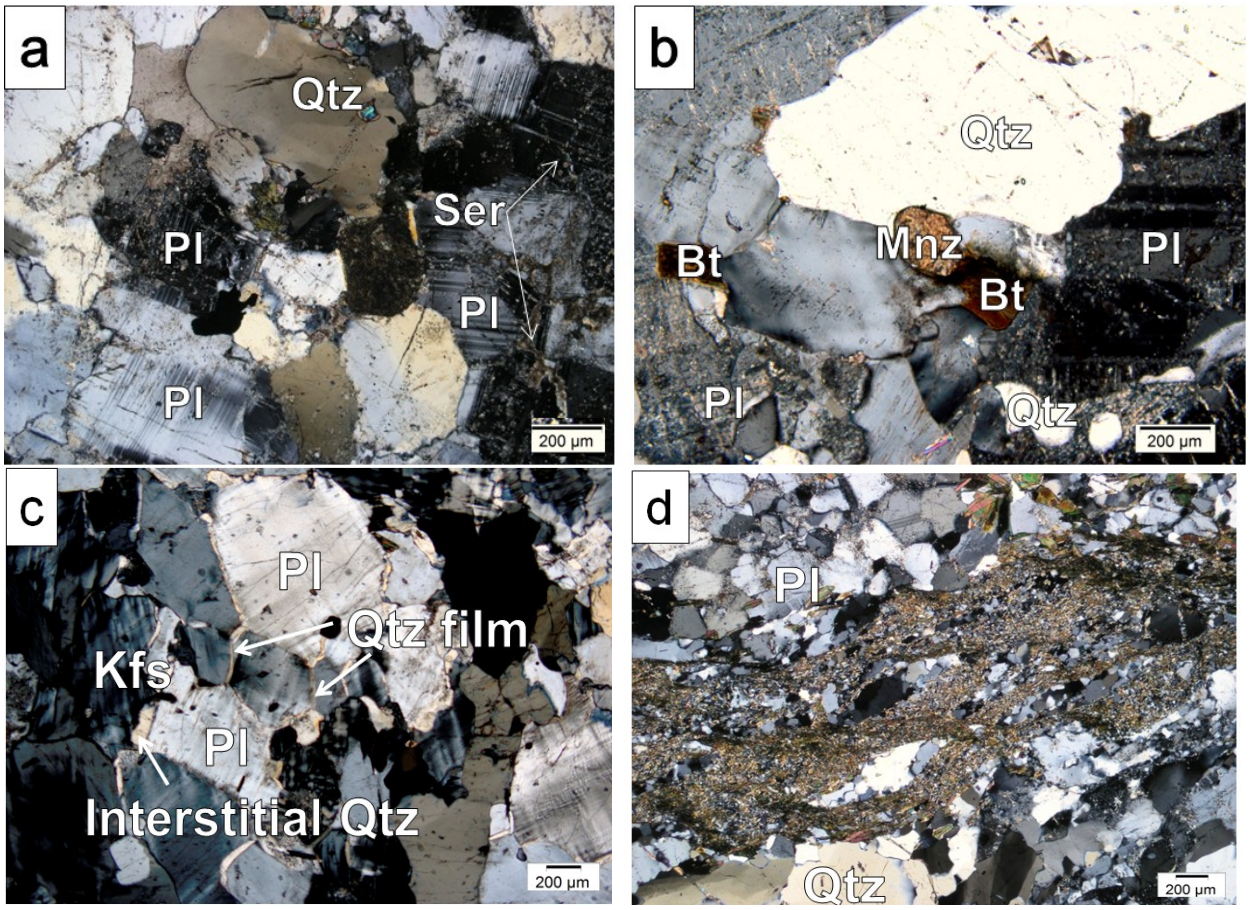

Figure 6: Cross-polarized photomicrograph thin section images showing representative leucosome textures from the monazite-bearing granodiorite (RAC22) from Suite 1. (**a**) Quartz + Plagioclase ± K-feldspar ± Biotite define the leucosome mineral assemblage. Quartz is interstitial to plagioclase in the form of big anhedral crystals and exhibits undulose extinction in response to some form of deformation. Some plagioclase crystals show curved albite-law twins and sericitization. (**b**) Large euhedral monazite crystals in the injected granodiorite (RAC22) preserve prismatic crystal shapes. Monazites from this sample occur along grain boundaries and at triple junction points between quartz, plagioclase, K-feldspar, and biotite. **(c)** Anatectic melt first form a thin film along grain boundaries and edges- evidence for partial melting (granodiorite, RAC22; xpl) (d) Augen gneiss with eye-shaped porphyroclasts (augen) of quartz in a sheared quartz + plagioclase ± biotite felsic leucosome (diorite, RAC6/9; xpl) Mineral abbreviations are after Whitney and Evans (2010).

hornblende (melanosome) (Table 1). These felsic leucosomes range in diameter from 0.5 mm to 10 mm parallel to the mafic foliation-defining layers. The layered banding within the gneiss is disturbed by the later coarse-grained quartz + K-feldspar pegmatitic syenite with metamict haloes around allanite, too coarse for thin section analysis yet was analyzed for whole-rock geochemistry. The melanosome is a homogeneous, melanocratic rock in which the pink perthite laths are partially recrystallized to microcline and albite (Fig. 8a) near the leucosome contact.

In the neosomes, subhedral to anhedral allanite is found in contact with dendritic magnetite and locally associated with perthite (Fig. 8b). These titanite crystals are anhedral, embayed, mainly occur within the kinked biotite melanosome defining the rocks' foliation or rarely occur as inclusions in rounded quartz and plagioclase crystals (Fig. 8c-d). Zircon was found as inclusions in biotite and allanite as well as within leucosomal highly sericitized plagioclase crystals. It should be noted that where allanite and titanite are present (Suite 2) no monazite or garnet were observed.

The highly sericitized plagioclase, altered titanite rims, and perthitic textures likely indicate significant hydrothermal alteration of these samples (Kretz 2009). The presence of a later very coarse-grained pegmatitic syenite (diatexite) causes the foliation of the overlying melanosome to plastically deform and therefore may be further explanation for the alteration (metasomatic) features observed in this sample.

The metasomatized K-feldspar gneiss is a highly sericitized and altered assemblage of intercalated leucosome and melanosomes bands where allanite and titanite (± zircon) are the main accessory minerals. Due to the absence of monazite from this suite, the focus of geochemical and geochronology studies will be placed on Suites 1 and 3.

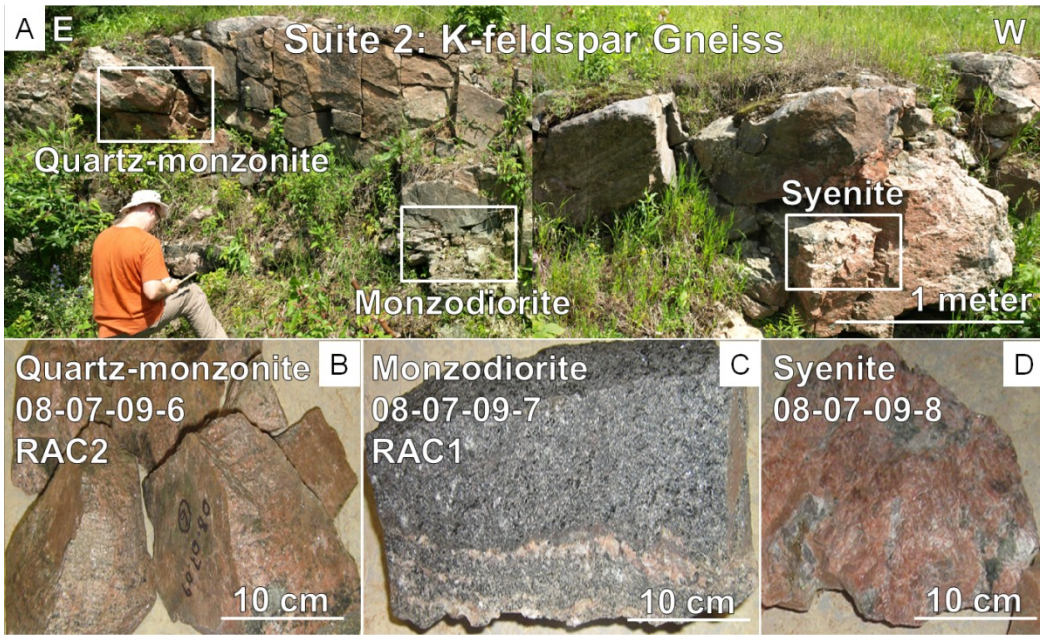

Figure 7: Field images from the studied 10 m-wide outcrop depicting a fine- to medium-grained K-feldspar gneiss (Suite 2; A-D) with gneissic banding defined by alternating bands of fine-grained K-feldspar- and quartz-rich segregations (quartz-monzonite; B) interlayered with medium grained mafic layers of plagioclase + biotite ± dark hornblende (monzodiorite; C). The layered banding within the gneiss is plastically-deformed by the later coarse-grained quartz + K-feldspar pegmatitic syenite (D) with radiation haloes, visible to the naked eye, around allanite. Mineral abbreviations are after Whitney and Evans (2010).

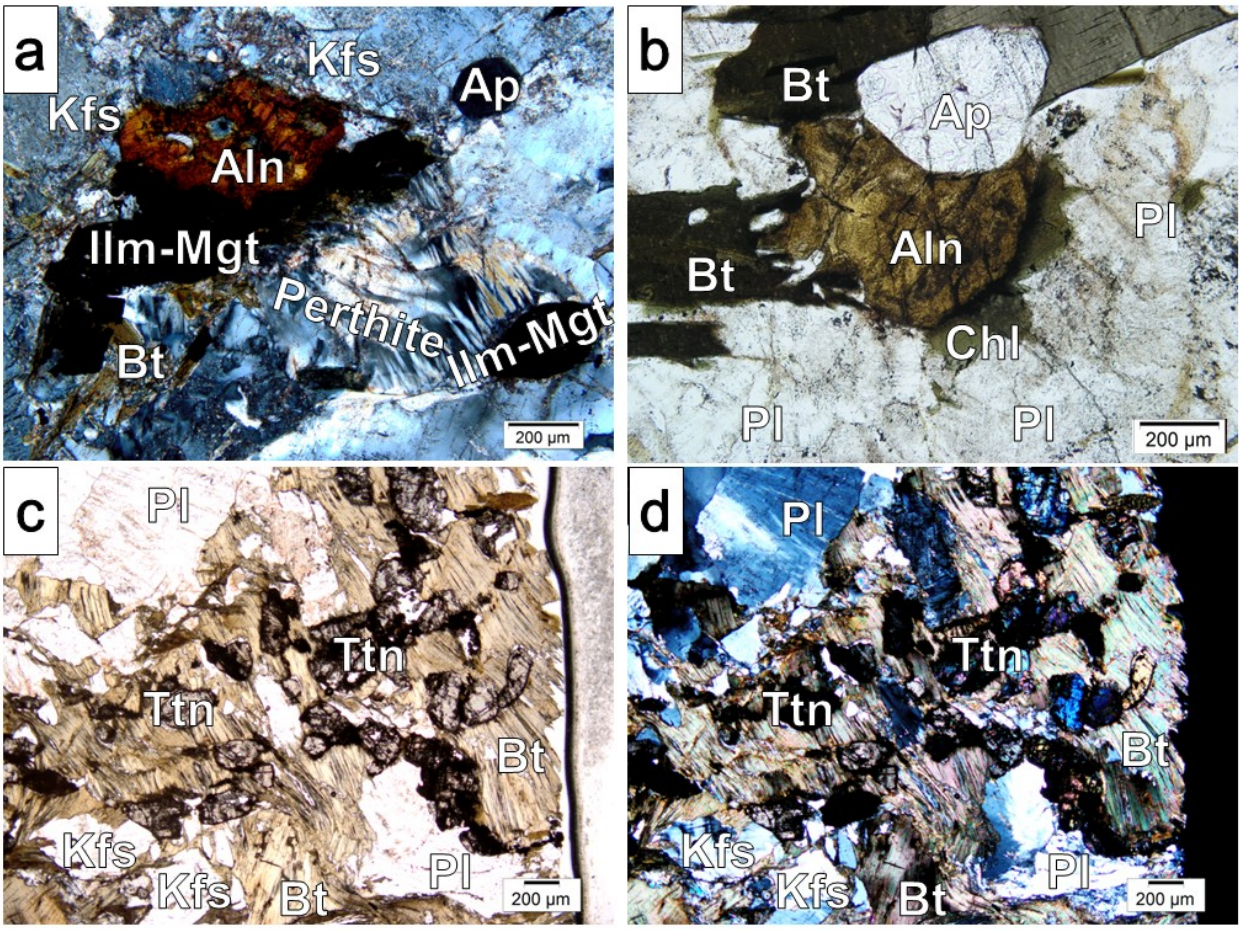

Figure 8: Petrographic thin section images taken from the K-feldspar gneiss, Suite 2, illustrating distinct textural features in which the pink perthite laths (**a**) are partially recrystallized to microcline and albite within the monzodiorite melanosome. RAC1 is a homogeneous, melanocratic rock near the contact with quartz-monzonite leucosome. (**b**) Allanite is subhedral to anhedral with few euhedral crystals in the quartz-monzonite associated with and/or always in contact with biotite crystals. Allanite is also found to be in contact with dendritic ilmenite-magnetite, locally associated with perthite (as seen in Fig. 8a). Altered titanite, seen in both plane polarizing light (**c**) and crossed-polarizing light (**d**), have dark black alteration rims surrounding crystal cores. These titanite crystals are anhedral, embayed, and mainly occur within the kinked biotite melanosome defining the rock's foliation or rarely occur as inclusions in rounded quartz and plagioclase crystals. Mineral abbreviations are after Whitney and Evans (2010).

Suite 3: Stromatic Grt-Bt-Sil Gneiss (Metaigneous & Metasedimentary; Metatexite & Diatexite)

The exposed stromatic migmatite from this 30 m-wide outcrop is defined by mineralogically distinct millimeter- to decimeter- spaced discontinuous bands formed by alternating melanocratic monzonite and leucocratic granite bodies (Fig. 9). Segregation of melanosomes define the biotite (sillimanite ± muscovite) foliation (Fig. 10a,c). The garnet-bearing stromatic bands are concordant (Fig. 9) with varying widths and compositions as reflected by the consistent steeply-dipping orientated layers which might represent relic pelitic or greywacke sedimentary bedding (e.g. Kretz 2007).

The cross-cutting neosomes to the main foliation in the host rock include the fine-grained, discontinuous quartz-monzonite leucosome (12695) interlayered with parallel melanosome monzonite (12696) layers (Fig. 9). These two samples, although located between Suite 1 and Suite 3, were placed as part of Suite 3 based on their proximity (< 1 km) and geochemical similarities (Ch. 5). Based on cross-cutting field relationships and petrographic similarities to the injected granodiorite (RAC22) from Suite 1 these two samples are interpreted to be injected neosomes.

The contacts between the granitic leucosome and the adjacent melanosome (garnet quartz-monzonite and garnet monzonite) are sharp in both outcrop and hand samples but are irregular on the grain scale (Figure 10a). The melanosomes from the stromatic migmatite are garnet, biotite and sillimanite-rich (Fig. 10a). The grain size of the minerals (mainly garnet and biotite) in the melanosome decreases systematically away from the leucosome. Most of the garnet occurs close to the contact with the leucosome. Garnet, observed in melanosome (quartz-)

monzonite samples (RAC 3, 8 and 13), occur mainly near the leucosome boundaries and have inclusions of quartz, biotite, apatite, rutile, monazite and zircon.

Two petrographically distinct garnet (Fig. 10a) varieties are observed in thin section: large (RAC8) and small garnets (RAC3, 8 and 13). The small, euhedral garnets are typically smaller than ~ 1-2 mm whereas the garnet porphyroblasts (RAC8) are up to ~ 9 mm in size and have inclusions of elongated quartz and biotite orientated at a high angle to the external matrix foliation defined by biotite and sillimanite (Fig. 10a). The biotite and sillimanite-defining foliation, contouring and in contact with garnet porphyroblasts, suggest that biotite and sillimanite possibly formed in situ at the expense of garnet. Retrograde reaction during cooling causes resorption of garnet and liquid by the reverse of reaction 1. Reaction microstructures support replacement is only possible if melt is available as a reactant, implying its retention within the system. As a whole, these textural features suggest retrograde reactions where biotite and sillimanite are produced from peritectic garnet:

$$Bt + Sil + Pl + Qtz \leftrightarrow Grt + Kfs + Liq \qquad (1)$$

Monazite was identified in three neosomes within the grt-bt-sil gneiss (1) in situ garnet monzonite (RAC13), (2) in garnet quartz-monzonite (RAC3) and (3)in the injected quartz-monzonite. Monazites from the in situ samples occur in three texturally distinct domains: leucosome, matrix and as inclusions within garnet whereas monazites from the injected quartz-monzonite occur only in the leucosome and matrix domains described in Ch. 7.

Based on field and petrographic observations, two types of neosomes are represented in the stromatic Grt-Bt-Sil gneiss (metatexite) (1) the in situ granite neosomes and (2) injected neosomes. Monazite occurs within both the in situ and injected neosomes yet two types of garnet are only present in the in situ melanosomes. These field and petrographic relationships

may be useful for geochemical and geochronological interpretations for the tectonic evolution within the Otter Lake area, CMB-Q.

Summary field relationships and petrography for monazite-bearing samples

The monazite-bearing injected leucosome samples occur in two manners as observed at the outcrop/field scale: (i) as sub-parallel granodiorite leucosomes with the foliation of the host lithology (amphibolite) from the amphibolite and associated diorite migmatite and (ii) quartz-monzonite leucosomes which cross-cut the stromatic Grt-Bt-Sil gneiss samples. The injected leucosomes bear very similar petrographic and field relationship similarities to one another even though they occur in different Suites. This could possibly indicate they these two samples are from the same or similar sources. The K-feldspar gneiss represents a diatexite migmatite, but due to the absence of monazite and garnet from the allanite- and titanite-bearing gneiss emphasis is placed on the study of the four monazite-bearing neosomes found within the amphibolite and associated diorite migmatite and Grt-Bt-Sil gneiss.

These four samples include the injected granodiorite and quartz-monzonite from Suites 1 and 3, respectively, as well as the in situ garnet quartz-monzonite and garnet monzonite from Suite 3. Based on field and petrographic observations at the thin section scale the monazites in the injected neosomes (diatexites) are divided into two petrographically distinct domains: leucosome (L) and matrix (M). The monazites in the in situ neosomes (metatexite) from Suite 3 occur in three texturally distinct domains: leucosome (L), matrix (M) and as inclusions within garnet (G). Geochemical and geochronological data will help constrain these field and petrographic observations relative to host rock protoliths and associated Grenvillian tectonism preserved within the studied Otter Lake area, CMB-Q.

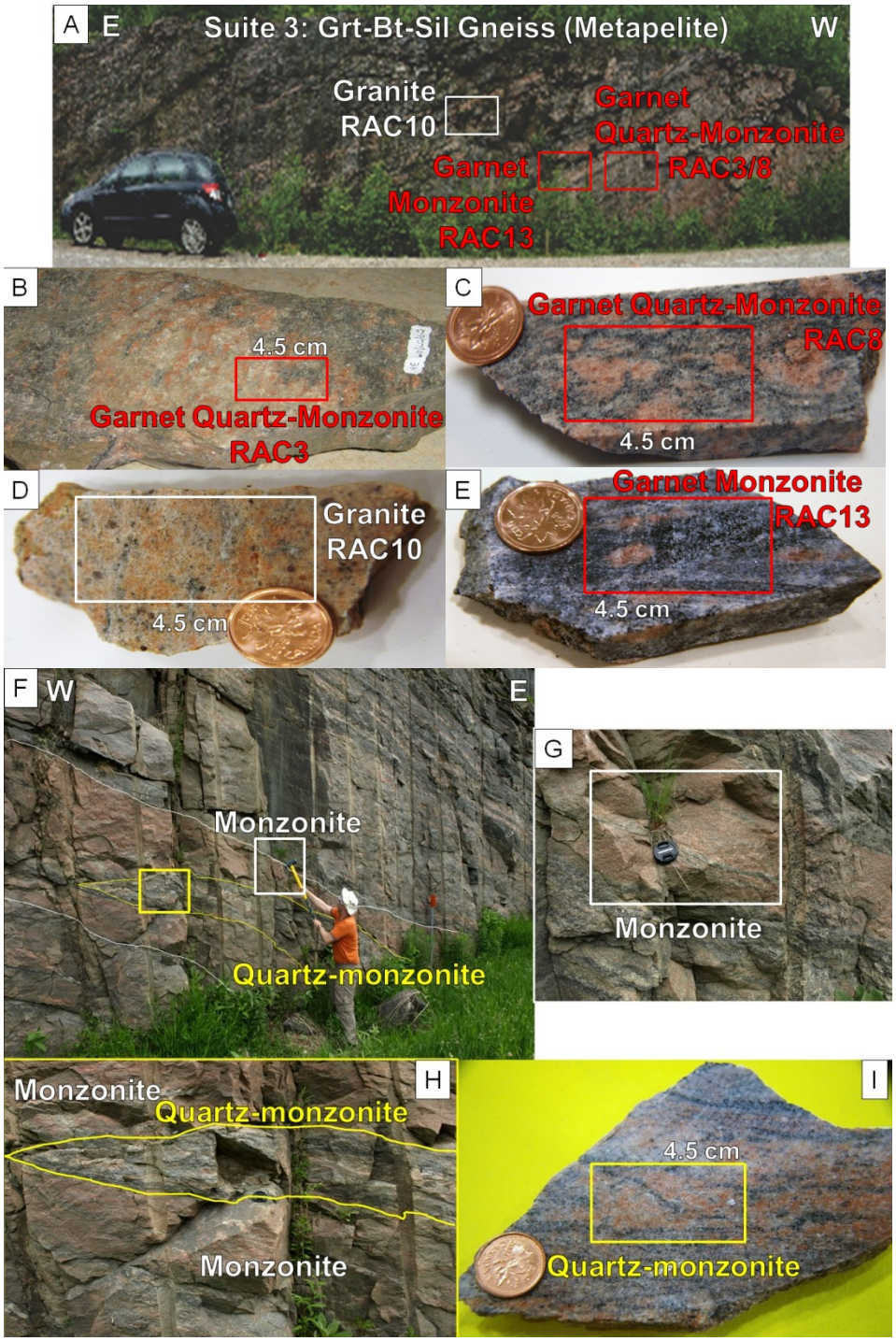

Figure 9: Road cut field images of representative sample locations along Hwy 301 between Danford and Otter Lake from the stromatic Grt-Bt-Sil gneiss (Suite 3; A-E) near contact between amphibolite and reaction zone (F-I). Images for the transition between base of migmatite (RAC3/8; B, C) and Kfs gneiss fine grain granite vein (12695; H-I) and the coarser migmatite (12696, G) as part of melanosome are depicted above. Samples 12695 and 12696 are located just east of Suite 3 (F), between Suite 1 and 3. They are thus grouped into Suite 3 due to their proximity (< 1 km). Samples highlighted in red (mnz- and grt-bearing), yellow (mnz-bearing), and white (mnz-absent). Mineral abbreviations are after Whitney and Evans (2010).

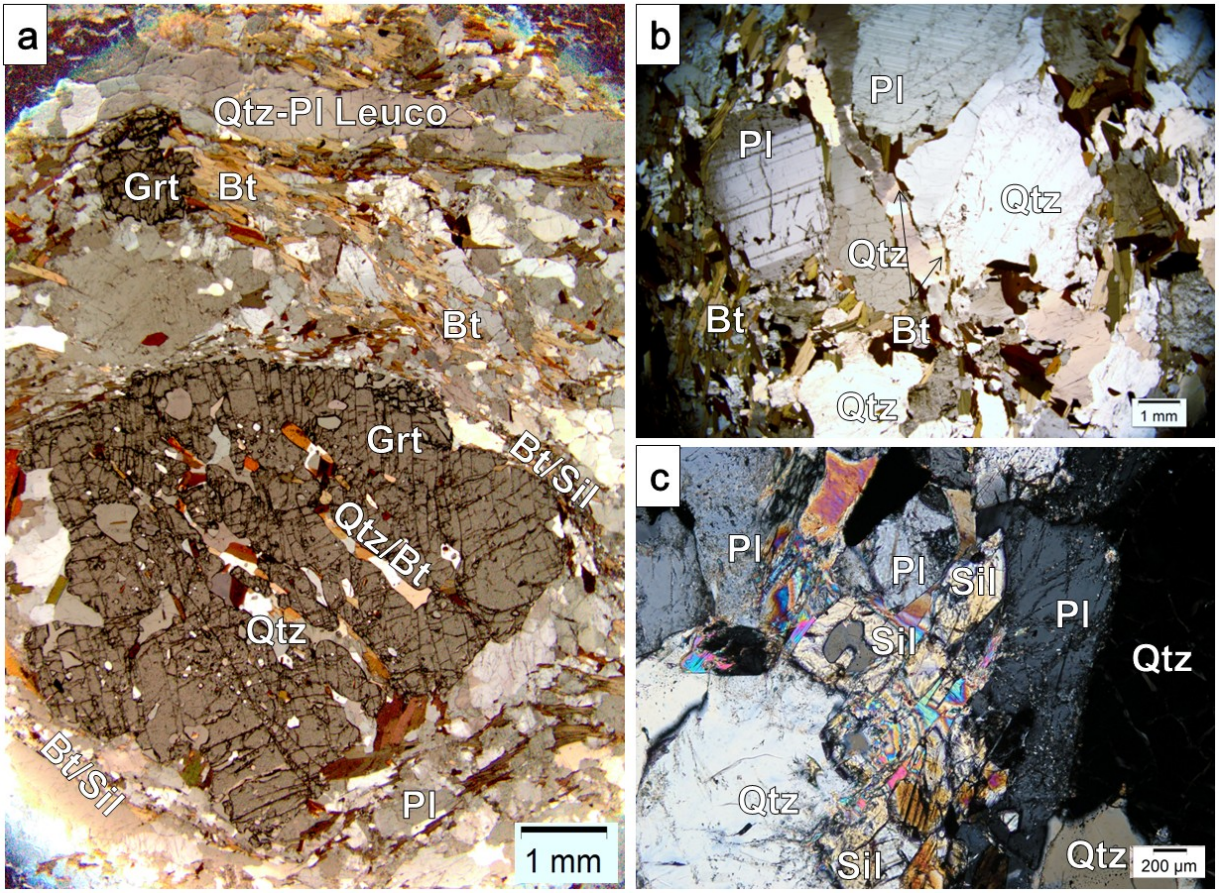

Figure 10: Petrographic thin section images from the stromatic Grt-Bt-Sil gneiss (Suite 3). (**a**) Quartz – plagioclase leucosomes contour and cross-cut the melanosome portion of the garnet quartz-monzonite. The melanosomes from this Suite consist of the assemblage biotite + garnet + sillimanite + K-feldspar + quartz + plagioclase and exhibits an internal mineralogical and textural zonation. The garnet has inclusions of elongated biotite and quartz that define an internal fabric orientated at a high angle to the external foliation defined by biotite and sillimanite. Most of the garnet occurs close to the contact with the leucosome. The biotite nearest to the leucosome (**a**, **b**) is considerably coarser-grained than biotite farther away and may, in part, replace the garnet. The leucosome (**b**) is granitic in composition, and has the mineral assemblage quartz + plagioclase + K-feldspar + minor biotite. Preferentially aligned quartz and plagioclase phenocrysts (**b**) in the quartz-monzonite occur with interstitial biotite along crystal boundaries. (**c**) Sillimanite occurs as skeletal crystals, elongated crystals (parallel to foliation) and as prisms within the grt quartz-monzonite. Mineral abbreviations are after Whitney and Evans (2010).

CHAPTER 5: WHOLE-ROCK ANALYSIS

The question to be addressed in this chapter is whether host rocks (paleosomes) affected by Grenville metamorphism (in situ partial melting) represent the source(s) for the monazite-bearing neosomes or whether these are associated with the injected Chevreuil and Kensington-Skootamatta plutonic suites (Corriveau et al. 1990, 1996, 1998; Corriveau and Gorton 1993; Corriveau and Morin 2000; Morin et al. 2005). Thirteen rock samples within the Otter Lake area were selected for major, trace and rare earth element analysis (Table 2) in order to address this question. Five samples from amphibolite and diorite migmatite, three samples from K-feldspar gneiss and five samples from Grt-Bt-Sil gneiss were analyzed. The samples are furthermore separated into paleosome and neosome (including leucosome and melanosome).

Major Element Geochemistry

The studied samples show variable silica content ranging from 47.90 – 72.40 wt% SiO_2 (Table 2). Amphibolite paleosome samples from the amphibolite and associated diorite migmatite outcrop have SiO_2 contents of 47.90 – 49.40 wt%, respectively. All neosome samples, including K-feldspar gneiss samples, show variable silica and alkali contents and can be chemically classified using the $Na_2O + K_2O$ vs. SiO_2 from Middlemost (1994), also referred to as the total-alkali vs. silica (TAS) diagram (Figure 11). All neosomes show a wide compositional range with samples plotting on either side of the alkaline-subalkaline trend line, reflecting different leucosome sources (Fig. 11). The medium- to high-K calc-alkaline leucosomes from the diorite migmatite show evidence for melt evolution from diorite through to granodiorite.

Here the terms in situ and injected leucosome and melanosome are based on field and petrographic observations. Both in situ and injected samples from the stromatic Grt-Bt-Sil gneiss cluster along the monzonite, quartz-monzonite and granite fields on the TAS

discrimination diagram (Fig. 11). The samples from the K-feldspar gneiss plot marginally in the alkaline field with the more mafic sample melanosome represented by monzodiorite and the more felsic quartz-monzonite leucosome and alkaline syenitic pegmatite, respectively. Corriveau et al. (1998) also observed potassic alkaline plutons in the CMB-Q consistent with field observations of the later syenitic pegmatite deforming the K-feldspar gneiss samples from this study. K-feldspar gneiss samples do not contain any monazite therefore geochemical emphasis is placed on monazite-bearing samples.

Both the in situ and injected leucosomes have similar major element geochemical trends: enrichment in K_2O, Al_2O_3 and Na_2O concentrations with increasing SiO_2 relative to decreasing CaO, P_2O_5, Fe_2O_3 and MgO in the paleosome (Table 2). The amphibolite paleosomes have lower SiO_2 and Al_2O_3 and higher CaO, MgO and Fe_2O_3 contents relative to neosomes. Field and petrographic observations for the alteration of pyroxene and amphibole to K-feldspar (and sericite) and the associated enrichment of SiO_2, K_2O and Na_2O in the leucosomes is possible evidence for the introduction of siliceous K-rich (alkaline) metasomatic fluids into these host rocks as demonstrated by Corriveau et al. (1990).

Further characterization of the neosomes in the K_2O vs. SiO_2 diagram (Fig. 12) show the amphibolite with diorite migmatite plot in the medium- to high-K calc-alkaline field whereas the stromatic Grt-Bt-Sil gneiss neosomes plot in the shoshonitic field. The shoshonitic character of the in situ Grt-Bt-Sil gneiss neosomes is also concordant with the measured high Al_2O_3 content (Table 2) and supported by noticeable abundance of K-feldspar, garnet and aluminosilicates (i.e. sillimanite).

Both the injected leucosomes and in situ melanosomes from this study have indicated an Al-saturated nature and display dominant peraluminous behaviour in all samples with values

greater than 1.1. This is confirmed in the alumina Saturation Index (ASI) where clustering is clearly within the peraluminous field (Fig. 13). The ASI is also widely used to geochemically discriminate between sedimentary (S-type) and igneous (I-type) granitoids indicating probable magma sources (e.g. Chappel and White 1974). Accordingly, the studied neosome samples from the Otter Lake area plot within the S-type granitoid field (Fig. 13) potentially derived from partial melting of crustal rocks.

Trace Element Geochemistry

Trace element abundances are good geochemical tools with which to explore the fractionation and partial melting natures of magma sources (e.g. Arculus and Johnson 1981). Trace element concentrations of the Otter Lake area are listed in Table 2.

The amphibolite paleosomes from Suite 1 have higher Cr, Ni and V concentrations compared to all other samples from this study. Both in situ and injected leucosomes from Suite 1 show high contents of Ba and Zr relative to amphibolite paleosomes. These leucosomes also have decreasing Ni, Cr and Y whereas Rb, Sr, Nb and Th remain unchanged with increasing SiO_2 wt% concentrations (Table 2). The leucosomes from the stromatic Grt-Bt-Sil gneiss relative to the melanosome samples reflect increases in Ba, decreases in Ni, Nb, Y, Zr and Th while Cr, Rb and Sr remain relatively unchanged with increasing SiO_2 wt% concentrations. Due to the various degrees of metamorphism and magmatism previously recorded in the study area, it is assumed that the analyzed samples have undergone metasomatic changes in the mobile elements such as alkalies (K_2O and Na_2O), CaO, and the large ion lithophile elements (LILE: e.g. Rb, Sr, Ba, Th) have possibly been mobilized and thus may not represent original pre-metamorphic concentrations.

On the primitive mantle-normalized diagrams (Fig. 14) which are used as indicators of fractionation (e.g. Corriveau et al. 1999; Corriveau and van Breeman 2000) the fluid-mobile LILE in the leucosomes are enriched in Rb, Ba, K, and Pb and depleted Nb, Ti, Y, and REEs relative to melanosome concentrations and are in accordance with the fractionated high-K calc-alkaline to shoshonitic Kensington-Skootamatta plutons studied by Corriveau et al. (1998) in the CMB-Q area. The enrichment of Th, U, K, Ce, Pb and Zr and depletion in Nb, Sr and Ti (Fig. 14) indicates the involvement of refractory mineral phases, such as apatite (observed in abundance in all samples), monazite and zircon during granitoid formation consistent with field, petrography and major element whole-rock geochemistry.

The provenance of monazite-bearing leucosomes can also be inferred from the abundance and ratio of certain trace elements with fairly low mobility as a function of tectonic setting. The in situ shoshonitic neosomes from the Grt-Bt-Sil gneiss are more alkali-rich ($Na_2O + K_2O$) relative to injected calc-alkaline neosomes from amphibolite and associated diorite migmatite (Figs. 11, 12 and 13). The in situ neosomes show nearly identical trace primitive mantle-normalized and LREE-enriched relative to HREE-depleted chondrite-normalized patterns with negligible Th, Sm and Eu anomaly differences. The studied in situ neosomes from Suite 1 and 3 show $(Ce/Yb)_N$ values range from 3.74 – 6.54. The injected monazite-bearing granodiorite and shoshonitic quartz-monzonite show sub-parallel and strongly fractionated REE patterns $(La/Yb)_N$ 28.21 and 49.73, respectively, and $(Ce/Yb)_N$ values range between 19.66 – 33.12 (Table 3). The injected neosomes also show LREE enriched relative to HREE depleted chondrite-normalized patterns and slightly concave-up middle REE to heavy REE patterns with no Eu anomalies. This suggests more than one magma source for the injected neosomes from Suite 1 and 3 (RAC22, 12695 and 12696).

Similarly, these multi-elemental plots (Pearce et al. 1984) point towards a mixed source as evidenced by distinct enrichment of Rb and depletion of Y (Fig. 14) characteristic feature of collisional granites but they differ on the account of Th and La. Enrichment of Rb and Th relative to Nb, and higher abundances of La (injected neosomes) can be attributed to crustal involvement (Harris et al. 1983) leading to terigenous sediment input (and/or garnet in the restite; Fig. 18a) as well as granitoid formation in a continental margin arc environment (Fig. 18b). Hence, it appears that crustal contamination has caused variations in trace element representation and show gradation between mantle-dominated injected and in situ melanosomes (Fig. 16b) and high-Al slab-derived crust-dominated patterns (Fig. 16b).

Samples with high Sr/Y ratios (112.05 – 266.63 ppm; Fig. 16b) include: diorite migmatite leucosomes and injected granodiorite leucosome from amphibolite and diorite migmatite and injected quartz-monzonite leucosome from Grt-Bt-Sil gneiss suggesting high-Al slab-derived granitoids. Whereas amphibole (Suite 1) and melanosome (Suite 3) samples all have Sr/Y ratios < 25 ppm implying mantle-derived arc magmas. These major and trace element geochemical trends support crustal and mantle-derived host rock protoliths.

Rare Earth Element (REE) Geochemistry

The principal carriers of REEs in most granitic neosomes are the accessory minerals such as monazite, zircon, apatite, xenotime and titanite in addition to plagioclase in the case of Eu therefore fractionation of accessory minerals would result in lowering the REE content (e.g. Bea et al. 1994; Bea 1996). The chondrite-normalized REE distribution patterns for all three suites (Fig. 15) with chondrite-normalized values according to Taylor & McLennan (1985) show that the amphibolite paleosomes have essentially flat chondrite-normalized REE patterns with decreases in ΣREE for more felsic leucosomes representing the diorite migmatites (Table 3).

Suite 1 best illustrates the effects of in situ and/or injected partial melting and/or fractionation caused by anatexis where these effects have been studied by plotting injected and in situ neosomes with protolith- (paleosome)-normalized geochemical data (Fig. 17; e.g. Nehring et al. 2009). The amphibolite mesosome, representing the paleosome, with no Eu anomaly and a flat REE (Figs. 15 and 17) pattern may be regarded as the closest approximation to the original melt composition (e.g. Sawyer 2008). Paleosome-normalized values < 1 for the in situ (diorite and granodiorite) and injected granodiorite leucosomes are indicative of partial melting whereas values > 1 for the melanosome amphibolite indicate the presence of trapped melt (fractionation) (e.g. Bhadra et al. 2007).

The protolith amphibolites are characterized by no to slightly negative Eu anomalies whereas the melanosomes from the stromatic Grt-Bt-Sil gneiss are characterized by a slight negative Eu anomalies and slight enrichment of the LREE over HREE (Fig. 15; Table 3). In situ and injected leucosomes, from both suites, show a wide range of positive Eu anomalies ranging from 1.43 – 5.31.

The overall positive Eu anomalies in leucosomes (Fig. 17) may indicate that plagioclase fractionation was important in their petrogenesis because of the high partition coefficients of plagioclase for Eu (Bea et al. 1994). The large protolith-normalized positive Eu anomalies (Fig. 17) as observed in the in situ leucosomes may contain plagioclase and quartz crystallized from percolating and possibly extracted melt phases (Brown 2001, Nehring et al. 2009; Fig. 17). On the other hand, the injected leucosome lacking both chondrite-normalized (Fig. 15) and protolith-normalized Eu anomalies (Fig. 17) must therefore contain higher proportions of entrained plagioclase, magma mixing or melt fractionation (e.g. Stagslad et al. 2005).

Furthermore, both the injected and in situ leucosomes from diorite migmatites suggest fractionation with the enrichment of LREE over HREE (Table 3; Figs. 15 and 17), concave-up HREE patterns and varying Eu anomalies (e.g. Bhadra et al. 2007). The variations in the abundance of garnet in the source or as a fractionating phase are the most likely cause for the steep HREE-depleted chondrite-normalized REE patterns (Pyle et al. 2001). The low HREE and Y contents observed in the in situ and injected leucosomes from Suites 1 and 3 (Figs. 15 and 17) suggest that garnet growth was coeval during leucosome formation (Kohn et al. 2005).

Summary of the geochemistry of monazite-bearing neosomes

The provenance of these rocks is important when attempting to determine whether the associated neosomes (leucosomes) formed from in situ or injected melts derived from either magmatic or metamorphic sources. Whole-rock analysis from the Otter Lake area samples reveals geochemical trends consistent with field and petrographic observations from this and previous studies in the area suggesting crustal and mantle derived host rock protoliths. Sub-alkaline amphibolite with diorite migmatite and stromatic Grt-Bt-Sil gneiss neosomes show S-type peraluminous granitoids (Fig. 13) that resemble the paragneiss (Grt-Bt-Sil gneiss from this study) and the Chevreuil and Kensington-Skootamatta plutonic suites defined by Corriveau et al. (1990; 1996) and Corriveau and Gorton (1993) in the Otter Lake area.

Based on field, petrographic and geochemical observations, the provenance of the injected neosomes source seem to reflect a metamorphic source, commonly associated with the breakdown of plagioclase during partial melting. Fluid-rich injected leucosomes from the amphibolite and diorite migmatite and the cross-cutting monzonite and quartz-monzonite granitoids from Grt-Bt-Sil gneiss reveal high-Al slab-derived tonalite-trondhjemite-granodiorite (TTG) melts whereas the in situ neosomes reflect a mantle-derived arc signature.

	Suite 1: Amphibolite with associated diorite migmatite					Suite 2: K-feldspar gneiss			Suite 3: Grt-Bt-Sil gneiss				
Sample	08-07-09-4	08-07-09-2	08-07-09-5	08-07-09-3	12-06-09-1	08-07-09-6	08-07-09-7	08-07-09-8*	12-06-09-5	12-06-09-6	09-07-09-1A	09-07-09-2	09-07-09-3A
Migmatite	Paleosome	Paleosome	Leucosome	Leucosome	Leucosome	Leucosome	Melanosome	Pegmatite	Leucosome	Melanosome	Leucosome	Melanosome	Melanosome
Emplacement			In situ	In situ	Injected	Injected	Injected	Injected	Injected	Injected	In situ	In situ	In Situ
Lithology	Amphibolite	Amphibolite	Diorite	Granodiorite	Mnz Granodiorite	Qtz-Monzonite	Monzonite	Syenite	Mnz Qtz-monzonite	Monzonite	Granite	Mnz-Grt Monzonite	Mnz-Grt Qtz-monzonite
Thin Section	8794	8792	RAC6/9	8793	RAC22	RAC2	RAC1	8798*	12695	RAC18	RAC10	RAC13	RAC3/8
SiO_2 (wt%)	47.90	49.40	62.60	69.40	66.10	69.50	53.30	62.40	68.70	62.20	72.40	59.60	63.20
TiO_2	0.39	0.28	0.12	0.01	0.17	0.22	1.41	0.25	0.21	0.53	0.07	0.68	0.66
Al_2O_3	12.60	13.60	14.30	16.10	14.20	13.90	13.30	14.22	16.30	14.50	15.00	14.80	14.70
Fe_2O_3	7.49	6.59	2.42	0.38	1.78	1.62	7.35	3.94	1.08	3.16	1.04	4.08	4.08
MnO	0.14	0.10	0.03	0.01	0.02	0.02	0.08	0.06	0.02	0.05	0.01	0.02	0.03
MgO	9.50	8.40	4.10	0.80	2.50	0.90	4.40	1.94	0.80	2.00	0.10	1.40	1.40
CaO	9.60	7.40	3.30	2.70	1.70	0.30	3.70	2.46	1.30	1.70	0.60	1.50	1.50
Na_2O	2.70	2.80	2.90	4.00	2.80	1.60	3.20	1.98	2.70	2.70	1.80	2.30	2.40
K_2O	0.93	1.51	2.90	2.26	3.02	8.01	3.65	7.50	6.27	4.93	7.20	5.01	5.23
P_2O_5	0.03	0.03	0.01	0.00	0.00	0.02	0.98	0.07	0.04	0.22	0.19	0.22	0.23
LOI	8.00	9.00	7.00	4.00	7.50	3.50	8.00	4.40	2.00	7.50	1.00	10.00	6.00
Total	**99.28**	**99.11**	**99.68**	**99.66**	**99.79**	**99.59**	**99.37**	**99.22**	**99.42**	**99.49**	**99.41**	**99.61**	**99.43**
Cr (ppm)	426.00	187.30	50.30	73.00	26.50	0.20	47.60	100.32	3.30	10.90	bdl	18.00	15.10
V	123.60	82.80	23.70	7.00	15.90	9.20	118.10	44.96	10.10	35.70	5.60	46.90	49.60
Ni	43.40	37.80	17.60	bdl	5.70	2.60	28.00	6.48	4.50	11.00	bdl	8.90	8.20
Rb	16.60	40.90	51.20	36.70	80.10	212.40	133.90	416.68	131.70	139.80	161.30	145.00	150.10
Sr	181.40	193.90	235.30	212.50	126.30	389.60	1196.50	426.98	589.50	423.30	118.00	111.60	122.90
Ba	134.40	186.70	1219.30	508.00	384.80	1187.90	1466.60	920.48	1676.40	826.10	735.30	636.90	768.90
Y	30.30	14.30	2.10	0.80	1.00	14.30	31.10	51.82	2.40	17.90	15.10	39.70	40.90
Zr	26.80	24.70	85.20	131.90	88.50	261.30	329.10	30.82	96.80	140.40	56.30	328.10	340.60
Nb	7.20	4.30	1.70	0.70	2.70	3.30	14.20	36.22	3.40	9.80	3.80	11.80	11.30
La	6.99	6.50	5.34	4.14	10.67	59.30	143.26	42.28	37.42	101.90	10.87	47.66	44.69
Ce	16.78	13.46	8.14	6.05	15.71	132.88	277.63	82.87	64.99	204.85	23.56	102.47	97.76
Pr	2.46	1.77	0.88	0.59	1.67	15.22	30.64	9.39	7.63	22.65	3.26	14.04	14.07
Nd	11.85	7.88	3.44	2.02	5.46	58.63	122.55	33.23	25.98	80.99	14.77	62.60	59.79
Sm	4.00	2.47	0.89	0.30	0.58	10.57	20.90	6.84	3.84	13.79	4.57	15.62	14.17
Eu	0.85	0.79	0.86	0.52	0.37	1.46	4.26	1.14	1.65	1.76	2.44	2.81	2.57
Gd	4.65	2.55	0.75	0.30	0.73	9.39	17.65	6.90	3.27	11.59	5.23	14.93	13.92
Tb	0.85	0.44	0.11	0.03	0.07	1.14	1.91	1.09	0.35	1.42	0.95	2.15	2.14
Dy	5.51	2.68	0.63	0.17	0.34	5.01	8.44	6.56	1.38	6.47	5.06	11.12	11.33
Ho	1.20	0.57	0.14	0.04	0.06	0.89	1.56	1.45	0.23	1.18	0.79	2.11	2.15
Er	3.78	1.79	0.48	0.16	0.20	2.27	4.79	4.60	0.65	3.24	1.88	6.40	5.91
Tm	0.54	0.25	0.06	0.02	0.02	0.27	0.55	0.75	0.06	0.39	0.21	0.82	0.83
Yb	4.11	1.93	0.56	0.24	0.26	2.10	3.88	5.95	0.51	2.70	1.44	5.87	6.00
Lu	0.58	0.27	0.09	0.04	0.04	0.32	0.54	0.87	0.07	0.36	0.19	0.83	0.84
Pb	5.70	10.30	17.00	11.90	12.60	25.80	27.80	35.18	40.70	33.20	25.30	20.30	20.40
Th	1.10	bdl	1.30	bdl	4.70	10.30	17.70	48.20	11.20	24.00	1.70	8.60	7.00
U	bdl	0.10	1.50	0.00	2.30	1.60	4.20	6.66	1.70	5.60	1.70	2.00	1.90

Table 2: Representative sample compositions from each Suite (1-3), based on whole-rock XRF and ICP-MS analyses. * Average of 5 pegmatite fractions. Mineral abbreviations from Whitney and Evans (2010); bdl: below detection limit; LOI: loss on ignition.

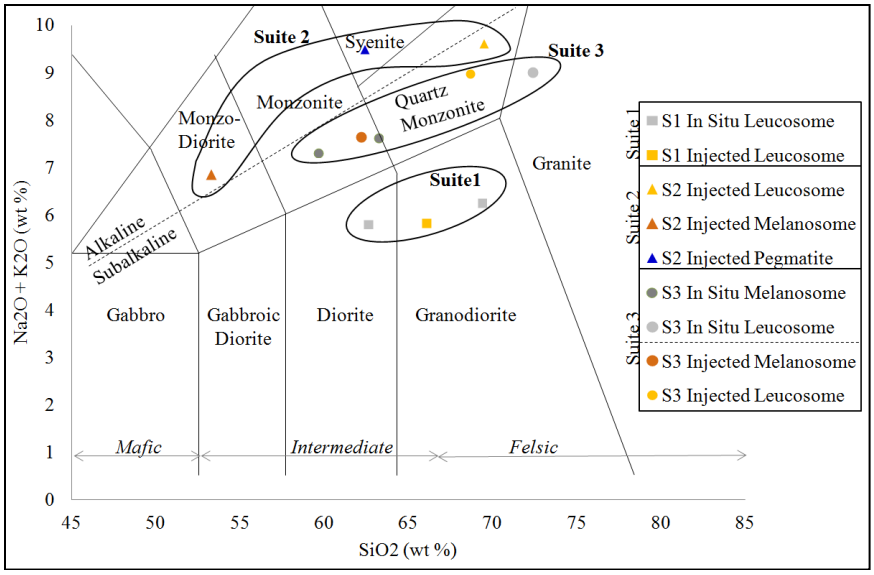

Figure 11: Total alkali vs. Silica (TAS) classification diagram of neosome samples from the Otter Lake area, after Middlemost (1994): in situ and injected leucosomes from Suite 1 (S1, squares), injected neosomes from Suite 2 (S2, triangle) and in situ and injected neosomes from Suite 3 (S3, circles). Paragneiss, Chevreuil and Kensington-Skootamatta plutonic suites (teal outline) defined by Corriveau et al. (1990, 1996) and Corriveau and Gorton (1993). Values and sample names summarized in Table 2.

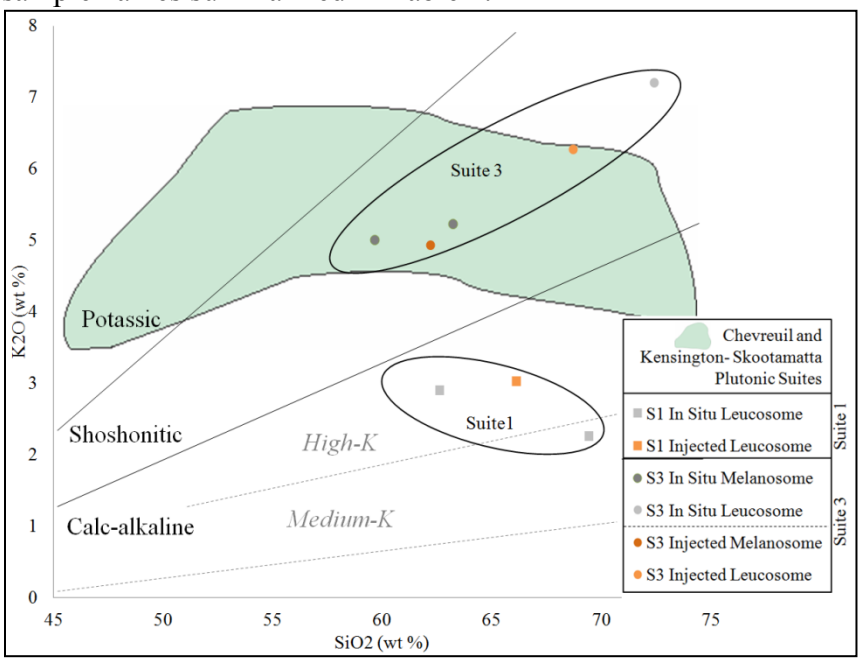

Figure 12: The K_2O vs. SiO_2 classification diagram, which is used to classify the subalkaline rocks, the in situ leucosomes from Suite 1 (S1, squares) samples are mainly medium-K to high-K calc-alkaline in character whereas the injected neosomes from Suite 3 (S3, circles) are shoshonitic in character, after Peccerillo and Taylor (1976). Paragneiss, Chevreuil and Kensington-Skootamatta plutonic suites (teal outline) defined by Corriveau et al. (1990, 1996) and Corriveau and Gorton (1993).

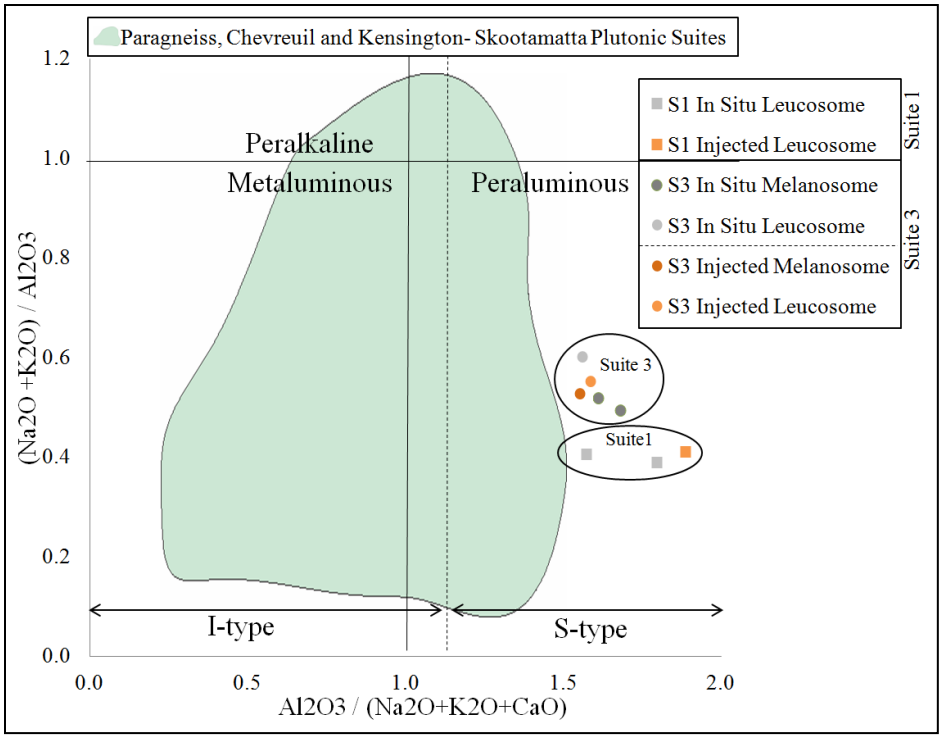

Figure 13: Alumina Saturation Indices (ASI) classification diagram for the peraluminous, S-type character for both the in situ leucosomes from the amphibolite and diorite migmatite from Suite 1 (S1, squares) and the injected leucosome and melanosome from the Grt-Bt-Sil gneiss, Suite 3 (S3, circles). Paragneiss, Chevreuil and Kensington-Skootamatta plutonic suites (teal outline) defined by Corriveau et al. (1990, 1996) and Corriveau and Gorton (1993). Igneous (I-) and Sedimentary (S-) type granitoids after Shand (1927) and Chappell and White (1974).

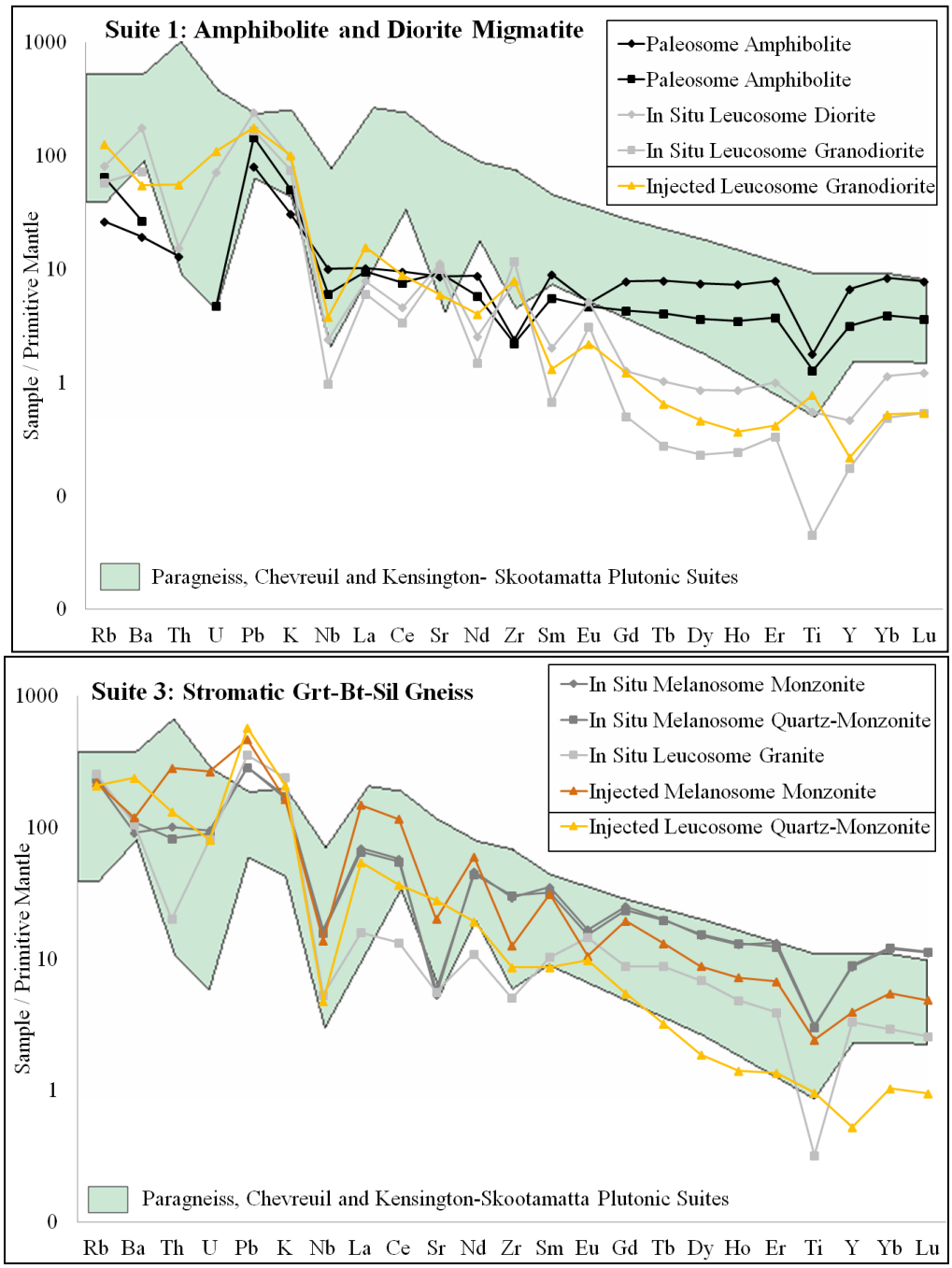

Figure 14: Primitive mantle normalizing diagrams (normalizing values from Sun and McDonough 1989) for the amphibolite and diorite migmatite (top) and stromatic Grt-Bt-Sil gneiss (bottom) compared to the Skootamatta plutonic suite (teal area) from Corriveau et al. (1990). Note the relative depletion of Nb and Ti for all samples, except Ti enrichment for the injected granodiorite leucosome. The grey-shaded normalized patterns represent the in situ neosomes; whereas the orange-shades normalized patterns represent the injected neosome samples. Paragneiss, Chevreuil and Kensington-Skootamatta plutonic suites (teal outline) defined by Corriveau et al. (1990, 1996) and Corriveau and Gorton (1993).

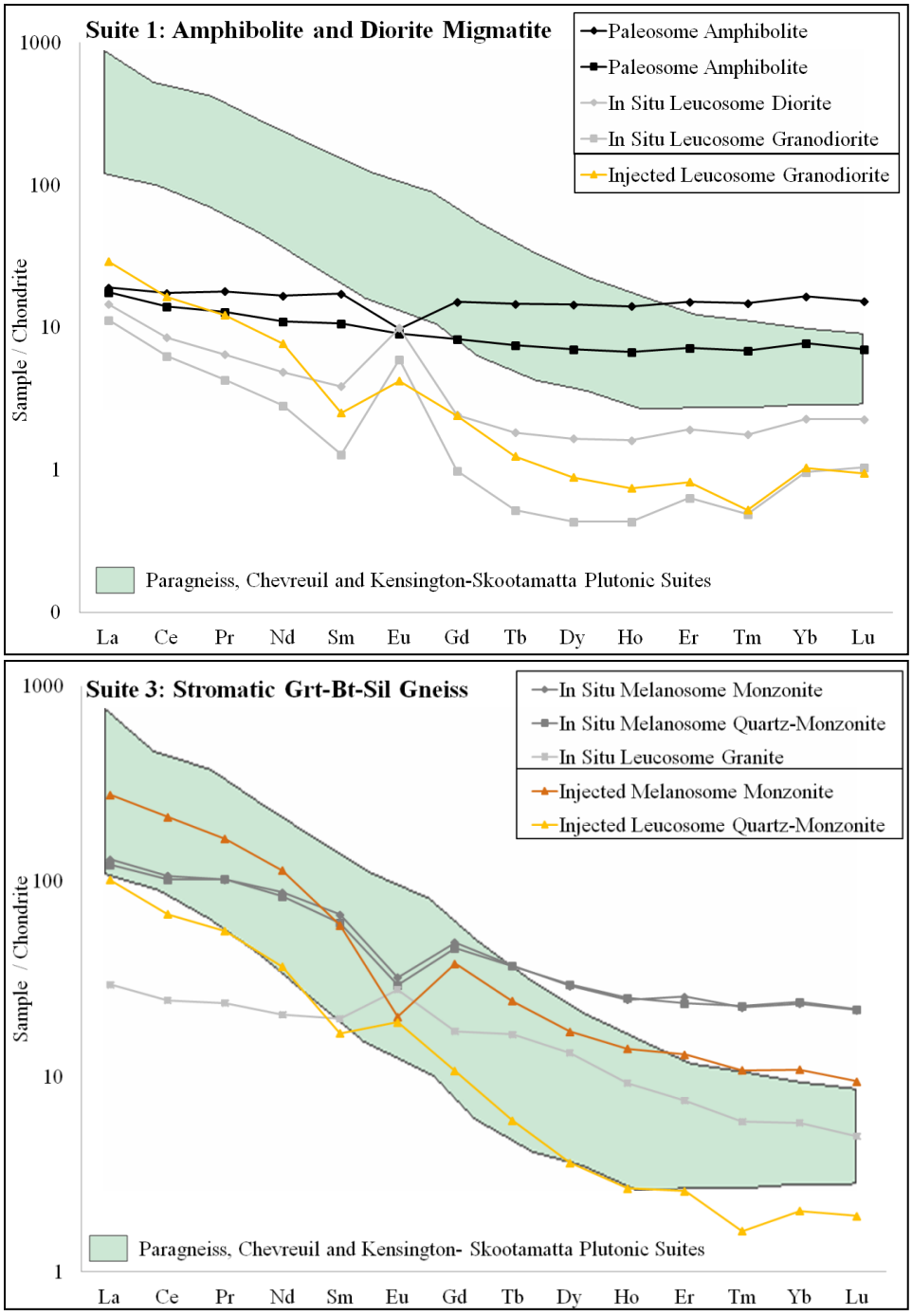

Figure 15: Chondrite-normalized REE patterns of whole-rock samples from amphibolite and diorite migmatite (top) and stromatic Grt-Bt-Sil gneiss (bottom) compared to the Skootamatta plutonic suite (teal area) from Corriveau et al. (1990). The black lines (paleosomes), light and dark grey shades represent in situ (leucosomes and melanosome, respectively); light and dark orange shades represent injected leucosome and melanosomes, respectively. Chondrite values are from Taylor and McClennan (1985). Paragneiss, Chevreuil and Kensington-Skootamatta plutonic suites (teal outline) defined by Corriveau et al. (1990, 1996) and Corriveau and Gorton (1993).

Table 3: Trace and rare earth element data (in ppm) for the studied in situ and injected neosomes found within Suites 1 and 3 from Otter Lake. Values normalized to Taylor and McLennan (1985). Mineral abbreviations are after Whitney and Evans (2010).

	Suite 1: Amphibolite with associated Diorite Migmatite					**Suite 3: Stromatic Grt-Bt-Sil Gneiss**				
Sample	08-07-09-4	08-07-09-2	08-07-09-5	08-07-09-3	12-06-09-1	12-06-09-5	12-06-09-6	09-07-09-1A	09-07-09-2	09-07-09-3A
Migmatite	Paleosome (melanosome)	Paleosome (mesosome)	Leucosome	Leucosome	Leucosome	Leucosome	Melanosome	Leucosome	Melanosome	Melanosome
Emplacement			In situ	In situ	Injected	Injected	Injected	In situ	In situ	In Situ
Lithology	Amphibolite	Amphibolite	Diorite	Granodiorite	Mnz Granodiorite	Qtz-monzonite	Monzonite	Granite	Grt Monzonite	Grt Qtz-monzonite
Thin Section	8794	8792	RAC6/9	8793	RAC22	12695	RAC18	RAC10	RAC13	RAC3/8
Sr/Y	5.99	13.56	112.05	265.63	126.30	245.63	23.65	2.81	3.00	7.81
ΣREE	64.15	43.35	22.37	14.62	36.18	251.88	89.65	75.22	289.43	276.17
$(Eu/Eu^*)_N$	0.60	0.96	3.22	5.31	1.72	1.43	0.43	1.52	0.56	0.56
$(La/Yb)_N$	1.15	2.28	6.41	11.69	28.21	49.73	25.50	5.11	5.49	5.04
$(Ce/Yb)_N$	1.06	1.81	3.74	6.54	15.93	33.12	19.66	4.25	4.52	4.22

(a)

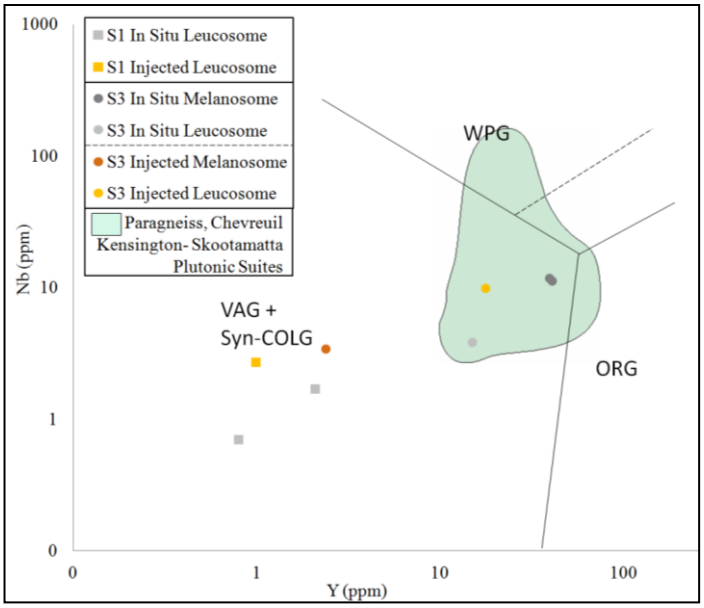

(b)

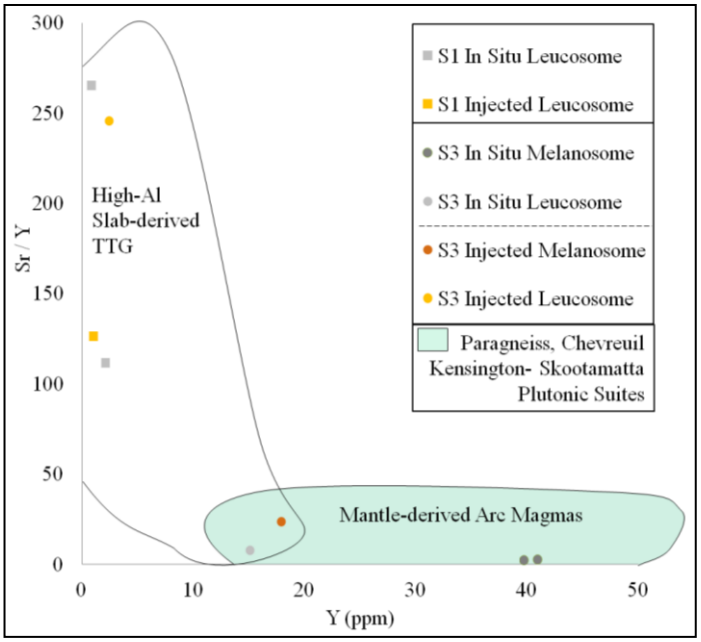

Figure 16: Trace element discrimination of tectonic granitoids (neosomes) diagrams. (a) Nb versus Y discrimination diagram for the in situ and injected neosomes from the two studied suites: amphibolite and dioirite migmatite and stromatic Grt-Bt-Sil gneiss within the Otter Lake area where all samples plot within the volanic arc granitoids and syn-collisiona field. Geochemical fields after Pearce et al. (1984). Volcanic-arc granitoids (VAG), within-plate granitoids (WPG), orogen-related granitoids (ORG), syn-collisional granitoids (syn-COLG). (b) Sr/Y versus Y (after Brown and Solar 1998) discrimination diagram for the in situ and injected neosomes from the two studied suites: amphibolite and dioirite migmatite S1 (Suite 1) and stromatic Grt-Bt-Sil gneiss S3 (Suite 3). The injected leucosomes plot within the "High-Al Slab-derived Tonalite-Trondhjemite-Granitoid (TTG)" field whereas the injected melanosome and in situ neosomes plot in the mantle-derived arc magma field. Teal area defines the paragneiss and Chevreuil & Kensington-Skootamatta plutonic suites (after Corriveau et al. 1996).

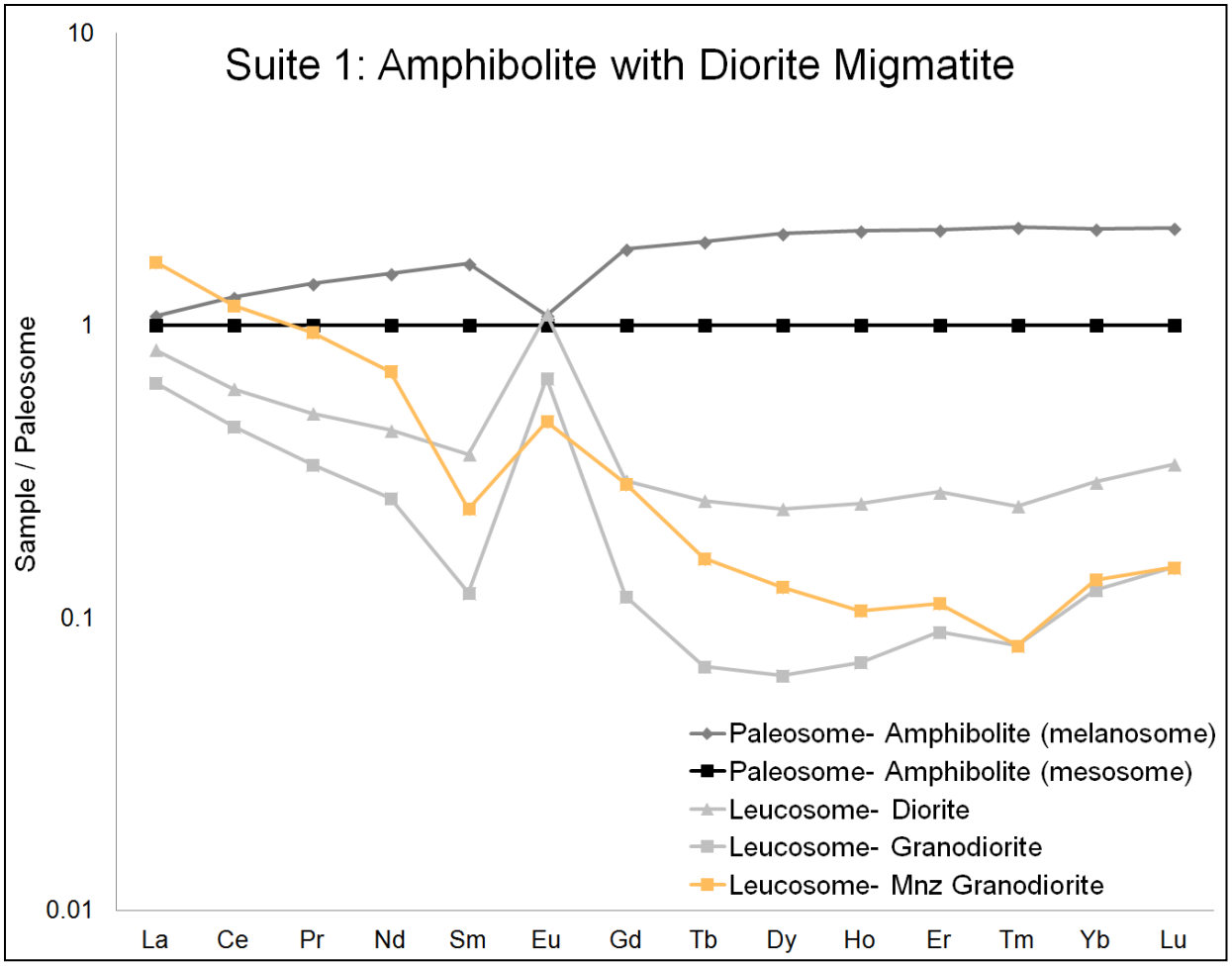

Figure 17: Protolith-normalized REE patterns of injected (orange) and in situ (light grey) leucosomes from the amphibolite with diorite migmatite, Suite 1. The protolith composition for normalization is the amphibolite (mesosome) paleosome. The (melanosome) paleosome has a negative Eu anomaly, but the protolith-normalized abundances of REE-depleted in situ leucosomes show positive Eu anomalies, with slightly negative Sm anomaly for the monazite-free granodiorite leucosome; whereas the injected leucosome lacks a Eu anomaly but does have a negative Sm and Tm anomaly. All leucosomes show relative fractionation of LREE over HREE and a concave-up HREE pattern

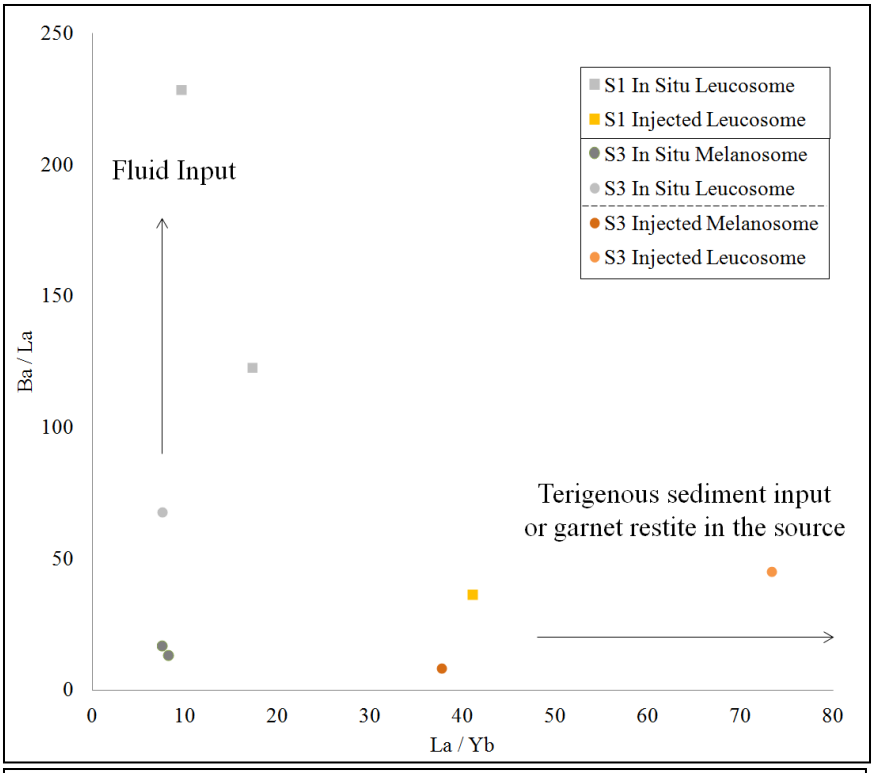

(a)

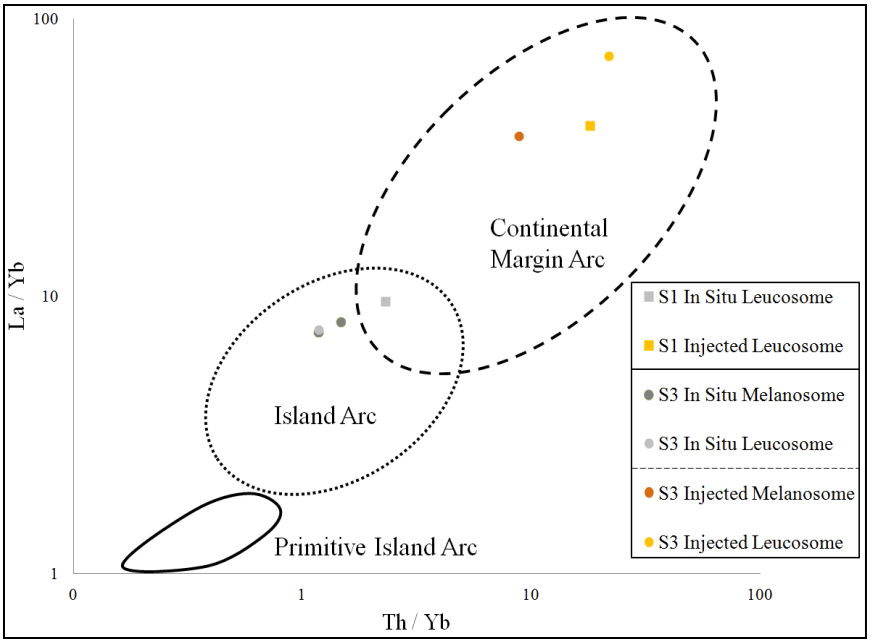

(b)

Figure 18: (a) Ba/La versus La/Yb for the analyzed neosomes from Suites 1 and 3. Suggesting injected neosomes (orange and red) from both Suite 1 and 3 are either enriched with terigenous sediments or represent garnet restite in the source whereas the in situ neosomes (grey) fall along the fluid input trend (Pearce et al. 1984). (b) La/Yb versus Th/Yb geotectonic discrimination diagram after Condie (1989) where the in situ neosomes from Suite 1 and 3 plot within the island arc tectonic discrimination diagram, whereas injected neosomes from Suites 1 and 3 plot in the continental margin arc tectonic field. Note there are no in situ leucosome values for the 8975 sample from Suite 1, because Th falls below the detection limit.

CHAPTER 6: GARNET MINERAL ANALYSIS

Monazite occurs as inclusions in minerals, particularly biotite and garnet. Because monazite is included in garnet, the growth and deformation history of the garnet can yield insight into the significance of U-Th-Pb chemical ages of the included monazites (e.g. Tuccillo et al. 1990; Kohn et al. 2005). Major element zoning and element distribution maps of garnet in the metapelitic gneisses (Suite 3) was determined in order to characterize the chemical variations preserved in different textural settings. In this study, the main characteristics of garnet are related to their petrographic location, geochemistry, and geochronology from the pelitic and migmatite gneisses and their association with monazite within the Otter Lake area.

Major and trace element distribution maps (Fe, Mg, Mn, Ca, Na, P, Y, Ti, Si, Al) were collected from six garnets, two per thin section (RAC3, RAC8, and RAC13), within three samples from the in situ melanosome, within the stromatic Grt-Bt-Sil gneiss (Suite 3). Note that RAC3 and RAC8 are from the same hand sample garnet quartz-monzonite. Two garnet samples per thin section (RAC3-1, RAC3-2, RAC8-1, RAC8-2, RAC13-1, and RAC13-2) were selected based on garnet size and textural location within the melanosome (Fig. 19). The major and trace element zoning profiles are schematically depicted in Figs. 20 - 22.

Composition Profiles of Garnet

Six chemical traverses of garnets from the metapelitic Grt-Bt-Sil gneiss were analyzed in order to document chemical zoning (Figs. 20 – 22). The largest garnets from each sample were analyzed, thereby increasing the likelihood that measured core and rim compositions are representative of zoning patterns in this mineral. The microprobe analyses for garnet data are included in Appendix III and the included CD. A ternary diagram showing the compositional variations of almandine, pyrope, spessartine and grossular (X_{Alm}, X_{Pyp}, X_{Sps} and X_{Grs}, respectively) from each spot analysis from RAC3, 8 and 13 are illustrated in Figure 23.

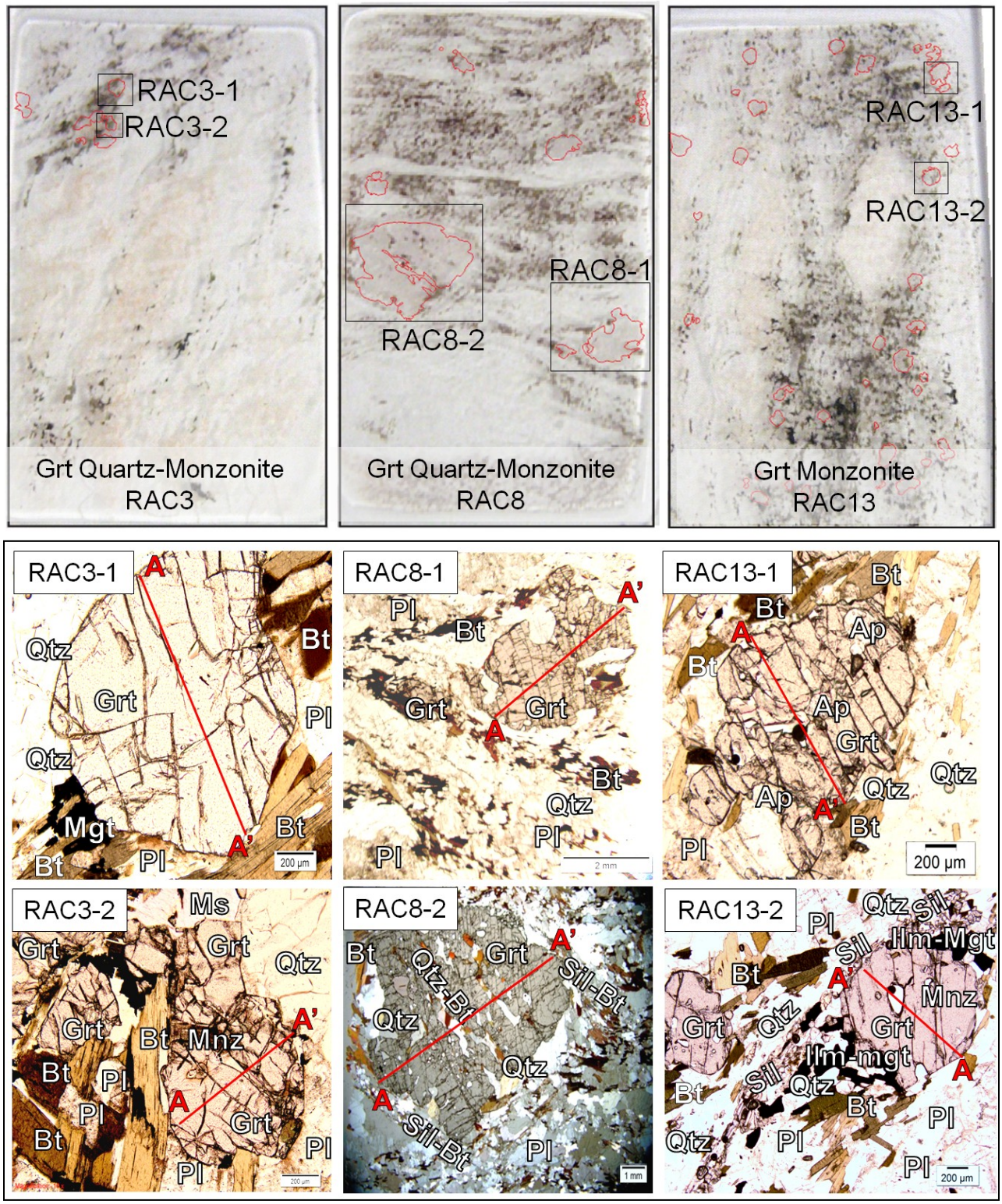

Figure 19: Thin section images from Suite 3 (RAC3, 8, and 13) showing garnet locations outlined in red with sample locations highlighted in boxes with garnet-sample ID. Petrographic images of analyzed garnets showing transect location (red line) along with representative surrounding minerals. Mineral abbreviations are after Whitney and Evans (2010).

Chemical totals on individual garnet analysis spots ranging above or below 7.90 - 8.10 atoms per formula unit (apfu) were rejected. This departure from stoichiometry is believed to be due to the presence of unanalyzed trace and REE elements, impurities (i.e. inclusions) or sample discontinuity (such as a crack), and were thus rejected.

Two petrographically distinct types of garnet are observed (Fig. 10a): large poikiolitic (RAC8) and small subhedral to euhedral (RAC3 and 13) garnets. All analyzed garnets are almandine-rich (X_{Alm}= 69.91 – 88.64 mol %), with moderate amounts of pyrope (X_{Pyp}= 6.26 – 25.40 mol %) and minor spessartine and grossular (X_{sps} = 1.62 – 9.43 and X_{Grs} = 0.00 – 5.63 mol %) concentrations (Table 4). Andradite (X_{Adr}) was present in all samples and was calculated based on measured stoichiometry (Appendix III) but was not presented on the compositional profiles due to very small abundance (up to 4.10 mol %).

The small garnets in RAC3 occur as small subhedral grains, up to 1.5 mm in diameter and contain a small number of included biotite and partially included monazite connected to the matrix (RAC3-2). The smaller RAC3 garnets are represented by asymmetrical zoning as observed on the compositional transects (A-A', Fig. 20a,c). Rimward almandine-enrichment and pyrope-depletion are greater near rim A of RAC3-1 and 2. A noticeable rimward spessartine-enrichment towards rim A in RAC3-1 (Fig. 20a) was also observed. The asymmetrical chemical profiles across these grains could be due to asymmetry of the traverse across the cut garnet grain, strain during orogenesis and/or reactions with adjacent matrix minerals (mineralogy).

The RAC13 garnets suggest two geochemically distinct growth zones (Fig. 22a,c). The first and larger garnet growth stage is more pyrope-rich and almandine-depleted relative to the smaller almandine-enriched second growth zoning (e.g. Fig. 22a,c). The smaller garnets from RAC3 and RAC13 record more grossular up to 5.63 mol% and andradite up to 4.10 mol% values (Fig. 23) relative to the RAC8-1 and RAC8-2 garnets up to 4.55 and 3.81 mol%, respectively (Fig. 22). In general, the garnets from RAC8 record the widest compositional variations (Fig

21). RAC8-1 records the widest compositional range of almandine. Core X_{Alm} values start at 69.91 mol% and increase to 88.64 mol% near the rim. They also have inversely proportional X_{Pyp} in the core, which start at 25.40 mol% and decrease down to 6.98 mol% near the rim. The general zoning trends of the large and small garnets are the same where almandine increases from core to rim to compensate for the decreasing pyrope.

Both the large and small garnet samples occur proximal to or in contact with matrix biotite (Figs. 20 – 22). The smaller garnets are commonly in contact with biotite and to a lesser extent sillimanite (RAC13-2) and magnetite (RAC3-1, 3-2 and 13-2) as shown in Fig. 19. Slight increases in X_{Alm} and decreases in X_{Pyp} occur in garnet profiles adjacent to matrix biotite and magnetite as well as biotite inclusions (Fig. 20a). The X_{Grs} concentrations from all samples show the absence of or very weak zoning with the exception of a slight X_{Grs} increase near an included apatite grain in RAC13-1(Fig. 22a,b). The large (Grt1; RAC8) are geochemically distinct from the smaller (Grt2; RAC3 and RAC13) garnets. Overall these garnets are not homogeneous and exhibit obvious compositional zoning with geochemically distinct growth zones (e.g. Fig. 22a,c).

Major and Trace Element Zoning

The EMPA garnet data is included in Appendix III and the enclosed CD-ROM. In addition elemental maps for major elements (Fe, Mg, Mn, Ca, Si, Al, Ti and K) and trace elements (P and Y) are illustrated in Figure A1 – A6 of the appendix for each analyzed garnet crystal.

Elemental maps from the smaller RAC3 garnet reveal asymmetrical rimward Fe- and Mn-enrichment and mirrored Mg-depletion (Figs. 20c,d). The rimward Mn-enrichment observed in the elemental map cannot be seen on the zoning profiles possibly due to the asymmetry of the zoning and/or the orientation of the garnet crystal (i.e. traverse not through center of crystal). The highest increase in Mn occurs when garnet is in direct contact with surrounding matrix biotite (e.g. Fig. 20b,d). The Ca and Y elemental maps from RAC3-1 also demonstrate

(a)

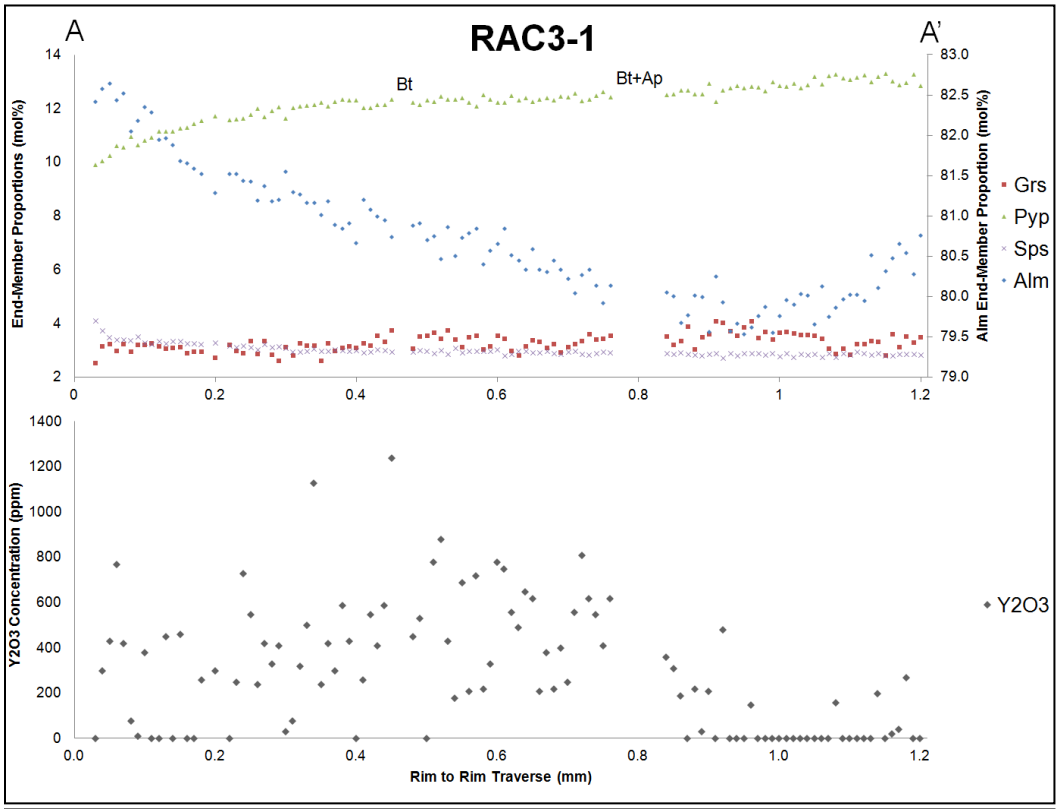

(b)

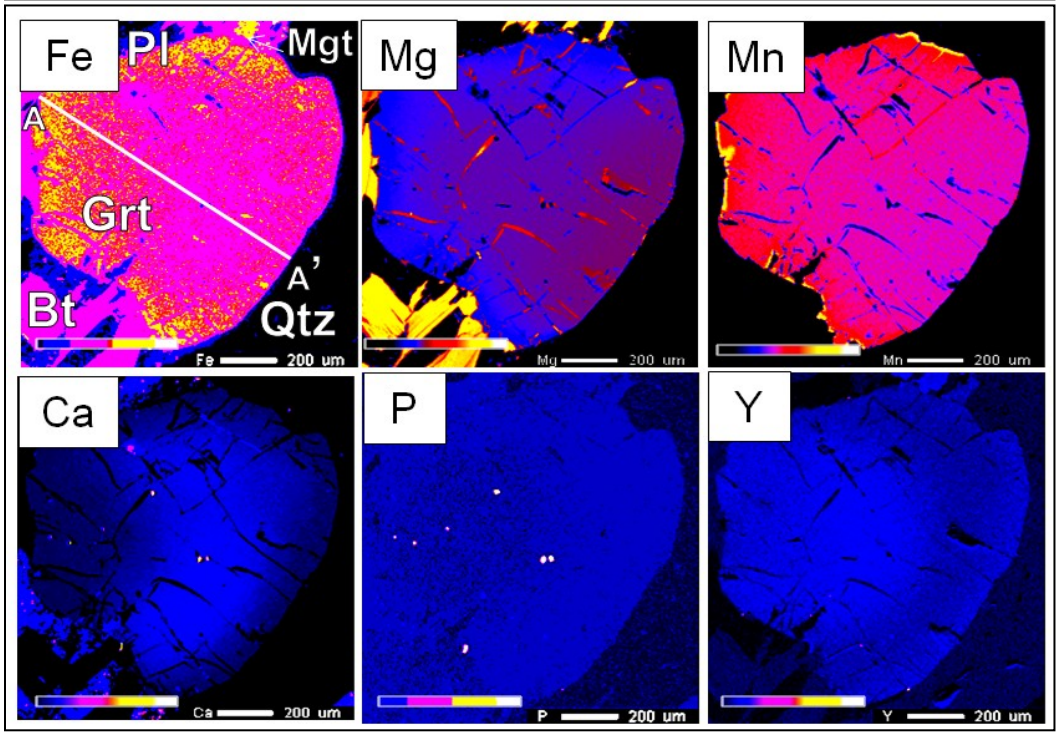

Figure 20: (a, c) Electron microprobe profiles (A - A') across garnets RAC3-1 (a) and RAC3-2 (c) across EMP analyzed garnets from the Grt-Bt-Sil gneiss (Suite 3). Gaps in chemical profiles represent inclusions. Garnet end-member proportions presented in percentage (%): Almandine (Alm); Andradite (And); Grossular (Grs); Pyrope (Pyp); Spessartine (Sps). (b, d) X-ray compositional maps for RAC3-1 (b) and RAC3-2 (d) for Fe, Mg, Mn and Ca in garnet. Note the decrease in Mg and increase in Mn near garnet rim when in contact with biotite. See Appendix III and the included CD for garnet EMPA data; mineral abbreviations after Whitney and Evans (2010). Mineral abbreviations are after Whitney and Evans (2010).

(c)

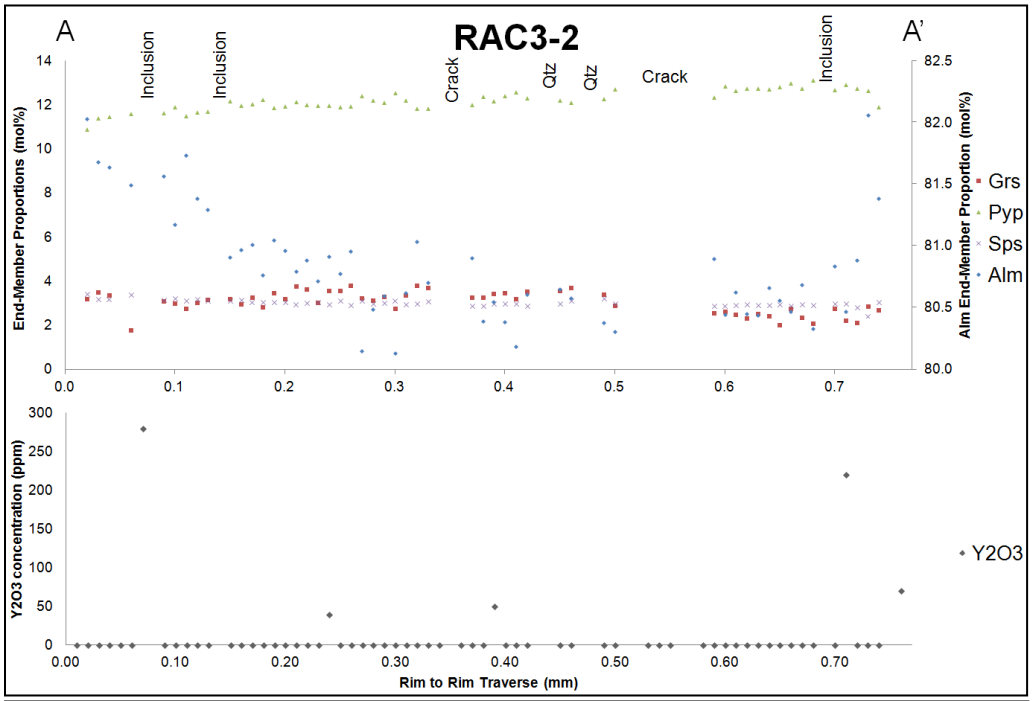

(d)

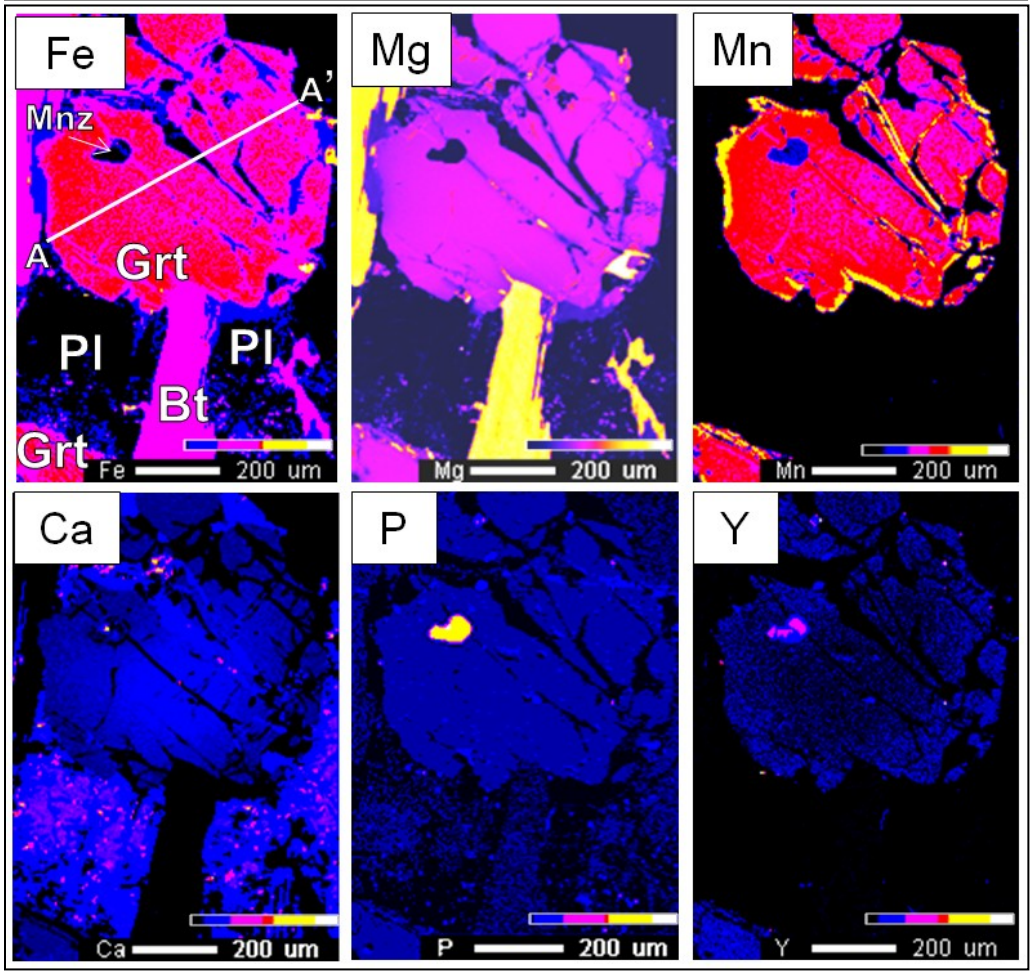

Figure 20: (continued)

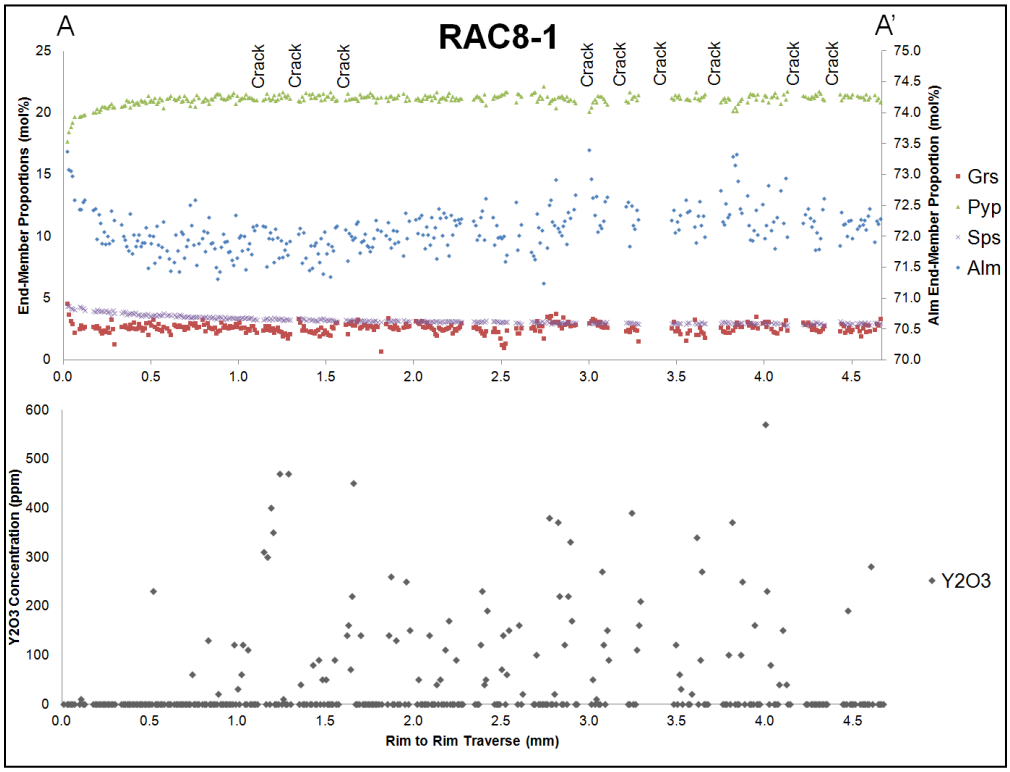

(a)

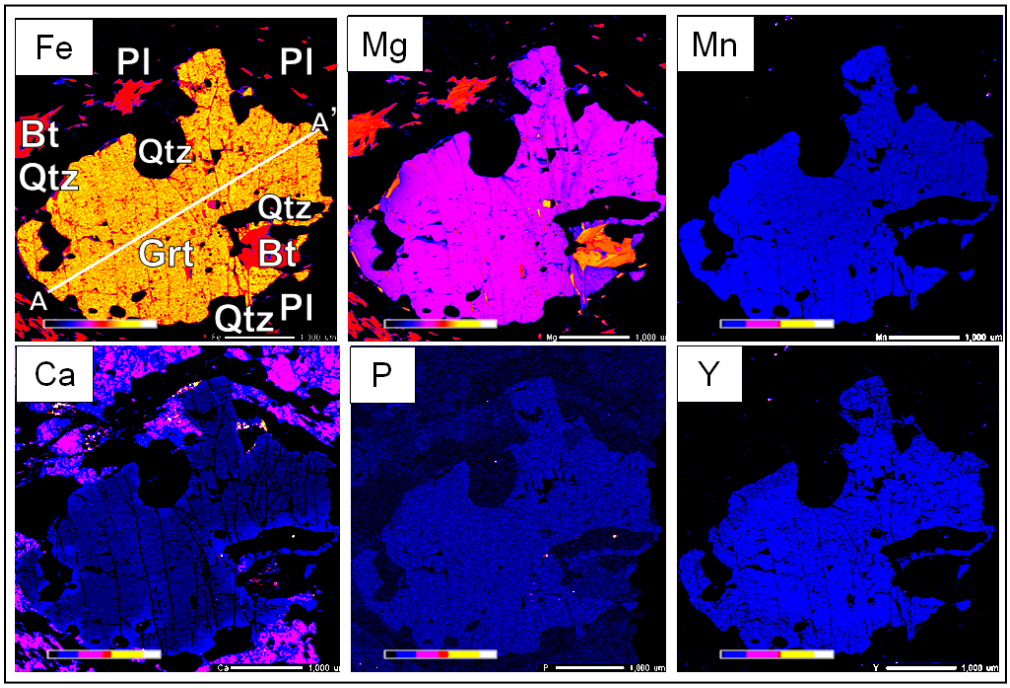

(b)

Figure 21: (a, c) Electron microprobe profiles (A - A') across garnets RAC8-1 (a) and RAC8-2 (c) across EMP analyzed garnets from the stromatic Grt-Bt-Sil gneiss (Suite 3). Cracks and unidentified inclusions are marked as 'cracks' on profile transects (a). Garnet end-member proportions are presented in molar percent (mol%): Almandine (Alm); Andradite (And); Grossular (Grs); Pyrope (Pyp); Spessartine (Sps). (b, d) X-ray compositional maps for Fe, Mg, Mn and Ca from RAC8-1 (b) and RAC8-2 (d) garnets. There is a slight decrease in Mg and increase in Mn near garnet rim (b) from RAC8-1. Fe is inversely correlated to Mg (c) and Mn increases near rim and along the polyphase elongated Qtz + Bt inclusions aligned as trails (center of garnet; d). See Appendix III and included CD for garnet EMPA data; mineral abbreviations are after Whitney and Evans (2010).

(c)

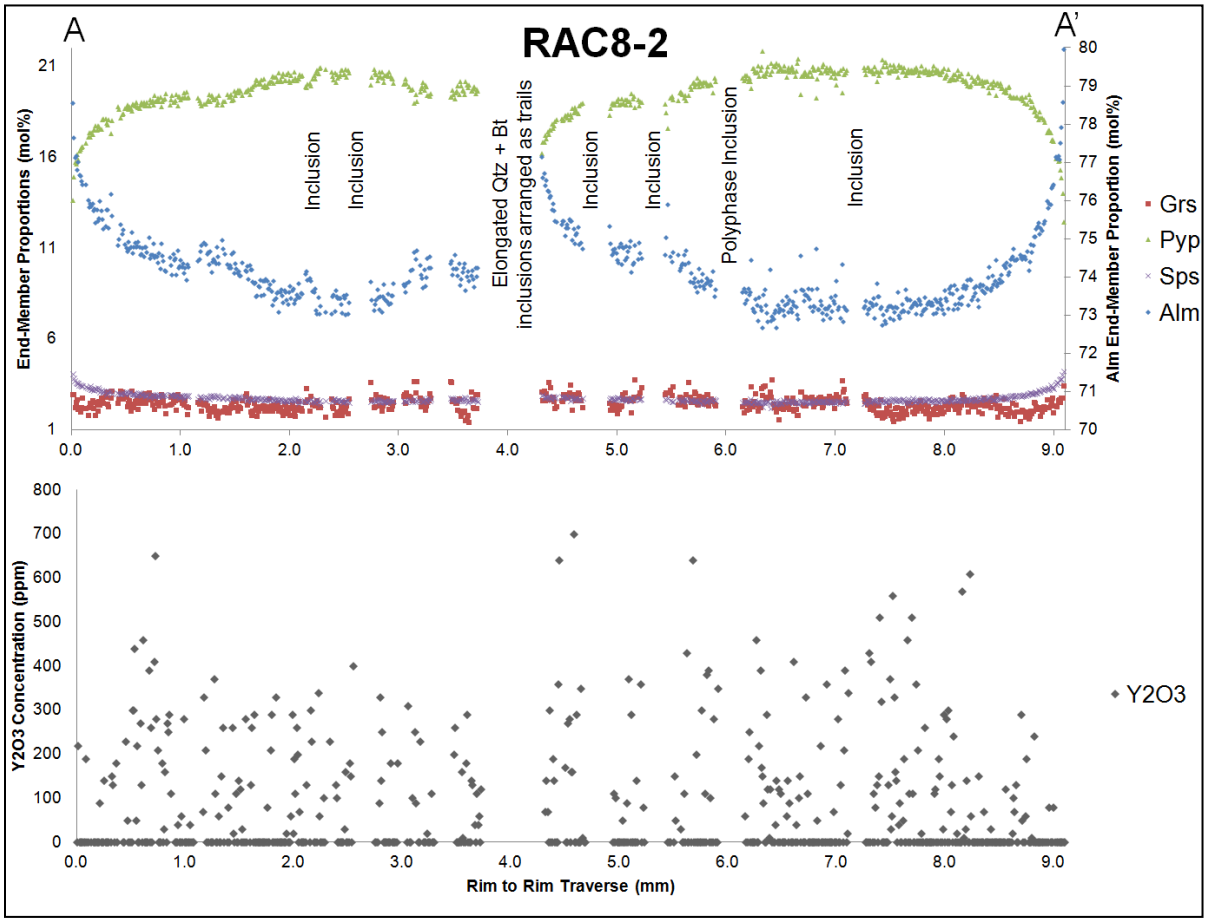

(d)

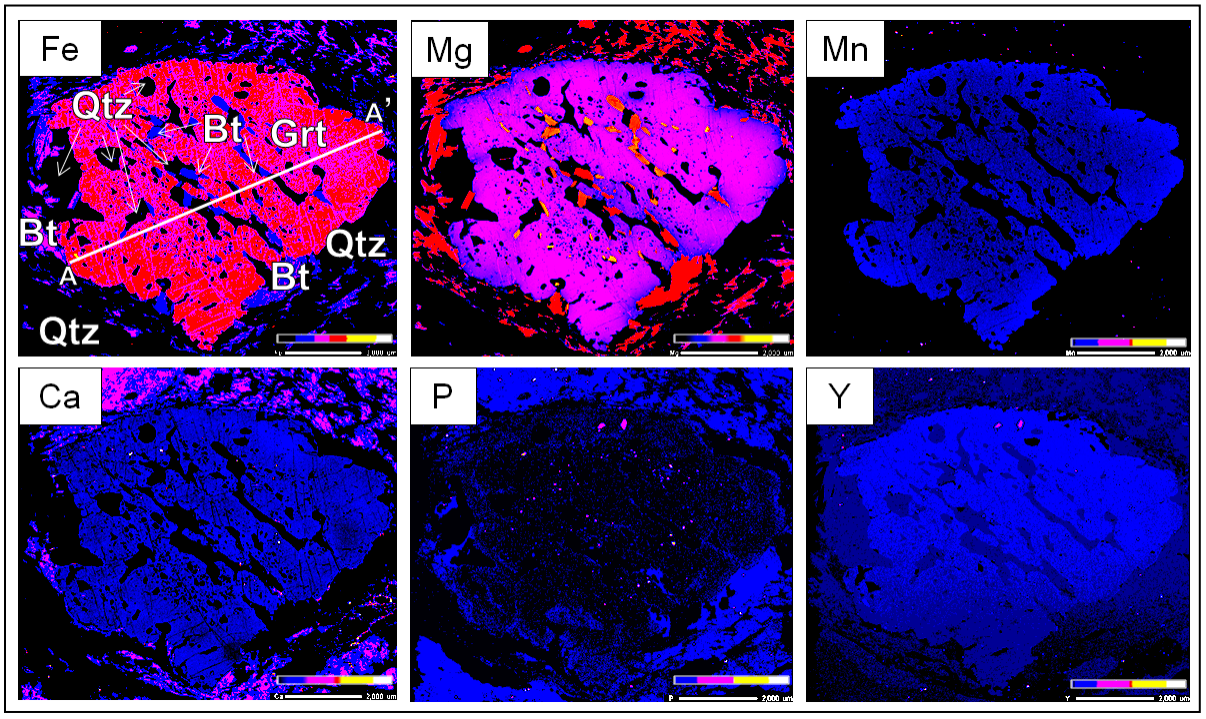

Figure 21: (continued)

(a)

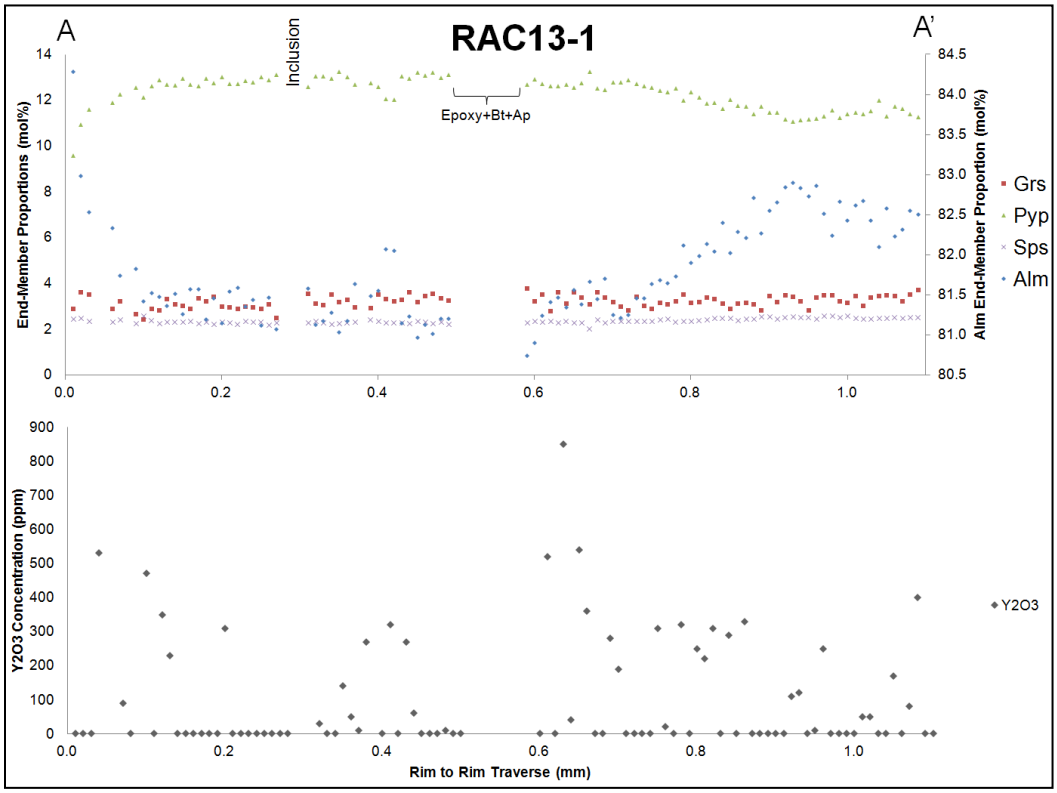

(b)

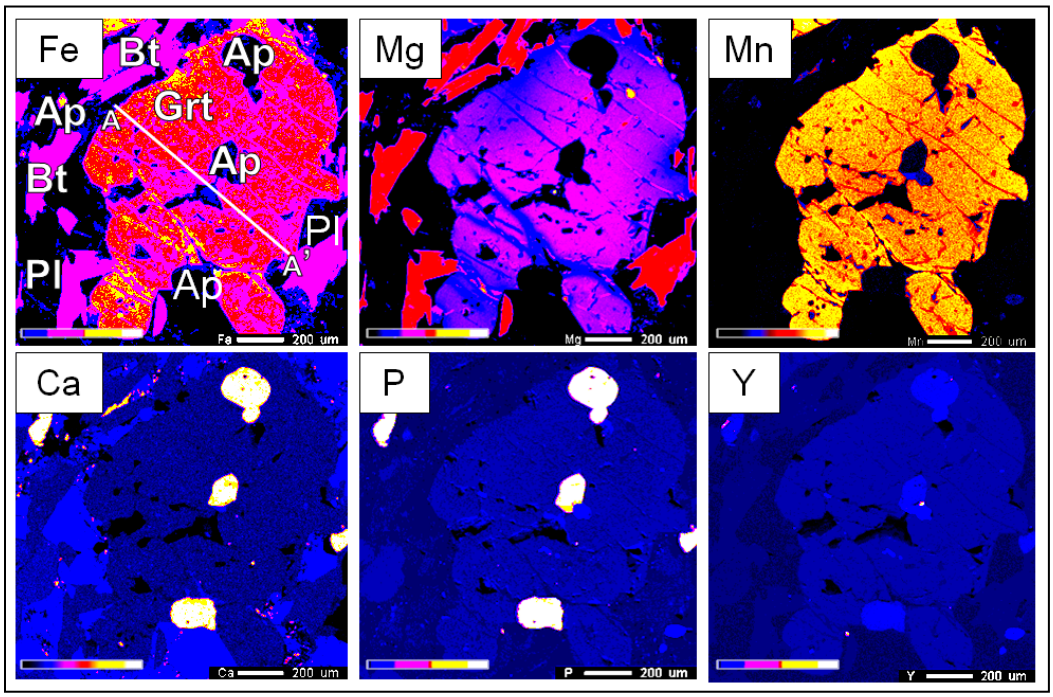

Figure 22: Electron microprobe profiles (A - A') across garnets RAC13-1 (a) and RAC13-2 (c) across EMP analyzed garnets from the stromatic Grt-Bt-Sil gneiss (Suite 3). Gaps in chemical profiles represent mineral inclusions. Garnet molar end-members proportions (mol%): Almandine (Alm); Andradite (And); Grossular (Grs); Pyrope (Pyp); Spessartine (Sps). Grs content increases and Alm decreases in RAC13-1 in contact with apatite inclusion. (b, d) X-ray compositional maps for Fe, Mg, Mn and Ca from RAC13-1 (b) and RAC13-2 (d) garnets. Fe and Mn are both inversely correlated to Mg (b and d). See Appendix III and the included CD for garnet EMPA data; mineral abbreviations are after Whitney and Evans (2010).

(c)

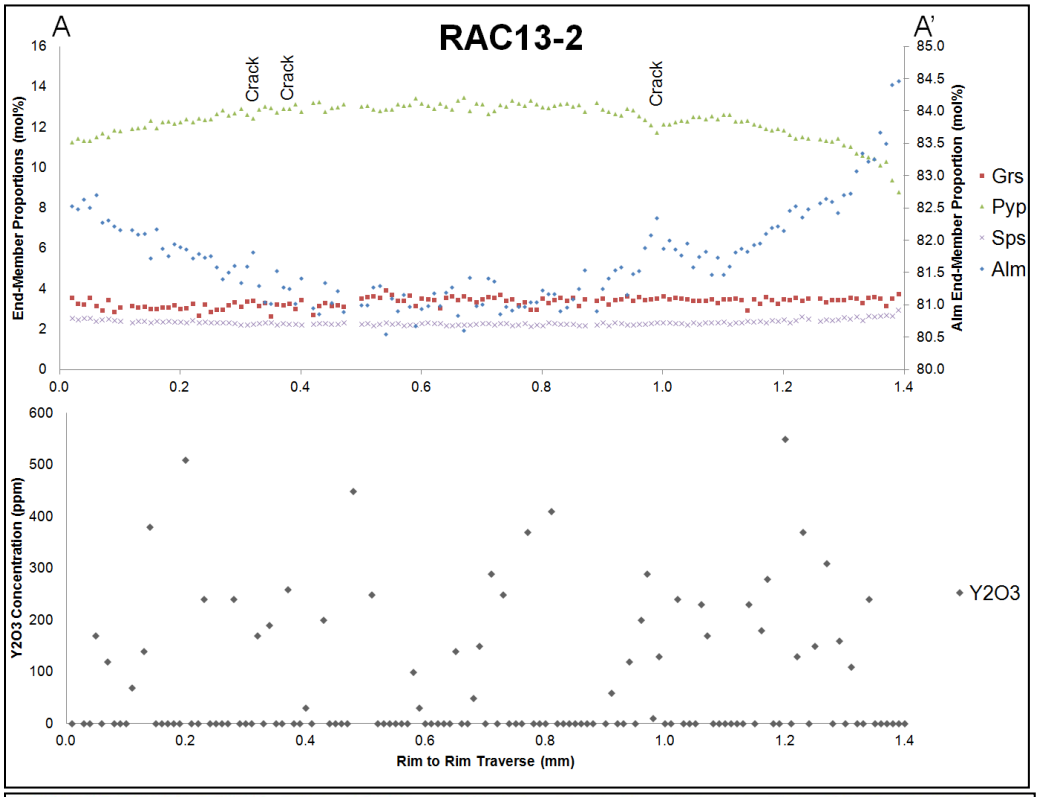

(d)

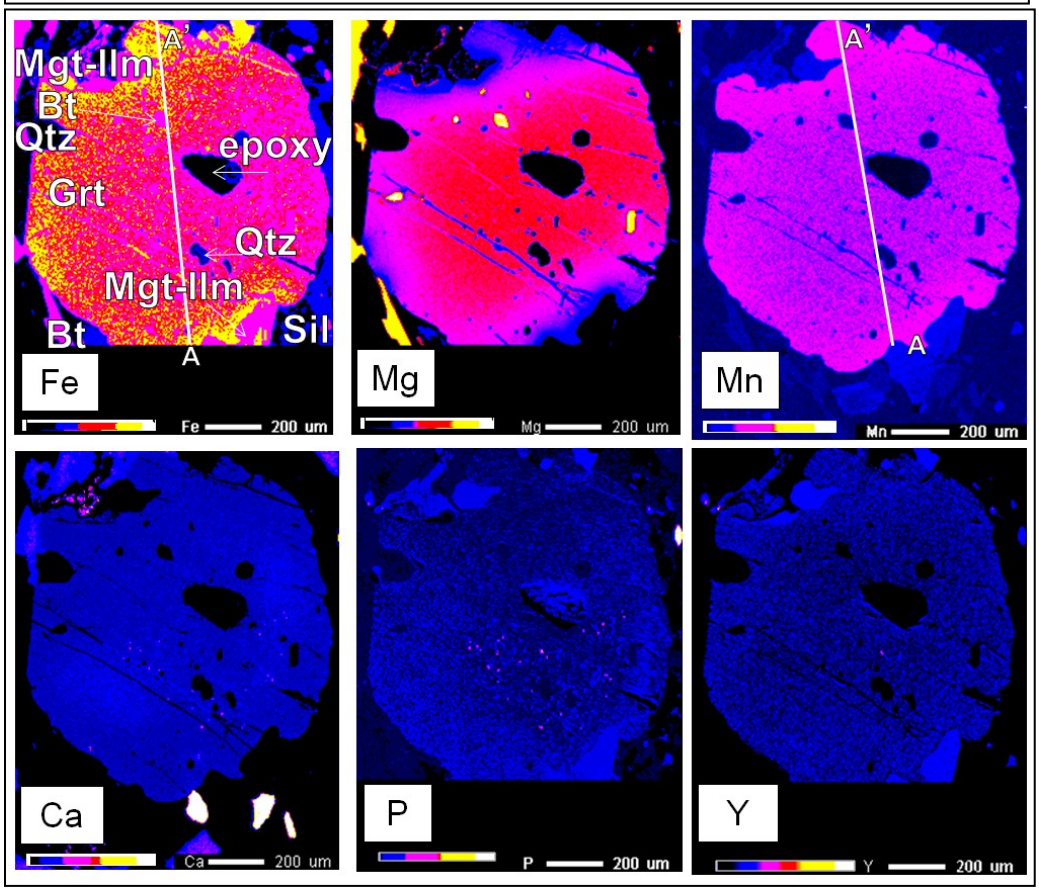

Figure 22: (continued)

(mol %)													
RAC3-1	Alm	Adr	Grs	Pyp	Sps	Y_2O_3	**RAC3-2**	Alm	Adr	Grs	Pyp	Sps	Y_2O_3
AVG	80.75	0.80	3.24	12.18	3.03	284	AVG	81.04	0.81	3.09	11.83	3.23	10
MIN	77.94	0.00	0.57	9.10	2.72	bdl	MIN	80.13	0.00	1.77	6.26	2.43	bdl
MAX	82.67	4.10	5.63	14.43	5.23	1240	MAX	86.58	1.74	4.08	13.12	9.43	280
RAC8-1	Alm	Adr	Grs	Pyp	Sps	Y_2O_3	**RAC8-2**	Alm	Adr	Grs	Pyp	Sps	Y_2O_3
AVG	72.21	0.94	2.61	20.99	3.24	43	AVG	74.28	1.07	2.44	19.48	2.73	68
MIN	70.37	0.00	0.69	8.08	1.87	bdl	MIN	69.91	0.00	0.00	6.98	1.62	bdl
MAX	80.87	2.89	4.55	23.50	6.64	570	MAX	88.64	3.81	3.75	25.40	4.23	700
RAC13-1	Alm	Adr	Grs	Pyp	Sps	Y_2O_3	**RAC13-2**	Alm	Adr	Grs	Pyp	Sps	Y_2O_3
AVG	81.75	0.38	3.17	12.34	2.37	99	AVG	81.76	0.18	3.36	12.34	2.36	69
MIN	79.76	0.00	0.00	9.59	2.02	bdl	MIN	80.55	0.00	2.66	8.80	2.17	bdl
MAX	84.28	3.47	3.78	14.28	2.58	850	MAX	85.05	1.00	3.94	13.48	2.98	550

Table 4: Garnet compositional profile (mol%) and Y_2O_3 (ppm) average (AVG), minimum (MIN) and maximum (MAX) for all electron microprobe spots taken from stromatic Grt-Bt-Sil gneiss samples (Suite 3). Mineral abbreviations are after Whitney and Evans (2010). Appendix III enclosed CD-ROM, for garnet EMPA data.

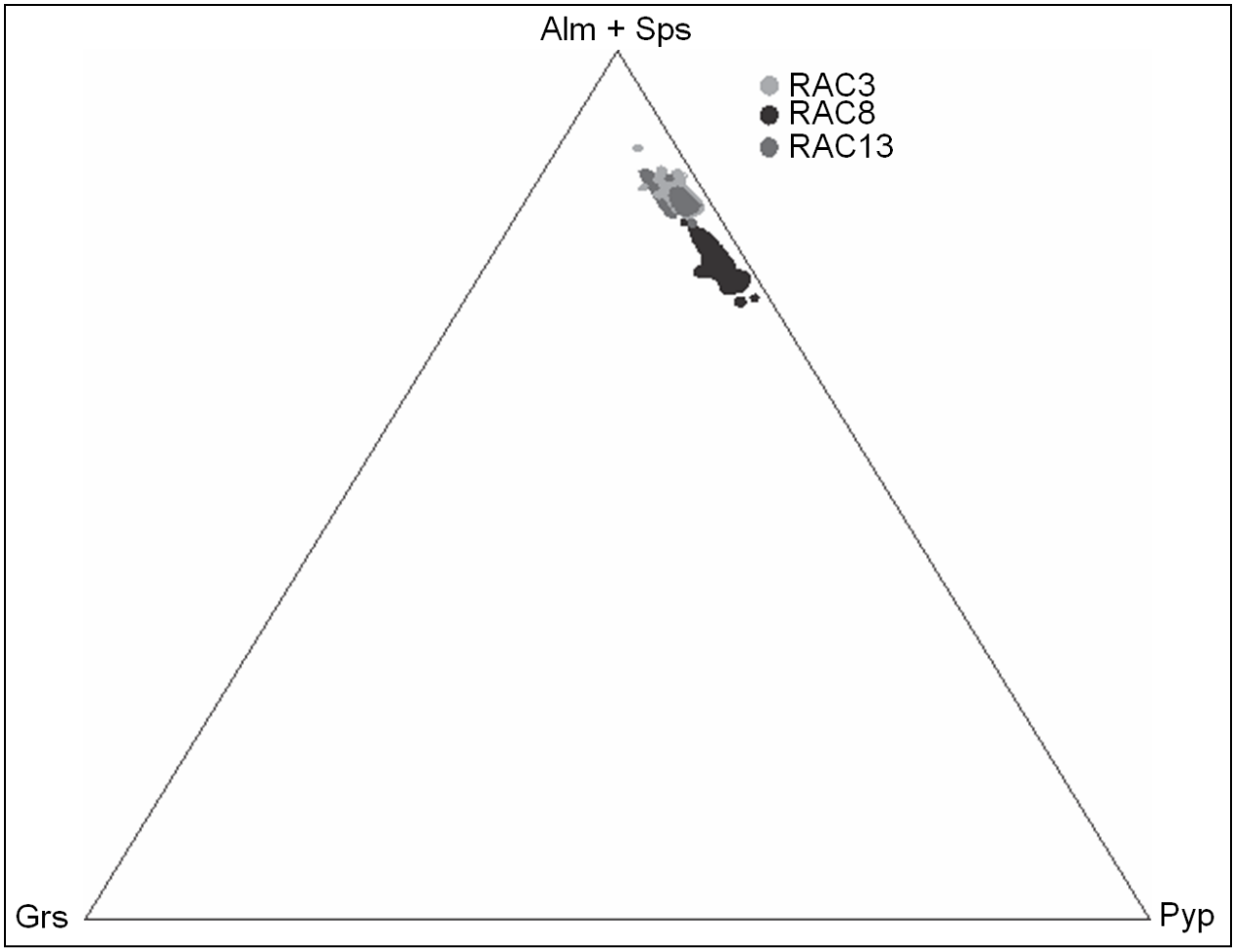

Figure 23: Ternary diagram of garnet variations in composition and between samples (RAC3, 8, and 13) in the Grt-Bt-Sil gneiss from Suite 3 are plotted as a function of almandine (Alm) + spessartine (Sps), pyrope (Pyp), and grossular (Grs) end-members. Note the RAC8 garnets are more pyrope-rich than the RAC3 and RAC13 garnets. Garnet EMPA data available in Appendix III (see enclosed CD-ROM).

asymmetrical zoning. The major element Fe, Mg and Mn distribution maps show well defined features that do not correlate with the Ca, Y, and P maps.

The large garnets from RAC8 have distinct textural features. RAC8-1 has parallel cracks (fractures) and is relatively inclusion free whereas RAC8-2 has parallel, elongated inclusions of biotite and quartz that define an internal fabric orientated oblique to the external foliation (Fig. 10a, Fig. 21 and 23). RAC8-1 has asymmetrical pyrope-depleted rims and cracks relative to the pyrope-rich core. Garnet RAC8-2 has a pyrope- and inclusion-rich, core relative to the more almandine- and spessartine-rich inclusion-poor secondary rim (Fig. 21d). Both rims (A and A') from RAC8-2 and rim (A) from RAC8-1 are spessartine-enriched relative to representative core values.

The external foliation-defining biotite (e.g. RAC8-1) shows grain-size coarsening relative to the smaller included biotite in garnet (Fig. 10a, Fig. 21 and 23) suggesting garnet is a peritectic-phase. Magnetite-ilmenite (RAC13-2) occurs adjacent to garnet and the biotite-sillimanite defined foliation within the matrix (Fig. 20b). Garnet exhibits reverse growth zoning (rimward Mg decrease from 13.48 to 8.80 mol %; Fig. 21). RAC13-1 garnet is the only sample with apatite inclusions, euhedral to subhedral, up to 200 μm in diameter present in the core and rim of the crystal. It should be noted that apatite also occurs in the matrix associated with plagioclase and biotite and is marked by enrichment in Ca and P on the elemental x-ray maps (Fig. 20 and Fig. A5).

Analysis of the trace element zoning in garnet compliments the major-element zoning potentially improving the petrographic and geochronological interpretation. According to Pyle and Spear (1991), trace element zoning in garnet growing in a close system depends on the presence or absence of mineral phases such as xenotime for Y and xenotime, apatite and

monazite for P. Yttrium is potentially useful for monitoring reactions involving Ca-rich minerals such as epidote, allanite, and titanite because this element substitutes for Ca in mineral structures and Y anomalies in garnet zoning may correlate with inflections in Ca zoning. Pyle and Spear (1999) noted that Yttrium partitions strongly into garnet relative to other silicates.

Y_2O_3 concentrations in garnet based on microprobe analyses are up to 1240 ppm (RAC3-1) at 0.45 mm from A on the A – A' traverse. The scattered Y_2O_3 concentrations from RAC3-1 show an asymmetrical trend towards A relative to depleted A' values. The near-rim Y_2O_3 values of RAC3-1 are 770 ppm (0.06 mm from A) decreasing rapidly to 300 ppm (0.03 mm from A), and 270 ppm (1.18 mm from A; 0.03 mm from A'). The highest Y_2O_3 value is from RAC3-1 with 1240 ppm near the core, whereas the lowest Y_2O_3 maxima concentrations observed occur in RAC3-2. RAC3-2 garnet core is Y_2O_3-poor (compared to RAC8 and RAC13) with two annuli of ~ 40 - 50 ppm (0.24 and 0.76 mm from A) on either side of a crack with nearby monazite and slightly higher near-rim 220 - 280 ppm values (0.07 and 0.71 mm) from A on the A-A' transect (Fig. 20c).

The large poikiolitic garnets from RAC8 show large variations of Y_2O_3 contents across each crystal with spikes up to ~ 430 – 650 ppm near the core and near-rim spikes of ~ 220 – 250 ppm (Fig. 21a,d). The A – A' chemical profile across RAC8-1 (Fig. 20a) reveals no clear Y_2O_3 patterns, the largest analysed concentrations show one up to 570 ppm (3.99 mm from A) relative to smaller near-rim concentrations of 280 ppm (4.59 mm from A) and 230 ppm (0.51 mm from A). The chemical profile across RAC8-2 (Fig. 20c) for Y_2O_3 illustrates a near-core Y_2O_3 spike up to ~ 700 ppm (4.57 mm from A), whereas the near-rim concentrations are 230 ppm (0.51 mm from A) and 280 ppm (4.59 mm from A). Hence an overall rimward decrease of Y_2O_3 contents on the chemical traverses is observed for the large, Mg-rich RAC8 garnets.

The analyzed garnet from RAC13-1 reveals a ~ 850 ppm spike near a crack containing apatite (Fig. 22a), decreasing on either side to ~ 310 – 330 ppm at about mid-grain and a slight increase near-rim to ~ 400 – 530 ppm. The garnet (RAC13-2) reveals near core Y_2O_3 spikes of ~ 390 – 450 ppm, decreasing gradually until mid-grain where the Y_2O_3 spikes again to ~ 510 – 550 ppm, and a gradual decrease towards the rim with Y_2O_3 concentrations ~ 170 – 240 ppm (Fig. 22c).

The Y elemental x-ray maps for the analyzed garnets show varying patterns (Figs. 20 – 22). RAC3-1 and RAC8-1 show asymmetrical enrichment of Y from one side of the garnet crystal to the other. RAC3-2 shows near-rim Y enrichment whereas RAC8-1 reveals near-rim depletion. The RAC13 garnet samples show uniform distribution of Y on the element x-ray maps.

The P_2O_5 concentration is almost below the detection limit of EMPA analysis in the garnet but it is significantly concentrated in phosphate minerals such as monazite and apatite, which are recognized as inclusions in garnets (e.g. RAC3-2 and RAC13-1). The measured P_2O_5 concentrations are relatively inversely correlated to Y_2O_3 in the samples; where Y_2O_3 generally decreases and P_2O_5 increases from core to rim, except RAC3-2 (Fig. 20 – 22); (RAC3-1 and RAC3-2) and magnetite-ilmenite (RAC13-1). The white line (Figs. 20 – 22) in the Fe maps indicates the location of the chemical traverses.

Summary of Garnet Chemistry

The focus of this chapter is on the chemical zoning profile and x-ray element maps of selected major (Fe, Mg, Mn and Ca) and trace elements (P and Y) that may be associated with episodes of growth and/or resorption on six garnets from three thin sections within the grt-bt-sil gneiss (Figs. 20 – 22). Two texturally distinct garnet habits have been identified in Suite 3 large

porphyroblasts and smaller garnets. The large garnet crystals are thought to be early nucleates and to have undergone multiple growth periods. The small garnets nucleated later and experienced only one or two growth periods. The ternary diagram (Fig. 23) shows the larger RAC8 garnets are more pyrope-rich relative to the smaller almandine- and spessartine-rich RAC13 and RAC3 garnets.

The chemical profiles and elemental maps reveal distinct major and trace element zoning. The zoning profiles for RAC8-1, RAC13-1 and RAC13-2 show increases in almandine and spessartine and a mirrored decrease in pyrope along garnet rims or next to biotite and magnetite-ilmenite for samples RAC3-1, RAC3-2, and RAC13-2 (Fig. 23). The majority of the garnets have higher near-core grossular contents and increased values near included apatite crystals in RAC13-1(Fig. 22a,b) relative to the depleted near-rim values. The trends of these mole fraction almandine and pyrope profiles are similar to those studied by Indares and Martignole (1990a) and Boggs (1996) in their transects across the CMB-Q and Bondy Gneiss Complex, respectively.

In growth zoning, Mn is zoned normally with lower values occurring near garnet rims relative to the rest of the garnet profile, consistent with depletion of the garnet-compatible element in the matrix during garnet growth (e.g. Pyle et al. 1999; Kohn and Spear 2000; Kohn and Malloy 2004). But the RAC3-1 and RAC3-2 garnets, as shown in the elemental maps, show a rimward Mn (and Fe) enrichment and an inversely related Mg depletion possibly suggesting retrograde metamorphism (e.g. Kohn and Spear 2000; Kohn and Malloy 2004). Overall, these trends are similar to those of Tuccillo et al. (1990) in their study of the upper amphibolite facies Britt Domain, Ontario Grenville province who described the resorption of garnet to form other ferromagnesian phases such as biotite. Tuccillo et al. (1990) also noted that because Mn is not

so easily incorporated into biotite, it will diffuse into the garnet, creating a near-rim enrichment in Mn, as observed in this study.

The major element Fe, Mg and Mn distribution maps show well defined features that do not correlate with the Ca, Y, and P maps. Various types of Ca and Y elemental map distributions are observed: asymmetrical zoning, rimward Ca increase and near-rim decrease of Y, patchy Ca with a general rimward Ca decrease and uniform Y distribution. The near-core Y concentration increases to ~ 850 ppm proximal to an apatite inclusion along a crack.

This study reveals the interaction between accessory and major phases throughout a metamorphic event and, more specifically, the partitioning of Y between these phases such as monazite and garnet (e.g. Foster et al. 2000; Pyle et al. 2001; Pyle and Spear 2003). Garnet can accommodate several thousand ppm Y, and the total volume of garnet in metapelites is two to three orders of magnitude greater than monazite and xenotime (Pyle and Spear 2000b). As such, production or consumption of monazite affects the availability of Y, and is reflected in garnet in preserved Y zones.

CHAPTER 7: MONAZITE EMPA GEOCHRONOLOGY

Previous studies investigate the behaviour of rare-earth elements (REEs) in accessory minerals during metamorphic processes (e.g. Bea 1996; Pyle and Spear 2002; Montel et al. 2000). In order to have a better understanding of these accessory REE minerals, especially monazite, this study investigates their occurrence, composition and textural relationship to rock-forming minerals (i.e. garnet). Since multiple ages and/or compositional domains can be preserved within individual monazite grains, monazite geochemistry and geochronology can thus shed light on the complex polyphase metamorphism of the CMB-Q within the study area (Suzuki and Adachi 1991; Montel et al. 1996; Cocherie et al. 1998; Dahl et al. 2005). Therefore an understanding of monazite growth and chemical composition from the Otter Lake area can be used to help interpret the tectonic environment in which they grew.

Chemical composition of monazite

Four monazite-bearing samples were identified: granodiorite (RAC22) from the amphibolite with diorite migmatite and three from the stromatic Grt-Bt-Sil gneiss, quartz-monzonite (12695), garnet quartz-monzonite (RAC3) and garnet monzonite (RAC13) (Fig. 24). Monazites from RAC22 and 12695 represent injected leucosomes whereas RAC3 and RAC13 are from garnet-bearing in situ melanosomes based on field, petrographic and geochemical data. From these four thin sections a total of twenty-two monazite crystals were analyzed. Monazites from both the injected and in situ spot analyses were divided based on their location within the following petrographic domains: leucosome, matrix and inclusions in garnet (in situ samples only).

All monazite EMP spot analyses (Tables 5 and 6) have cation totals between 2.00 and 2.03 atoms per formula unit (apfu) and were thus considered acceptable. From the 91 spot

analyses totals 9 are less than 98.00 wt%. Typically any analysis under 98.00 wt% is considered unacceptable. For purposes of this study, results were included to show the work that was carried out on these samples. Many studies of monazite do not measure the full suite of REEs in monazite (e.g. Roeder 1985; Parrish 1990; Scherrer 2001). The problem of accurate measurement of background and overlap correction for concentrations less than 0.1 wt% are very significant, and results at this level should be viewed with scepticism (Parrish 1990). The above-mentioned departure from stoichiometry is believed to be due to the presence of unanalyzed trace and REE elements.

The majority of the monazites analyzed are chemically comparable plotting within the monazite-(Ce) field (Fig. 26a) defined by Linthout (2007) (Tables 5 and 6). Although, the injected leucosomal monazite-(Ce) samples are more La-rich relative to the Nd-rich monazite-(Ce) from in situ melanosomes. Furthermore, the La/Nd vs. Ce_2O_3 diagram (Fig. 27c) illustrates the La-enriched nature of the injected monazites relative to the Nd-enriched in situ monazites. The increase in $(La/Yb)_N$ ratios (Fig. 27c) correlates positively with younging ages. One such example is from monazite included in garnet along matrix-connecting cracks (A18, up to 908) (Tables 5 and 6 and Figs. 30-31). The rimward increase could suggest monazite fractionation, possibly due to hydrothermal leaching and melt present in the rock (e.g. Poitrasson et al. 1996).

Chemical zoning in monazites result from (partial) dissolution of the monazite lattice, which may (or may not) be enhanced by the presence of hydrothermal fluids (Ayers et al. 1999; Williams et al. 2007). Fluid mobilization of REEs has been described in detail by Pan and Fleet (1996). These fluids cause the breakdown of the structure and enhance the formation of other related phases like apatite and allanite (Ayers et al. 1999). At lower-amphibolite facies conditions, the formation of metamorphic monazite often involves the breakdown of allanite

(Krenn and Finger 2007). However, metamorphic monazite also forms through the direct recrystallization of older monazite (McFarlane et al. 2005). This latter process is more common at higher metamorphic grades of upper-amphibolite and granulite facies (McFarlane et al. 2005), as recorded in the studied Otter Lake area.

The analysed geochemical features yield characteristic chemical zonation identified by relative proportions of varying Y_2O_3, ThO_2, LREE and HREE. The inversely correlated Y_2O_3 vs. ThO_2 illustrate in situ monazites are more Y_2O_3-enriched relative to the ThO_2-enriched injected samples (Fig. 27a). The Y_2O_3 vs. HREE variation diagram shows a positive linear correlation with Y_2O_3 and HREE (Fig. 27b).

Furthermore, the LREE concentrations are approximately constant for the in situ monazites relative to varying LREE concentrations for injected monazites (Fig. 27d). The monazites within the injected quartz-monazite leucosome have LREE/HREE ratios that are relatively larger than the injected granodiorite leucosome ratios. In situ monazites included within garnet from the stromatic Grt-Bt-Sil gneiss are comparatively HREE- and Y-poor in contrast to the leucosome and matrix HREE- and Y-rich monazite from the same in situ melanosome samples (Fig. 27d). This could possibly reflect that included monazites within garnet (HREE- and Y-poor) may have grown concurrent with or following substantial garnet growth as demonstrated by Kohn et al. (2005). Chondrite-normalized REE distribution diagrams for monazite, normalized after Taylor & McClennan (1985), overall are similar with relative enrichment of the L-MREE and depletion of HREE and moderately negative Eu anomalies (Fig. 31).

Monazite U-Th-Pb EMPA chemical ages

Monazite can grow at different stages of metamorphism and melting, it can preserve different ages within individual crystals and it also has the potential to survive multiple metamorphic, magmatic and/or hydrothermal events (Spear and Pyle 2002). The advantage of the EMP method for analyzing the U-Th-Pb chemical ages is because it is a in situ, non-destructive method able to analyze the chemical composition of domains only several microns in size, thus preserving the textural setting (Cocherie et al. 2005).

The chemical zones for the analyzed monazites were identified with the aid of the backscatter electron detector (BSE). These chemical domains include patchy zoning (A1, A4, A7-A10, A13-A14, and A20), smaller crystals with no zoning (A11, A15-A18, A21), few with concentric zoning (A2-A3 and A5), and to a lesser extent intergrowth-like zoning (A2 and A6). From the in situ samples monazite samples occurring as inclusions in garnet (Fig. 30) are relatively smaller and generally more compositionally homogeneous than larger leucosome and matrix monazites (Fig. 28 – 30), though exceptions do exist (A10, A14 and A20).

Measurements for U, Th, Pb and Y were collected in order to calculate an age for each analyzed spot. The analyzed sample chemical age data are from 91 analyses and represent 22 individual monazite crystals summarized in Tables 7 – 10. Individual spot analyses are listed into three texturally distinct subsets: (1) monazite included in leucosome; (2) monazite included in matrix and (3) monazite included in garnet. Furthermore, chemical U-Th-Pb monazite age results using the EMPA (Tables 7 – 10) have been pooled in the following manner (1) point by point; (2) grain by grain and (3) thin section by thin section. Monazite ages were 'pooled' keeping the statistical mean standard weight deviation (MSWD < 5.5). Relatively few analyses were collected from each sample, therefore making it difficult to minimize analytical error by

pooling individual measurements from each age population, hence why this approach is the best, given the dataset.

Data from each grain are presented using cumulative probability curves of average ages obtained for monazites. Twenty-six EMPA U-Th-Pb data analyses on three monazites (A1-A3) from the injected granodiorite leucosome (Table 7) and have between 7 and 10 analytical points on each grain (Fig 28a-c). A pooled 'mean' age for each grain was calculated. A total of 65 spot analyses were taken from 19 monazites within three thin sections from the stromatic Grt-Bt-Sil gneiss. 21 spot analyses on 8 monazites (A7 - A13a and b) from the garnet quartz-monzonite are observed in three texturally distinct domains: three monazite crystals within the leucosome (A11 - A13a; Fig. 28), four within the matrix (A7 – A9, A13b; Fig. 29) and one included within garnet (A10; Fig. 30) (Table 9 and Fig. 32c).

The 18 spot analyses on 8 monazites within garnet monzonite (A14 – A21; Fig. 28 and Fig. 30; Table 10 and Fig. 32d) occur mainly within garnet, except A21 (Fig. 33a) which occurs in the leucosome adjacent to zircon and K-feldspar and records the oldest 'inherited' spot analysis 1685 ± 14 Ma. The monazites included within garnet are relatively smaller 10 – 100 μm (average 40 μm) than matrix and leucosome monazites. Most of the monazites are lozenge- to oval-shaped with either no visible zoning or some relic concentric or patchy zones. The smaller grain-size of the included monazites decreases the number of chemical age analyses permitted on each grain (1 to 4 ages per grain). No ages fall between the ca. 1139 – 1170 Ma for monazites included in garnet from the garnet monzonite (RAC13).

Monazite A16, included within garnet, occurs along a matrix-connecting crack (1218 ± 16 Ma) and it is also adjacent to included zircon and apatite (Fig. 33c). There is a wide range of ages recorded within these garnet-included monazites ranging from 1570 ± 10 Ma to 1007 ± 8

Ma. Monazite A18, included in garnet, is located near a matrix-connecting crack exposing the monazite to the surrounding matrix and fluids which potentially reset the U-Th-Pb chronometer record to younger ages 1007± 8 Ma and 1097 ± 9 Ma. A similar observation occurs in A10 from RAC3 where evidence supporting this 'altered' monazite is inferred with the darker band concordant with the crack, where fluids could have passed through resetting the geochronometer (Fig. 33b-d). One limiting constraint to this study is the lack of an age for the darker, more corroded part of the monazite in A10 (1141 ± 21 Ma) which correlates with the matrix-connecting crack within the garnet where fluids possibly circulated.

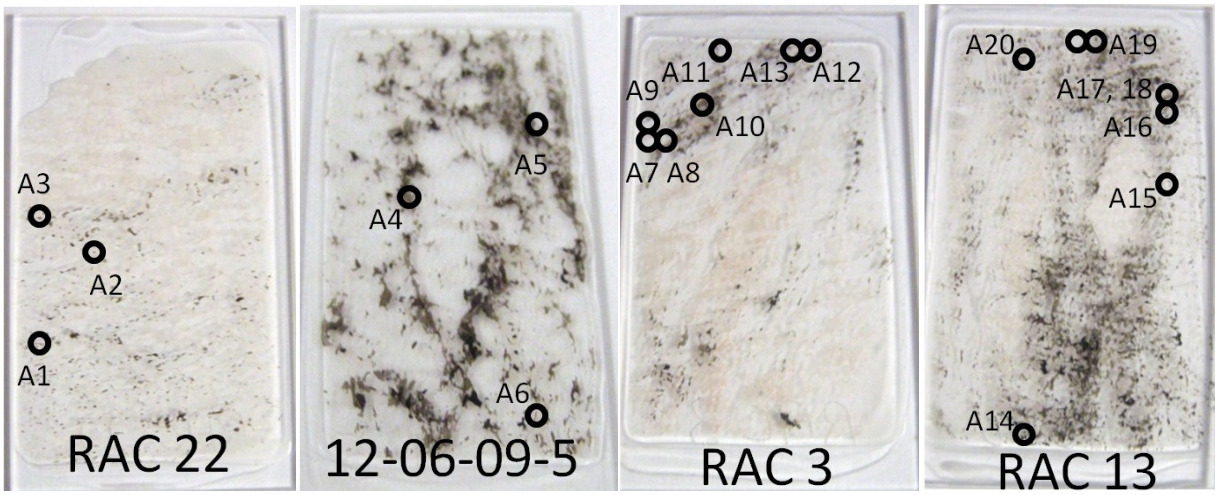

Figure 24: Polished thin section location of monazite used for EMPA chemical age analyses (A1-A21). A1-A6 are from injected granodiorite (RAC22) and quartz-monzonite (12695) whereas A7-A21 are from the in situ garnet quartz-monzonite (RAC3) and garnet monzonite (RAC13) samples.

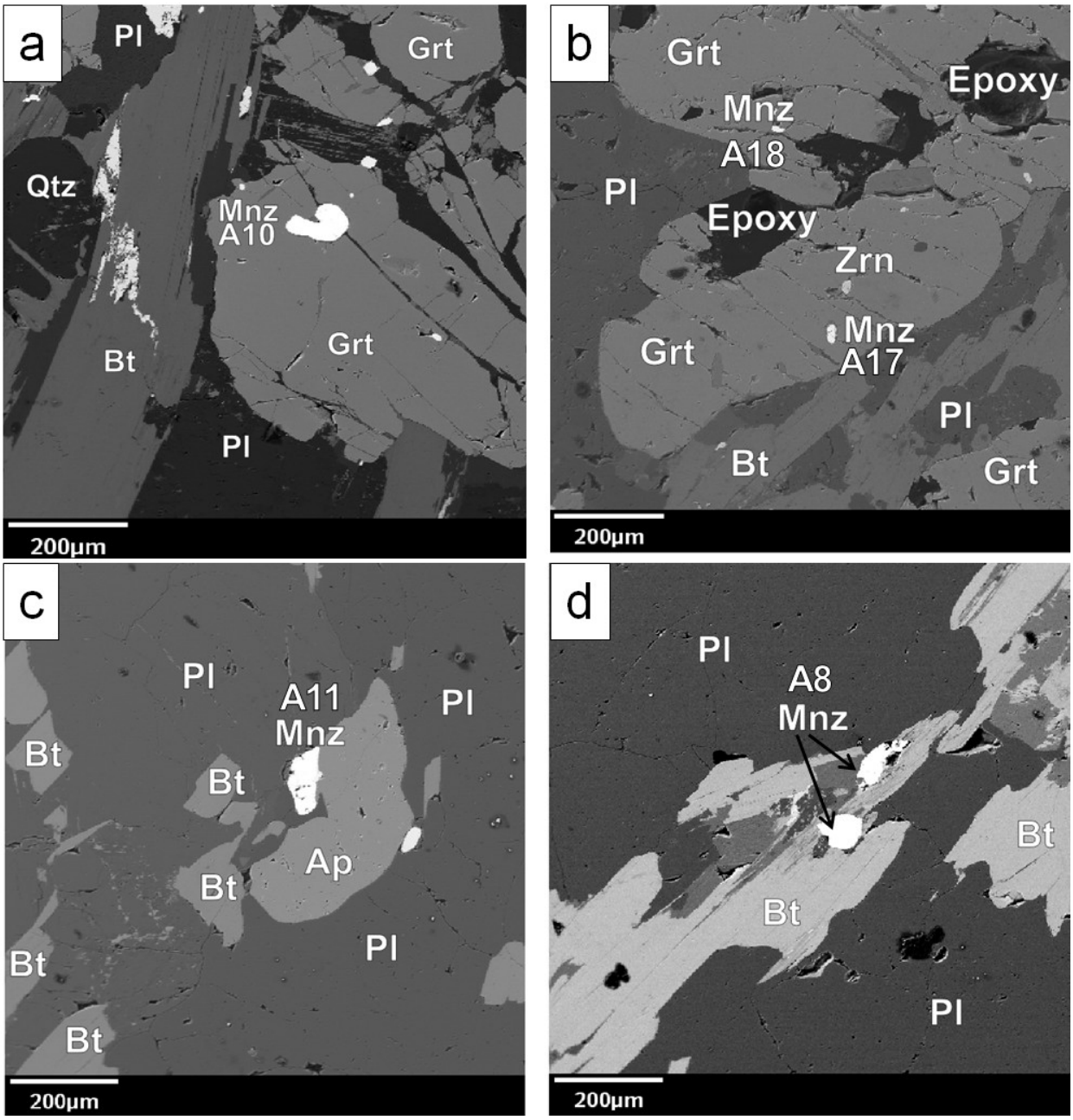

Figure 25: BSE images showing the texturally distinct domains in which monazite occurs: included in garnet, in leucosome and as inclusions in the matrix (mainly biotite): (a) monazite in garnet quartz-monzonite (RAC3) included in garnet. (b) Monazite grains in garnet monzonite (RAC13) sample, where A18 is partially included; occurring along a crack in the garnet and A17 is completely included in garnet. (c) Monazite from garnet quartz-monzonite (RAC3), parallel to biotite-defining foliation and in contact with plagioclase and apatite. (d) Monazite occurring in the matrix (biotite), parallel to foliation from garnet quartz-monzonite (RAC3). Mineral abbreviations are after Whitney and Evans (2010).

	Suite 1: Amphibolite with Diorite Migmatite													Suite 3: Stromatic Grt-Bt-Sil Gneiss						
	Injected Leucosome: Granodiorite (RAC22)													Injected Leucosome: Quartz-Monzonite (12695)						
	Leucosome Monazites													Matrix Monazites						
	A1					A2			A3					A4		A5		A6		
(wt%)	RAC22-1	RAC22-2	RAC22-3	RAC22-4	RAC22-5	RAC22-6	RAC22-7	RAC22-8	RAC22-9	RAC22-10	RAC22-11	RAC22-12	RAC22-13	12695-1	12695-2	12695-3	12695-4	12695-5	12695-6	12695-7
P2O5	29.64	29.58	28.21	29.10	29.09	28.89	28.46	29.43	29.20	28.14	28.43	29.44	28.13	28.76	29.58	27.74	29.48	25.53	27.93	28.71
CaO	1.40	1.51	0.78	1.10	1.18	0.72	1.19	1.36	1.09	0.86	0.75	0.95	1.26	0.59	1.14	1.02	0.96	1.12	1.05	1.10
SiO2	0.57	0.63	1.40	0.76	0.82	1.02	1.26	0.60	0.60	1.35	1.00	0.54	1.39	0.62	0.51	1.21	0.50	2.72	1.28	0.67
Ce2O3	26.72	26.29	28.58	28.05	27.57	29.29	27.22	27.33	28.73	27.86	29.38	29.02	27.15	30.56	28.27	27.66	28.26	25.10	27.17	27.96
La2O3	14.58	14.63	16.02	14.94	14.96	16.89	15.21	14.96	15.85	16.05	16.82	15.36	15.54	16.79	15.23	15.70	14.43	13.93	14.89	14.74
Nd2O3	9.22	9.73	9.20	11.44	11.94	10.58	10.30	10.54	11.10	10.47	10.31	12.03	9.64	12.87	11.95	9.64	11.70	10.01	11.02	11.32
Pr2O3	2.44	2.68	2.59	2.68	2.59	2.59	2.69	2.77	2.73	2.75	2.86	2.49	2.57	2.83	2.76	2.36	2.57	2.32	2.35	2.71
Sm2O3	1.42	1.46	1.16	1.07	0.91	1.42	1.43	1.28	1.66	1.69	1.35	1.49	1.37	1.40	1.50	1.10	1.59	1.15	1.24	1.50
Eu2O3	0.00	0.00	0.00	0.00	0.00	0.00	0.00	0.09	0.00	0.00	0.00	0.00	0.00	0.00	0.07	0.00	0.00	0.03	0.02	0.00
Gd2O3	0.91	0.92	0.83	0.67	0.64	0.94	1.00	0.80	0.68	1.10	0.93	0.80	0.97	0.60	0.82	0.59	0.95	0.57	0.58	0.80
Tb2O3	0.04	0.02	0.07	0.03	0.15	0.10	0.04	0.03	0.02	0.05	0.12	0.08	0.16	0.04	0.07	0.02	0.07	0.00	0.03	0.02
Dy2O3	0.52	0.55	0.37	0.28	0.39	0.43	0.42	0.40	0.54	0.55	0.48	0.34	0.38	0.27	0.42	0.34	0.52	0.14	0.26	0.31
Ho2O3	0.15	0.03	0.09	0.31	0.19	0.06	0.19	0.26	0.12	0.23	0.20	0.18	0.24	0.31	0.08	0.20	0.10	0.18	0.05	0.27
Er2O3	0.24	0.27	0.14	0.12	0.11	0.04	0.20	0.22	0.12	0.21	0.15	0.15	0.06	0.04	0.14	0.10	0.16	0.07	0.08	0.12
Tm2O3	0.00	0.00	0.25	0.10	0.19	0.05	0.00	0.15	0.32	0.41	0.36	0.26	0.07	0.28	0.12	0.26	0.26	0.18	0.11	0.12
Yb2O3	0.11	0.10	0.06	0.00	0.07	0.05	0.13	0.15	0.05	0.15	0.13	0.11	0.09	0.08	0.17	0.17	0.17	0.04	0.05	0.04
Lu2O3	0.06	0.03	0.00	0.01	0.00	0.00	0.04	0.00	0.02	0.09	0.00	0.09	0.09	0.00	0.09	0.00	0.10	0.21	0.00	0.00
ThO2	6.99	6.91	7.00	5.72	6.36	4.70	8.11	6.23	5.50	6.45	4.44	4.54	8.51	2.91	4.82	7.00	4.21	12.63	7.84	5.54
Y2O3	2.04	2.22	1.55	0.99	1.11	1.71	1.74	1.78	1.32	1.81	1.74	1.33	1.67	0.73	1.45	1.17	1.45	0.66	0.75	1.08
UO2	0.59	0.86	0.37	0.74	0.66	0.14	0.38	0.98	0.78	0.29	0.18	0.72	0.45	0.44	0.78		0.75	0.75	0.47	0.80
SrO	0.08	0.00	0.02	0.01	0.02	0.04	0.00	0.00	0.04	0.00	0.01	0.00	0.01	0.00	0.03	0.00	0.01	0.03	0.02	0.04
FeO	0.00	0.00	0.00	0.00	0.00	0.00	0.00	0.00	0.00	0.00	0.00	0.00	0.00	0.00	0.00	0.00	0.00	0.00	0.00	0.00
Total	97.71	98.44	98.69	98.10	98.94	99.66	100.03	99.36	100.47	100.52	99.65	99.94	99.74	100.13	100.01	96.95	98.24	97.36	97.21	97.85
apfu based on 4 oxygens																				
P	0.992	0.985	0.952	0.980	0.974	0.963	0.951	0.979	0.971	0.941	0.955	0.979	0.944	0.966	0.980	0.955	0.989	0.894	0.958	0.975
Ca	0.059	0.064	0.033	0.047	0.050	0.031	0.051	0.057	0.046	0.036	0.032	0.040	0.053	0.025	0.048	0.045	0.041	0.050	0.046	0.047
Si	0.023	0.025	0.056	0.030	0.033	0.040	0.050	0.024	0.024	0.053	0.040	0.021	0.055	0.024	0.020	0.049	0.020	0.113	0.052	0.027
Ce	0.387	0.379	0.417	0.408	0.399	0.422	0.393	0.393	0.413	0.403	0.427	0.417	0.394	0.444	0.405	0.412	0.410	0.380	0.403	0.411
La	0.212	0.212	0.236	0.219	0.218	0.245	0.221	0.217	0.230	0.234	0.246	0.222	0.227	0.246	0.220	0.236	0.211	0.213	0.222	0.218
Nd	0.130	0.137	0.131	0.163	0.169	0.149	0.145	0.148	0.156	0.148	0.146	0.169	0.136	0.182	0.167	0.140	0.166	0.148	0.159	0.162
Pr	0.035	0.038	0.038	0.039	0.037	0.037	0.039	0.040	0.039	0.040	0.041	0.036	0.037	0.041	0.039	0.035	0.037	0.035	0.035	0.040
Sm	0.019	0.020	0.016	0.015	0.012	0.019	0.019	0.017	0.022	0.023	0.018	0.020	0.019	0.019	0.020	0.015	0.022	0.016	0.017	0.021
Eu	0.000	0.000	0.000	0.000	0.000	0.000	0.000	0.001	0.000	0.000	0.000	0.000	0.000	0.000	0.001	0.000	0.000	0.000	0.000	0.000
Gd	0.012	0.012	0.011	0.009	0.008	0.012	0.013	0.010	0.009	0.014	0.012	0.010	0.013	0.008	0.011	0.008	0.013	0.008	0.008	0.011
Tb	0.001	0.000	0.001	0.000	0.002	0.001	0.001	0.000	0.000	0.001	0.002	0.001	0.002	0.001	0.001	0.000	0.001	0.000	0.000	0.000
Dy	0.007	0.007	0.005	0.004	0.005	0.005	0.005	0.005	0.007	0.007	0.006	0.004	0.005	0.003	0.005	0.004	0.007	0.002	0.003	0.004
Ho	0.002	0.000	0.001	0.004	0.002	0.001	0.002	0.003	0.002	0.003	0.003	0.002	0.003	0.004	0.001	0.003	0.001	0.002	0.001	0.003
Er	0.003	0.003	0.002	0.001	0.001	0.001	0.002	0.003	0.001	0.003	0.002	0.002	0.001	0.001	0.002	0.001	0.002	0.001	0.001	0.001
Tm	0.000	0.000	0.003	0.001	0.002	0.001	0.000	0.002	0.004	0.005	0.005	0.003	0.001	0.004	0.002	0.003	0.003	0.002	0.001	0.002
Yb	0.001	0.001	0.001	0.000	0.001	0.001	0.002	0.002	0.001	0.002	0.002	0.001	0.001	0.001	0.002	0.002	0.002	0.000	0.001	0.000
Lu	0.001	0.000	0.000	0.000	0.000	0.000	0.000	0.000	0.000	0.001	0.000	0.001	0.001	0.000	0.001	0.000	0.001	0.003	0.000	0.000
Th	0.063	0.062	0.064	0.052	0.057	0.042	0.073	0.056	0.049	0.058	0.040	0.041	0.077	0.026	0.043	0.065	0.038	0.119	0.072	0.051
Y	0.043	0.046	0.033	0.021	0.023	0.036	0.037	0.037	0.028	0.038	0.037	0.028	0.035	0.015	0.030	0.025	0.031	0.015	0.016	0.023
U	0.005	0.008	0.003	0.007	0.006	0.001	0.003	0.009	0.007	0.003	0.002	0.006	0.004	0.004	0.007	0.006	0.007	0.007	0.004	0.007
Sr	0.002	0.000	0.000	0.000	0.000	0.001	0.000	0.000	0.001	0.000	0.000	0.000	0.000	0.000	0.001	0.000	0.000	0.001	0.000	0.001
Fe	0.000	0.000	0.000	0.000	0.000	0.000	0.000	0.000	0.000	0.000	0.000	0.000	0.000	0.000	0.000	0.000	0.000	0.000	0.000	0.000
Total	1.996	2.000	2.002	2.000	2.002	2.007	2.008	2.004	2.008	2.013	2.014	2.005	2.010	2.013	2.006	2.005	2.000	2.008	2.001	2.004
$(La/Yb)_N$	90.12	95.39	179.39		143.19	208.78	81.34	69.34	195.94	72.72	88.32	97.98	119.78	146.56	59.48	60.90	56.33	266.69	184.10	282.16

Table 5: Quantitative electron microprobe spot analyses of major- and minor-elements on monazite from two garnet-absent samples. Results, represented by weight percent (wt %) and cations per 4.00 atoms of oxygen as atoms per formula unit (apfu). Yellow-leucosome; blue- matrix; and red- garnet. Chondrite normalized values after Taylor and McLennan (1985)

	Suite 3: Stromatic Grt-Bt-Sil Gneiss																			
	In Situ Melanosome: Garnet Quartz-monzonite (RAC3)													In Situ Melanosome: Garnet Monzonite (RAC13)						
	Matrix					Garnet	Leucosome						Leuco-some	Garnet						
	A7		A8	A9		A13	A10	A11	A13		A12			A21	A14	A15	A16	A17	A18	A19	A20
(wt%)	RAC-1	RAC3-2	RAC3-3	RAC3-4	RAC3-5	RAC3-9	RAC3-1	RAC3-6	RAC3-7	RAC3-8	RAC3-10	RAC3-11	RAC3-12	RAC13-8	RAC13-1	RAC13-2	RAC13-3	RAC13-4	RAC13-5	RAC13-6	RAC13-7
P2O5	30.05	29.87	30.26	30.46	30.13	29.79	29.03	30.05	30.04	29.78	29.83	29.59	29.75	29.53	29.35	29.53	29.20	29.08	29.36	28.88	29.18
CaO	1.17	1.13	1.22	1.01	1.05	1.00	0.88	1.15	1.03	1.10	0.95	1.07	1.21	0.85	0.98	0.69	0.74	1.03	0.74	0.90	G
SiO2	0.28	0.28	0.36	0.14	0.35	0.18	0.42	0.28	0.25	0.41	0.19	0.34	0.35	0.34	0.32	0.40	0.21	0.37	0.55	0.50	0.35
Ce2O3	24.50	25.73	24.19	25.13	25.27	24.85	26.47	25.35	24.65	25.16	25.63	26.86	25.55	26.73	25.29	25.32	25.15	25.91	27.08	26.13	27.04
La2O3	11.70	12.70	11.60	11.77	12.14	11.73	12.49	12.41	11.77	12.41	12.36	14.28	12.34	12.35	10.60	11.57	11.13	11.00	12.25	11.61	12.29
Nd2O3	13.31	12.80	13.22	13.73	12.98	13.42	13.74	13.26	13.55	13.49	14.08	12.18	13.43	13.95	14.04	13.35	14.90	13.66	13.61	14.12	14.84
Pr2O3	2.78	3.03	2.80	3.06	3.10	2.85	2.98	2.78	2.87	2.92	2.80	2.58	2.68	3.07	3.12	3.08	2.80	3.10	2.64	2.77	3.08
Sm2O3	2.54	2.58	2.80	3.07	2.73	2.86	2.99	2.68	2.95	2.81	2.89	2.13	2.59	2.76	3.25	2.73	3.40	3.59	2.76	3.04	2.98
Eu2O3	0.10	0.12	0.08	0.08	0.09	0.15	0.08	0.09	0.26	0.19	0.13	0.03	0.09	0.04	0.00	0.00	0.20	0.00	0.09	0.00	0.00
Gd2O3	2.35	2.06	2.46	2.46	2.12	2.42	1.84	2.42	2.39	2.49	2.18	1.76	2.43	2.08	2.61	2.31	2.79	2.20	1.83	1.98	1.92
Tb2O3	0.21	0.25	0.18	0.32	0.27	0.16	0.23	0.23	0.16	0.17	0.20	0.17	0.24	0.25	0.33	0.21	0.22	0.20	0.00	0.09	0.09
Dy2O3	1.09	0.90	1.05	1.05	0.88	1.06	0.55	1.02	1.13	0.96	1.13	0.74	0.85	0.74	0.66	0.91	0.92	0.80	0.49	0.37	0.36
Ho2O3	0.30	0.26	0.13	0.02	0.08	0.17	0.16	0.15	0.32	0.19	0.03	0.04	0.05	0.15	0.27	0.23	0.18	0.15	0.33	0.10	0.24
Er2O3	0.28	0.17	0.19	0.23	0.13	0.23	0.08	0.16	0.24	0.10	0.21	0.24	0.15	0.13	0.10	0.34	0.09	0.10	0.11	0.06	0.02
Tm2O3	0.47	0.26	0.39	0.14	0.31	0.30	0.27	0.00	0.20	0.52	0.05	0.15	0.22	0.41	0.36	0.20	0.43	0.08	0.21	0.16	0.28
Yb2O3	0.00	0.13	0.00	0.03	0.00	0.07	0.03	0.06	0.17	0.10	0.16	0.08	0.04	0.09	0.00	0.13	0.05	0.03	0.01	0.00	0.06
Lu2O3	0.04	0.04	0.09	0.17	0.06	0.00	0.00	0.00	0.03	0.03	0.16	0.16	0.07	0.14	0.06	0.00	0.00	0.07	0.00	0.09	0.08
ThO2	4.50	5.05	5.02	4.12	4.35	3.86	3.06	4.17	3.55	4.13	3.28	4.68	4.61	2.90	4.09	3.01	2.30	4.35	3.79	4.34	3.05
Y2O3	3.39	2.37	3.12	3.23	2.62	3.59	1.01	2.83	3.62	2.25	3.01	2.55	2.26	1.57	1.71	3.48	2.06	1.49	1.43	0.94	0.88
UO2	0.86	0.30	0.84	0.63	0.89	0.77	0.97	0.86	0.81	1.14	0.59	0.27	0.96	0.58	0.34	0.21	0.68	0.50	0.62	0.30	0.17
SrO	0.00	0.06	0.03	0.01	0.03	0.00	0.06	0.01	0.00	0.03	0.03	0.00	0.00	0.00	0.05	0.00	0.00	0.00	0.02	0.00	0.01
FeO	0.00	0.00	0.00	0.00	0.00	0.00	0.01	0.00	0.00	0.00	0.00	0.00	0.00	0.00	0.98	1.87	0.00	0.64	0.81	1.30	0.09
Total	99.91	100.09	100.03	100.86	99.59	99.46	97.35	99.95	100.01	100.38	99.90	99.91	99.85	98.66	98.50	99.57	97.47	98.34	98.75	97.69	97.63
apfu based on 4 oxygens																					
P	0.990	0.988	0.993	0.995	0.994	0.989	0.988	0.990	0.989	0.984	0.988	0.982	0.986	0.990	0.986	0.976	0.992	0.982	0.982	0.979	0.991
Ca	0.049	0.047	0.050	0.042	0.044	0.042	0.038	0.048	0.043	0.046	0.040	0.045	0.051	0.036	0.041	0.029	0.032	0.044	0.031	0.038	0.027
Si	0.011	0.011	0.014	0.005	0.014	0.007	0.017	0.011	0.010	0.016	0.007	0.013	0.014	0.013	0.013	0.015	0.009	0.015	0.022	0.020	0.014
Ce	0.349	0.368	0.343	0.355	0.360	0.357	0.390	0.178	0.169	0.179	0.178	0.206	0.178	0.180	0.367	0.362	0.370	0.378	0.392	0.383	0.397
La	0.168	0.183	0.166	0.167	0.174	0.170	0.185	0.361	0.351	0.359	0.367	0.385	0.366	0.388	0.155	0.167	0.165	0.162	0.179	0.172	0.182
Nd	0.185	0.179	0.183	0.189	0.181	0.188	0.197	0.184	0.188	0.188	0.197	0.171	0.188	0.197	0.199	0.186	0.214	0.195	0.192	0.202	0.213
Pr	0.039	0.043	0.040	0.043	0.044	0.041	0.044	0.039	0.041	0.042	0.040	0.037	0.038	0.044	0.045	0.044	0.041	0.045	0.038	0.040	0.045
Sm	0.034	0.035	0.037	0.041	0.037	0.039	0.041	0.036	0.040	0.038	0.039	0.029	0.035	0.038	0.044	0.037	0.047	0.049	0.038	0.042	0.041
Eu	0.001	0.002	0.001	0.001	0.001	0.002	0.001	0.001	0.003	0.002	0.002	0.000	0.001	0.001	0.000	0.000	0.003	0.000	0.001	0.000	0.000
Gd	0.030	0.027	0.032	0.031	0.027	0.031	0.025	0.031	0.031	0.032	0.028	0.023	0.032	0.027	0.034	0.030	0.037	0.029	0.024	0.026	0.026
Tb	0.003	0.003	0.002	0.004	0.003	0.002	0.003	0.003	0.002	0.002	0.003	0.002	0.003	0.003	0.004	0.003	0.003	0.003	0.000	0.001	0.001
Dy	0.014	0.011	0.013	0.013	0.011	0.013	0.007	0.013	0.014	0.012	0.014	0.009	0.011	0.009	0.008	0.011	0.012	0.010	0.006	0.005	0.005
Ho	0.004	0.003	0.002	0.000	0.001	0.002	0.002	0.002	0.004	0.002	0.000	0.000	0.001	0.002	0.003	0.003	0.002	0.002	0.004	0.001	0.003
Er	0.003	0.002	0.002	0.003	0.002	0.003	0.001	0.002	0.003	0.001	0.003	0.003	0.002	0.002	0.001	0.004	0.001	0.001	0.001	0.001	0.000
Tm	0.006	0.003	0.005	0.002	0.004	0.004	0.003	0.000	0.002	0.006	0.001	0.002	0.003	0.005	0.004	0.002	0.005	0.001	0.003	0.002	0.003
Yb	0.000	0.001	0.000	0.000	0.000	0.001	0.000	0.001	0.002	0.001	0.002	0.001	0.001	0.001	0.000	0.002	0.001	0.000	0.000	0.000	0.001
Lu	0.000	0.000	0.001	0.002	0.001	0.000	0.000	0.000	0.000	0.000	0.002	0.002	0.001	0.002	0.001	0.000	0.000	0.001	0.000	0.001	0.001
Th	0.040	0.045	0.044	0.036	0.039	0.034	0.028	0.059	0.075	0.047	0.063	0.053	0.047	0.033	0.037	0.027	0.021	0.039	0.034	0.040	0.028
Y	0.070	0.049	0.064	0.066	0.054	0.075	0.022	0.037	0.031	0.037	0.029	0.042	0.041	0.026	0.036	0.072	0.044	0.032	0.030	0.020	0.019
U	0.007	0.003	0.007	0.005	0.008	0.007	0.009	0.007	0.007	0.010	0.005	0.002	0.008	0.005	0.003	0.002	0.006	0.004	0.005	0.003	0.001
Sr	0.000	0.001	0.001	0.000	0.001	0.000	0.001	0.000	0.000	0.000	0.000	0.000	0.000	0.000	0.001	0.000	0.000	0.000	0.001	0.000	0.000
Fe	0.000	0.000	0.000	0.000	0.000	0.000	0.000	0.000	0.000	0.001	0.001	0.000	0.000	0.000	0.032	0.061	0.000	0.021	0.027	0.044	0.003
Total	2.004	2.005	2.000	2.002	1.999	2.005	2.003	2.004	2.006	2.005	2.008	2.008	2.005	2.004	2.017	2.032	2.004	2.014	2.011	2.020	2.002
$La/Yb)_N$		68.52		258.73		120.03	296.46	150.30	46.25	81.82	52.40	119.33	197.96	88.30		58.68	150.15	261.19	908.46		145.86

Table 6: Quantitative electron microprobe spot analyses of major- and minor-elements on monazite from two garnet-rich samples. Results, represented by weight percent (wt %) and cations per 4.00 atoms of oxygen as atoms per formula unit (apfu). Yellow-leucosome, blue- matrix and red- garnet. Chondrite normalized values after Taylor and McLennan (1985)

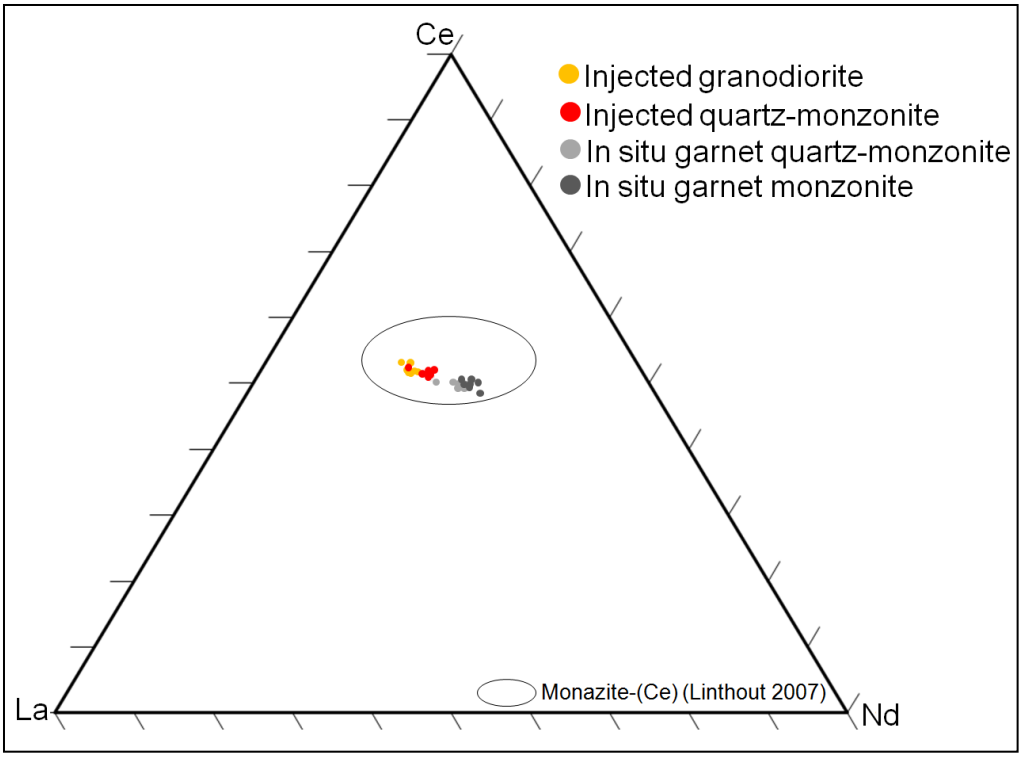

Figure 26: Ternary Ce-La-Nd plot for both the injected (RAC22 and 12695) and in situ (RAC3 and RAC13) of monazite spot analysis compositions relative to literature values for granitic monazite-(Ce) (circle outline). La, Ce, and Nd account for 75% of the total cation proportions for monazite. Note the restricted range of monazite composition, plus the nearly constant Ce values (Linthout 2007).

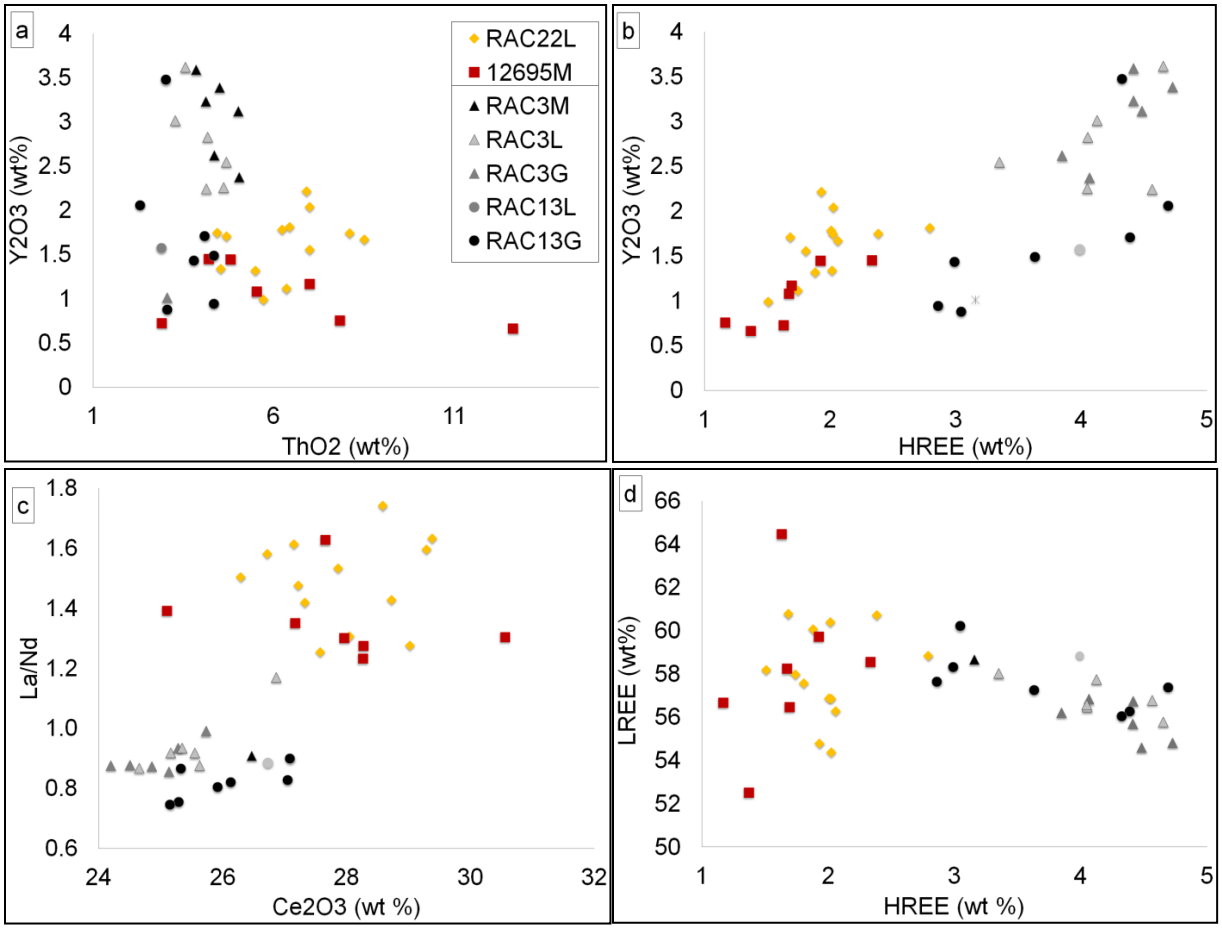

Figure 27: Variation diagrams for monazite from the injected leucosomes granodiorite (RAC22 and quartz-monzonite (12695) and in situ garnet quartz-monzonite (RAC3) and garnet monzonite (RAC13). Note their texturally distinct locations: leucosome (L), matrix (M) and as inclusions in garnet (G). (a) The inversely correlated Y_2O_3 vs. ThO_2 (wt %), where in situ monazites are more Y_2O_3 enriched relative to the ThO_2 enriched injected monazite. (b) Y_2O_3 vs. HREE shows a positive linear correlation from Y_2O_3 + HREE poor compositions in the injected and relatively enriched Y_2O_3 + HREE. (c) La/Nd vs. Ce_2O_3 for both. Note the La-enriched injected leucosome monazites relative to the Nd-enriched in situ melanosome monazites. (d) The weakly negative correlation between LREE vs. HREE for both types of monazites in this study. The injected monazites are relatively LREE-enriched relative to HREE and show a wide range whereas the monazites from the in situ samples are relatively LREE-depleted and HREE-enriched.

Summary of monazite chemistry and geochronology

Monazites in low grade samples (injected) generally contain more Th and LREE and less Y and HREE then the higher grade (in situ; i.e. presence of sillimanite) samples. The Nd_2O_3 and Sm_2O_3 contents for the in situ monazites (RAC3 and RAC13) are higher than the injected monazites. The Y + HREE and Nd_2O_3 enrichment in the in situ monazite analyses could be due to the breakdown of garnet, as suggested by the poikiolitic and embayed porphyroclasts described in Chapter 6, which subsequently released these elements into surrounding matrix at the time of monazite formation. Chemical changes to monazite during magmatism and/or metamorphism are important for interpreting different generations of monazite and their ages.

Based on field and petrographic textural observations, whole-rock geochemistry and monazite geochronology support the resulting 'pooled' ages from the individual injected monazites are 1045 ± 13 Ma (MSWD= 0.04; n= 3) for the granodiorite leucosome and 1052 ± 15 Ma (MSWD= 0.48; n= 2) for the quartz-monzonite leucosome (Fig. 34a) whereas the ages for the individual in situ melanosome monazites are 1060 ± 13 Ma (MSWD= 2.8; n= 3) for the garnet quartz-monzonite and 1064 ± 7 Ma (n= 1) for and the garnet monzonite (Fig. 34b). As a whole the in situ monazites record two main leucosome ages of 1063 ± 6 and 1136 ± 16 Ma (Fig. 34b) whereas the injected monazites record two main leucosome ages of 1048 ± 10 Ma (MSWD= 0.50; n= 2) and 1155 ± 14 Ma (MSWD= 4.5; n= 2).

As mentioned earlier, the growth of monazite occurs due to the breakdown of phosphate minerals or garnet which act as a source of REEs. Much of the compositional variations of monazite is presumed to be due to variations in Y and to a lesser extent Th. The preferred explanation for monazite Y variation is multiple stages of monazite growth in different whole-rock reactions (xenotime absent/present; garnet grown/consumed; low T/high T).

INJECTED		Measured Elements			Point by Point			Grain by grain				Thin Section by Thin Section			
Granodiorite (n=26)		Th (ppm)	U (ppm)	Pb (ppm)	Age (Ma)	Error	n	Age (Ma)	Error	MSWD	n	Age (Ma)	Error	MSWD	n
A1 L	RAC22-4.1	48498	7380	3375	1008	34	7	**1044**	**15**	**1.9**	**7**	**1045**	**13**	**0.04**	**3**
A1 L	RAC22-2.1	59536	7431	3972	1028	37						1174	23		
A1L	RAC22-1.2	83176	7025	5016	1029	42						1287	42		
A1 L	RAC22-5.1	70693	8670	4828	1056	39									
A1 L	RAC22-1.1	83843	6835	5189	1062	43									
A1 L	RAC22-3.1	69328	4369	4116	1072	41									
A1 L	RAC22-1.3	90385	7595	5747	1083	46									
A2 L	RAC22-6.2	64729	10123	4475	993	37	9	**1049**	**32**	**4.8**	**9**				
A2 L	RAC22-6.1	46890	2532	2557	1012	33									
A2 L	RAC22-8.1	63448	10065	4553	1023	38									
A2 L	RAC22-6.4r	48176	2450	2641	1026	34									
A2 L	RAC22-17.2	72008	4225	4121	1047	40									
A2 L	RAC22-6.3	57073	8663	4283	1083	39									
A2 L	RAC22-6.1r	46462	2248	2677	1084	36									
A2 L	RAC22-7.1	73226	3996	4307	1087	41									
A2 L	RAC22-8.2	59742	9757	4746	1115	41									
A3 L	RAC22-12.2	46900	2350	2710	1008	34	10	**1047**	**44**	**5.5**	**6**				
A3 L	RAC22-9.1	53510	7140	3600	1018	35									
A3 L	RAC22-12.1	45430	8290	3380	1018	38									
A3 L	RAC22-12.3	50760	8330	4050	1026	35									
A3 L	RAC22-9.2	54970	5970	3830	1045	36									
A3 L	RAC22-11.3	53150	7150	3690	1083	36									
A3 L	RAC22-10	48180	2450	2640	1168	43		1174	23	0.06	3				
A3 L	RAC22-11.2	66080	3670	4200	1174	39									
A3 L	RAC22-11.4	45890	2530	2930	1178	39									
A3 L	RAC22-11.1	44400	2430	3120	1287	42		1287	42		1				

Table 7: Table of chemical age data from the analyzed injected granodiorite (RAC22) sample, Suite 1. The individual spot analyses are represented by texturally distinct domains. In this case they all represent monazites included in leucosome (L) minerals (yellow). The resulting monazite ages have been pooled in the following manner: (1) point by point; (2) grain by grain and (3) thin section by thin section. Monazite ages were 'pooled' keeping the statistical mean standard weight deviation (MSWD < 5.5) and standard error at 2-sigma. Grain by grain monazite ages have been grouped into three groups: < 1040 – 1065 Ma, 1040 – 1065 Ma and > 1040 – 1065 Ma (inherited).

INJECTED		Measured Elements			Point by Point			Grain by grain				Thin Section by Thin Section			
Qtz-Monzonite (n=16)		Th (ppm)	U (ppm)	Pb (ppm)	Age (Ma)	Error	n	Age (Ma)	Error	MSWD	n	Age (Ma)	Error	MSWD	n
A4 M	12-6-9-5-2.1	50534	8658	3732	1024	35	5	**1048**	**18**	**2.2**	**4**	**1052**	**15**	**0.48**	**2**
A4 M	12-6-9-5-1.2	32869	6628	2610	1034	32						1089	25	0.77	
A4 M	12-6-9-5-2.3	53153	8454	3986	1066	38						1143	18	2.4	3
A4 M	12-6-9-5-2.2	53280	8641	4095	1084	42						1247	55		
A4 M	12-6-9-5-1.1	24484	5018	2203	1155	32		1155	32		1				
A5 M	12695-4.2	48423	6898	3527	1074	40	5	1089	25	0.77	3				
A5 M	12-6-9-5-4.1	45759	6926	3442	1087	41									
A5 M	12695-3.2r	45109	4390	3058	1114	49									
A5 M	12-6-9-5-3.1	73428	6259	5153	1186	54		1186	54		1				
A5 M	12-6-9-5-3.2	43982	4190	3343	1247	55		1247	55		1				
A6 M	12-6-9-5-6.1	76955	6389	4589	1021	47	6	**1059**	**26**	**2.4**	**3**				
A6 M	12-6-9-5-7.1	53185	7782	3867	1064	39									
A6 M	12-6-9-5-5.1	110259	7287	6782	1099	54									
A6 M	12-6-9-5-7.3	49662	7739	3907	1123	41		1127	24	0.15	3				
A6 M	12-6-9-5-7.2r	53592	7672	4097	1123	42									
A6 M	12-6-9-5-7.2	53276	7538	4110	1137	42									

Table 8: Table of chemical age data from the analyzed injected quartz-monzonite (12695), Suite 3. The individual spot analyses are represented by texturally distinct domains. All monazite spot analysis represent monazites included in matrix (M) minerals (blue) and number of analyses (n) is shown as well. The resulting monazite ages have been pooled in the following manner: (1) point by point; (2) grain by grain and (3) thin section by thin section. Monazite ages were 'pooled' keeping the statistical mean standard weight deviation (MSWD < 5.5) and standard error at 2-sigma.

IN SITU		Measured Elements			Point by Point			Grain by grain				Thin Section by Thin Section			
Grt Qtz-Monzonite (n=31)		Th (ppm)	U (ppm)	Pb (ppm)	Age (Ma)	Error	n	Age (Ma)	Error	MSWD	n	Age (Ma)	Error	MSWD	n
A11 L	RAC3-6.1	39505	11570	3365	942	30	3	948	21	0.36	2	970	28	2.9	6
A11 L	RAC3-6.3	31985	12337	3200	955	30						**1060**	**13**	**2.8**	3
A11 L	RAC3-6.2	43333	10269	3612	1014	34		1014	34		1	1136	16	0.21	4
A12 L	RAC3-12.2	51271	6903	3247	957	37	6	957	37		2	1274	31	0.57	2
A12 L	RAC3-11.1	51326	3297	2995	1051	54		**1066**	**21**	**0.47**	**4**	1322	36		
A12 L	RAC3-10.2	49270	4266	3072	1056	48									
A12 L	RAC3-10.1	37494	7746	3096	1062	37									
A12 L	RAC3-12.1	44833	10247	3946	1083	36									
A12 L	RAC3-11.2	43711	3849	2984	1147	53		1147	53		1				
A13a L	RAC3-7.1	51271	6903	3247	957	49	4	1011	56	3.7	4				
A13a L	RAC3-8.2	41553	10312	3485	1000	33									
A13a L	RAC3-8.1	41444	10578	3563	1011	34									
A13a L	RAC3-7.2	33211	8744	3028	1054	35									
A7 M	RAC3-1.1	42458	7739	3935	1240	48	4	1240	36	0.01	2				
A7 M	RAC3-2.1	48835	4743	3711	1241	55									
A7 M	RAC3-1.2	36460	7848	3867	1319	44		1322	36	0.07	2				
A7 M	RAC3-3.1	45585	3761	3583	1329	63									
A8 M	RAC3-3.4	44793	9214	3346	968	34	4	968	34		1				
A8 M	RAC3-3.1	47385	4744	3738	1125	40		1125	40		1				
A8 M	RAC3-3.2	49225	8565	4039	1218	52		1268	65	0.94	2				
A8 M	RAC3-3.3	55530	5388	4134	1276	56									
A9 M	RAC3-5.1	44537	10318	3554	982	33	5	982	33						
A9 M	RAC3-5.2	41307	11660	3904	1056	33		**1072**	**21**	**1.6**	**3**				
A9 M	RAC3-4.2	40693	7577	3236	1066	38									
A9 M	RAC3-4.3	32802	6315	2737	1102	39									
A9 M	RAC3-4.1	39632	7572	3414	1138	40		1138	40		1				
A13b M	RAC3-9.1	37476	7707	2981	1027	36	2	**1035**	**25**	**0.31**	**2**				
A13b M	RAC3-9.2	36319	9223	3215	1041	35									
A10 G	RAC3-20.2	31955	7967	3005	1111	37	3	1141	21	2.3	3				
A10 G	RAC3-20.1	32009	9371	3361	1145	36									
A10 G	RAC3-20.3	31937	10143	3566	1166	36									

Table 9: Table of chemical age data from the analyzed in situ garnet quartz-monzonite (RAC3), Suite 3. The individual spot analyses are separated into three texturally distinct domains: yellow- monazite included in leucosome (L); blue- monazite included in matrix (M); and red- as inclusions in garnet (G); where the number (n) of each pooled age is also given. The resulting monazite ages have been pooled in the following manner: (1) point by point; (2) grain by grain and (3) thin section by thin section. Monazite ages were 'pooled' keeping the statistical mean standard weight deviation (MSWD < 5.5) and standard error at 2-sigma.

IN SITU		Measured Elements			Point by Point			Grain by grain				Thin Section by Thin Section			
Grt Monzonite (n=18)		Th (ppm)	U (ppm)	Pb (ppm)	Age (Ma)	Error	n	Age (Ma)	Error	MSWD	n	Age (Ma)	Error	MSWD	n
A21 L	RAC13-8.2	29313	7284	2629	1064	9	4	**1064**	**7**	**0.02**	**2**	1007	8		
A21 L	RAC13-8.4	30998	7105	2684	1065	10						**1064**	**7**		
A21 L	RAC13-8.3	31562	6849	2768	1102	9		1102	9		1	1094	9		
A21 L	RAC13-8.1	29088	7047	2888	1685	14		1685	14		1				
A14 G	RAC13-1.3	34502	4472	3032	1318	11	3	1318	11		1	1218	16	1.02	
A14 G	RAC13-1.1	29579	3239	2670	1416	13		1426	16	0.97	2	1262	12		
A14 G	RAC13-1.2	22454	917	1692	1432	10						1318	11		
A15 G	RAC13-2.1	19976	861	1671	1570	10	1	1570	10		1	1344	11	2.2	
A16 G	RAC13-3.1	29364	7400	3044	1210	11	2	1218	16	1.02	2	1365	11		
A16 G	RAC13-3.2	19938	6916	2464	1226	11						1426	16	0.97	
A17 G	RAC13-4.1	35524	2150	2700	1365	11	1	1365	11		1	1517	11		
A18 G	RAC13-5.1	30196	6708	2428	1007	8	2	1007	8		1	1570	10		
A18 G	RAC13-5.2	31331	6680	2704	1094	9		1094	9		1	1685	14		
A19 G	RAC13-6.1	49455	3278	3516	1262	12	1	1262	12		1				
A20 G	RAC13-7.3	24771	1359	1801	1329	9	4	1344	11	2.2	3				
A20 G	RAC13-7.4	31543	2186	2429	1350	10									
A20 G	RAC13-7.1	27299	1253	1974	1357	10									
A20 G	RAC13-7.2	25371	1482	2144	1517	11		1517	11		1				

Table 10: Table of chemical age data from the analyzed in situ garnet monzonite (RAC13), Suite 3. The individual spot analyses are separated into two texturally distinct domains: yellow-monazite included in leucosome (L); blue- monazite included in matrix (M); and red- as inclusions in garnet (G); where the number (n) of each pooled age is also given. The resulting monazite ages have been pooled in the following manner: (1) point by point; (2) grain by grain and (3) thin section by thin section. Monazite ages were 'pooled' keeping the statistical mean standard weight deviation (MSWD < 5.5) and standard error at 2-sigma.

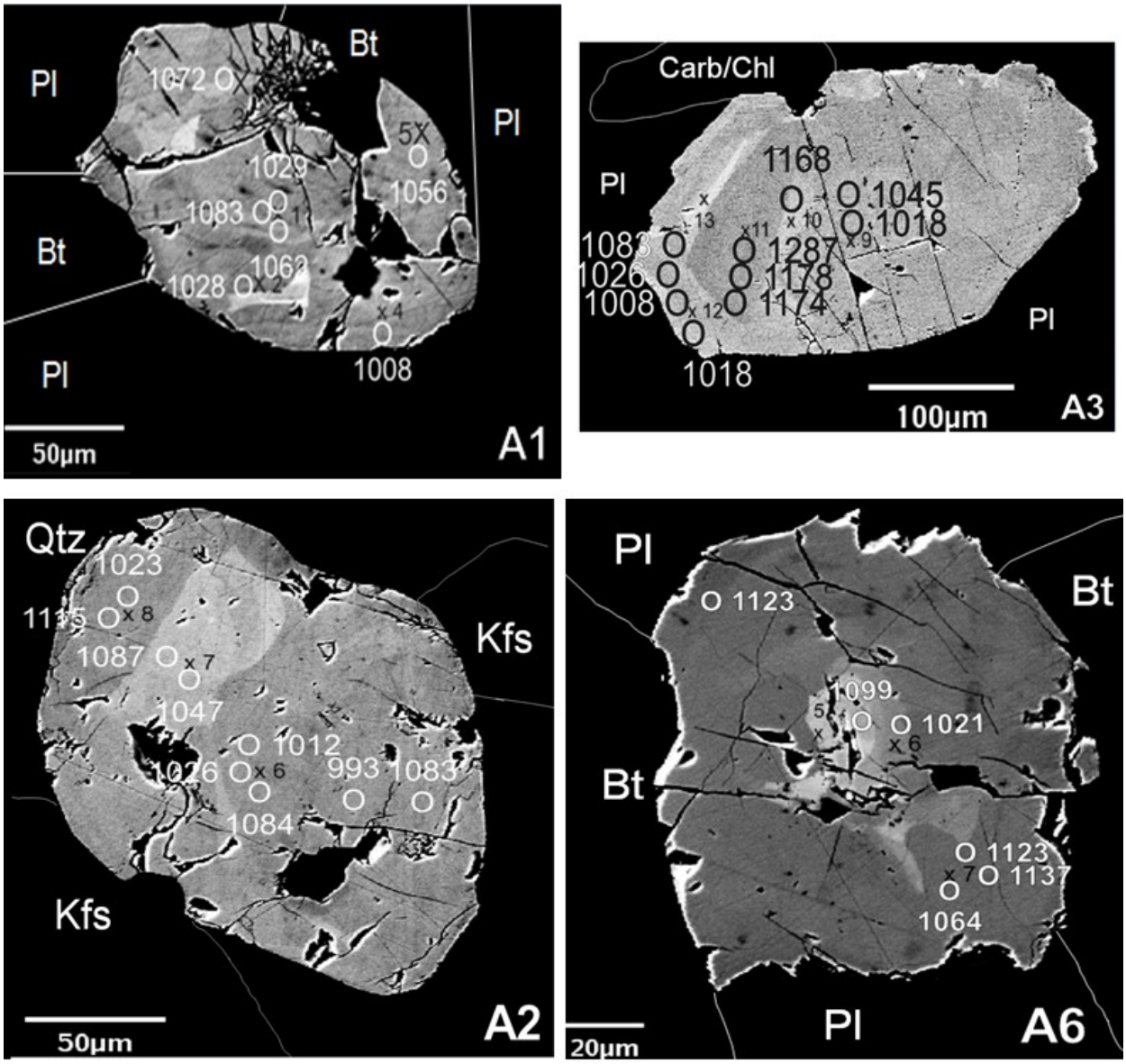

Figure 28: BSE images of monazite found within the leucosome with surrounding minerals. The numbers marked with an X are where chemical analyses were obtained on each grain, results displayed in Tables 5 and 6. The circles represent the calculated age (Ma) (Tables 7 – 10). The colour variations are representative of Th differences within each grain. Analyzed monazite crystal locations are as follows (A1-A3) within RAC22, (A11-A13) within RAC3, (A21) within RAC13, and (A6) within 12-06-09-5. Images for A11, A12, A13 and A21 are illustrated on next page. Surrounding mineral abbreviations are after Whitney and Evans (2010).

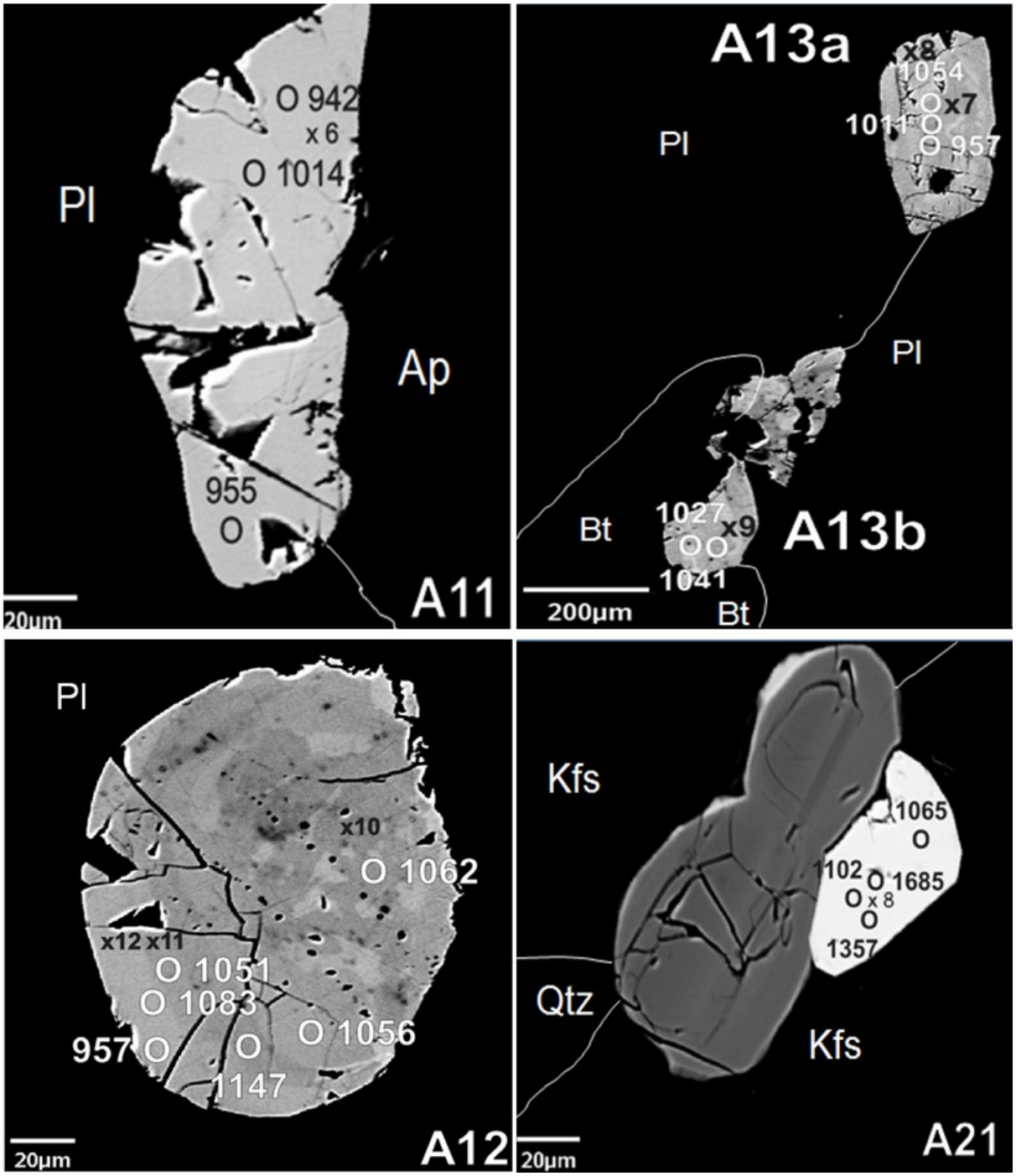

Figure 28 continued

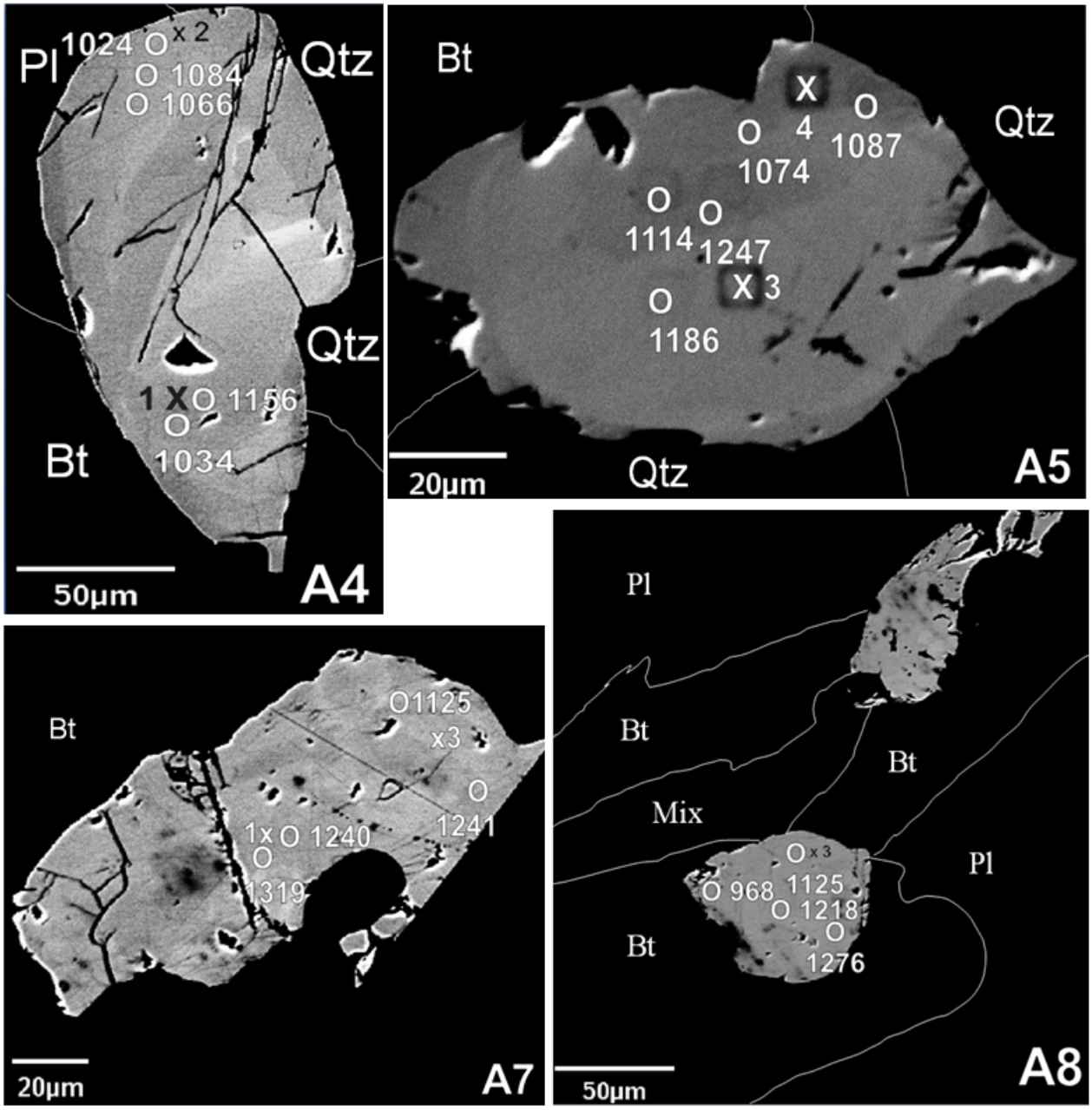

Figure 29: BSE images of monazite grains found within the melanosome with surrounding minerals. The numbers marked with an X (or in A5 squares) are where chemical analyses were obtained on each grain; results displayed in Tables 5 and 6. The circles represent the calculated age (Ma) (Tables 7 – 10). Analyzed monazites and their locations are as follows (A4-A5) are located within 12-06-09-5 and (A7-A9, A13) are located within RAC3. Monazite images for A9 and A13 are illustrated on the next page. Mineral abbreviations are after Whitney and Evans (2010).

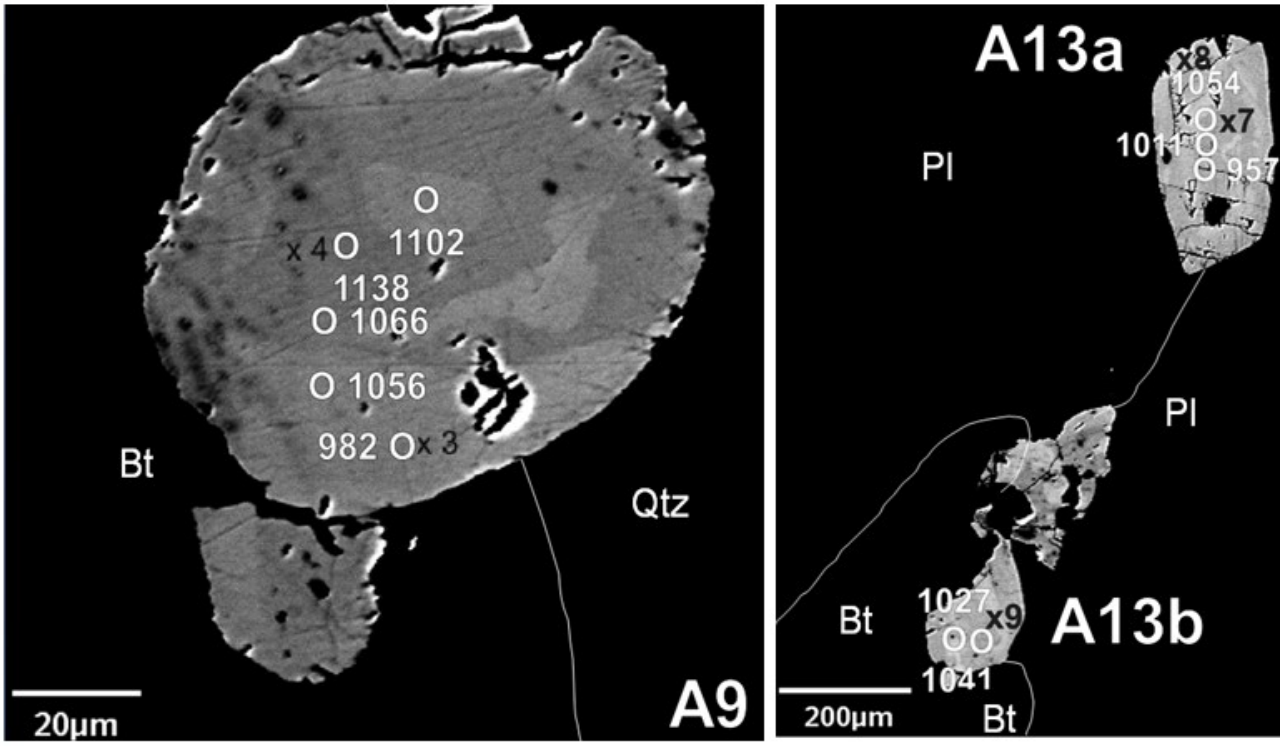

Figure 29 continued.

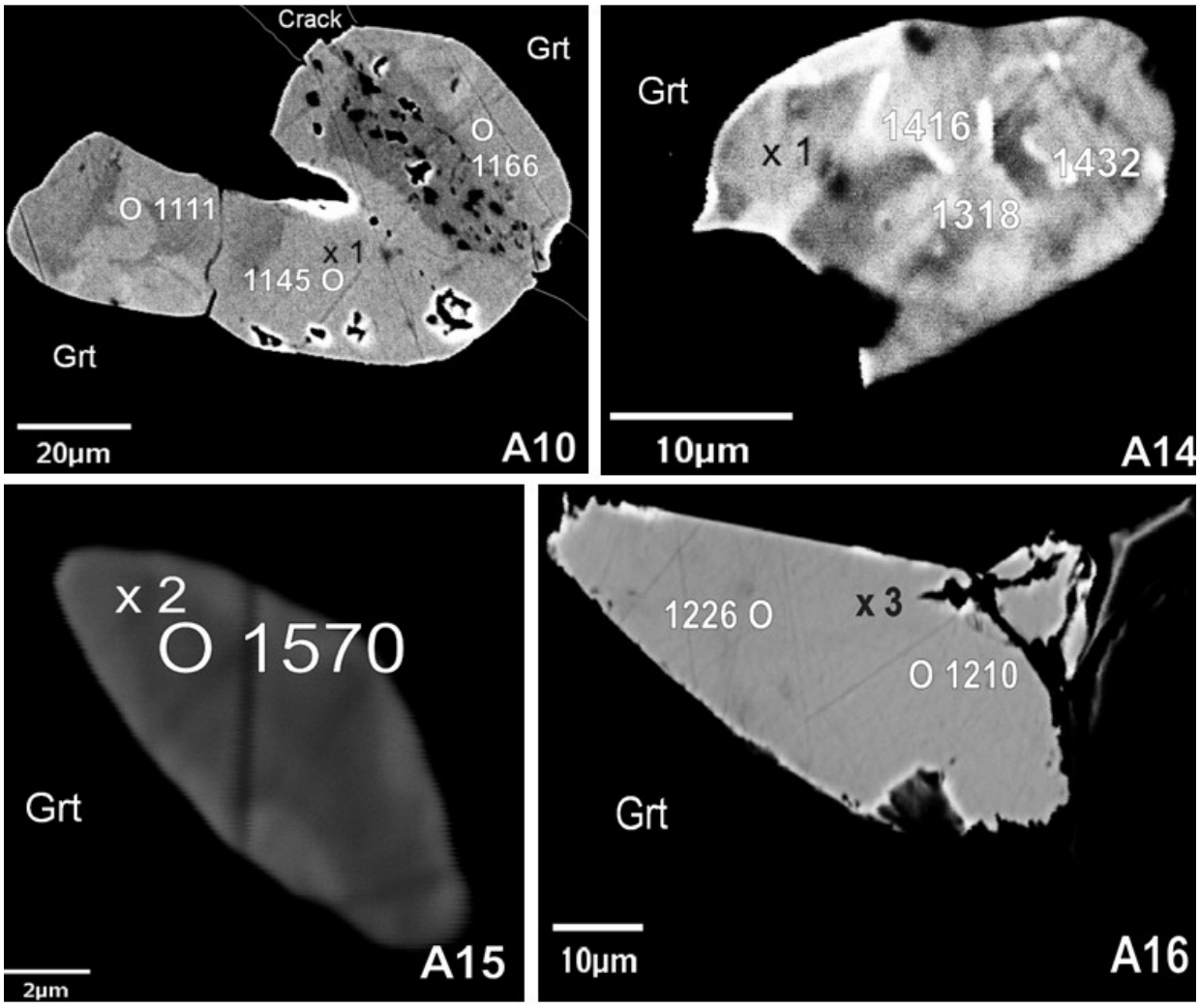

Figure 30: BSE images of monazite grains found as inclusions within garnet. The numbers marked with an X are where chemical analyses were obtained on each grain, results displayed in Tables 5 and 6. The circles represent the calculated age (Ma) (Tables 7 – 10). Analyzed monazite crystal locations (A10) is located within RAC3 and (A14 - A20) are located within RAC13. Monazite BSE images for A17 and A20 are illustrated on the next page. Surrounding mineral abbreviations are after Whitney and Evans (2010).

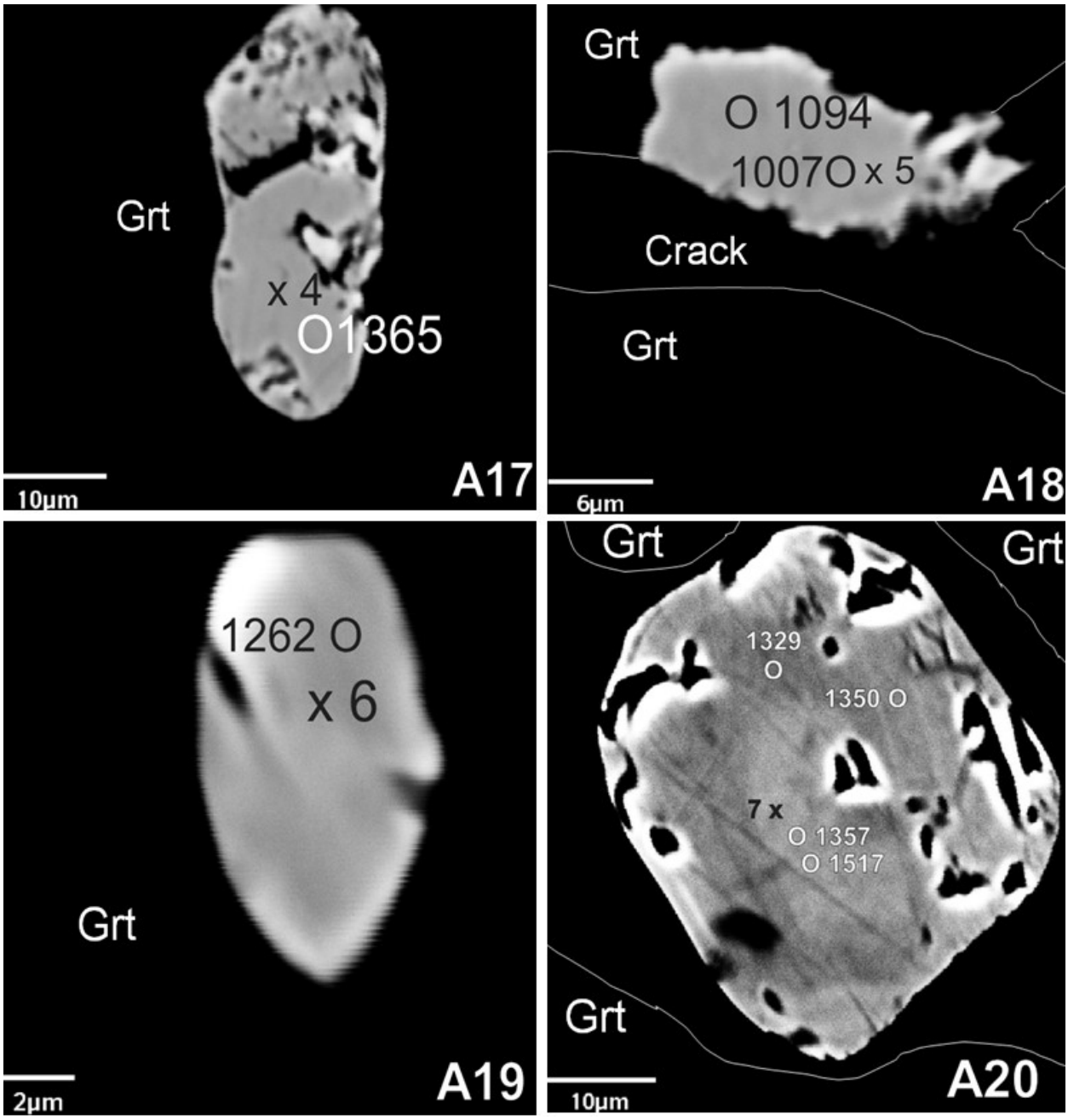

Figure 30 continued.

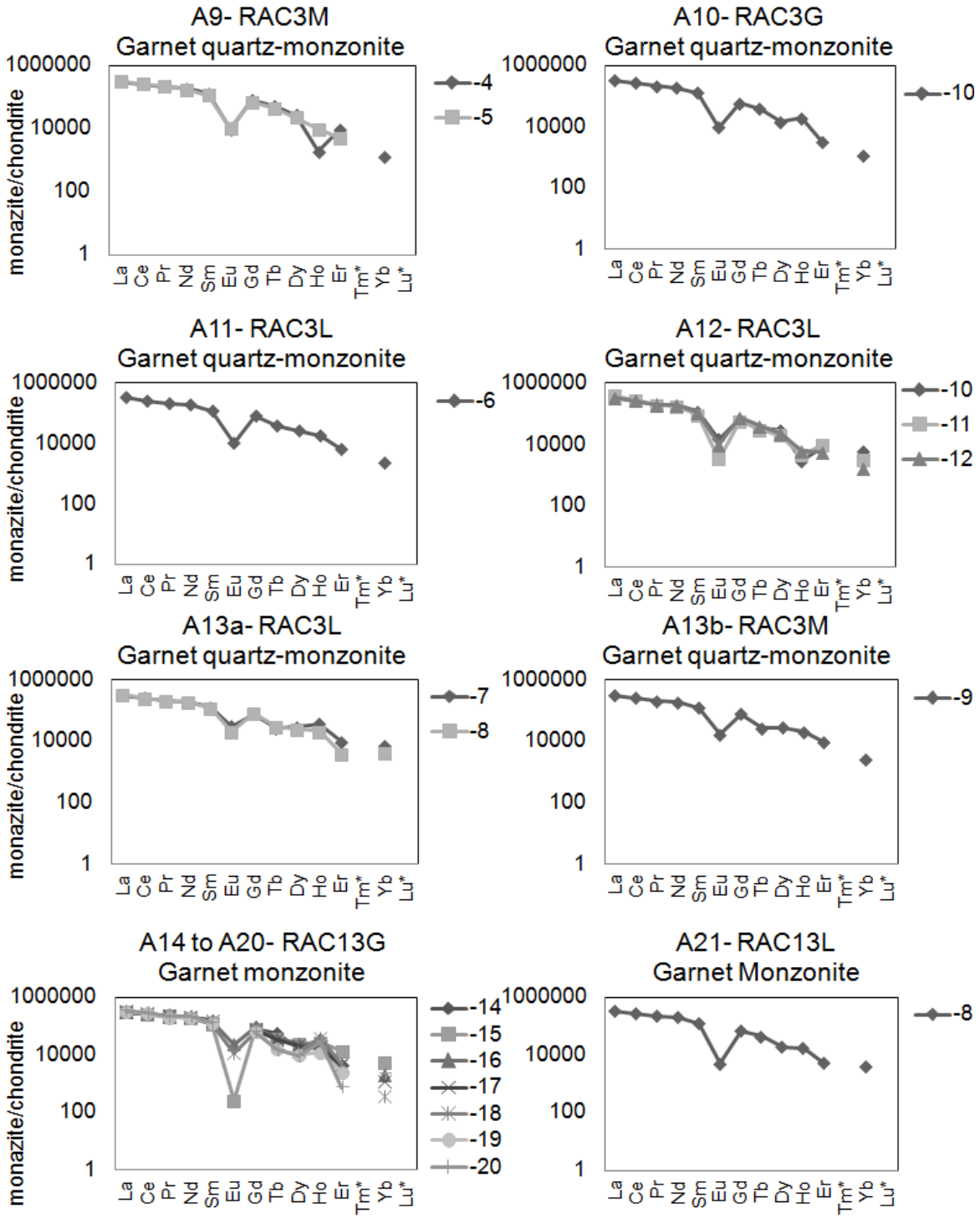

Figure 31: Chondrite-normalized distribution diagram for both the injected (RAC22 and 12695) and in situ (RAC3 and RAC13) monazites normalized after Taylor & McClennan (1985). The monazites occur in three domains (L: leucosome, M: matrix and G: inclusions in garnet; Tables 5 and 6) and exhibit relatively parallel patterns with relative enrichment of the L-MREE and depletion of HREE. Corrected values for Tm* and Lu* (Table A5) are not included because Tm is the least abundant of the stable REEs and the favoured x-ray line to use for Lu was unresolved (Scherrer 2001).

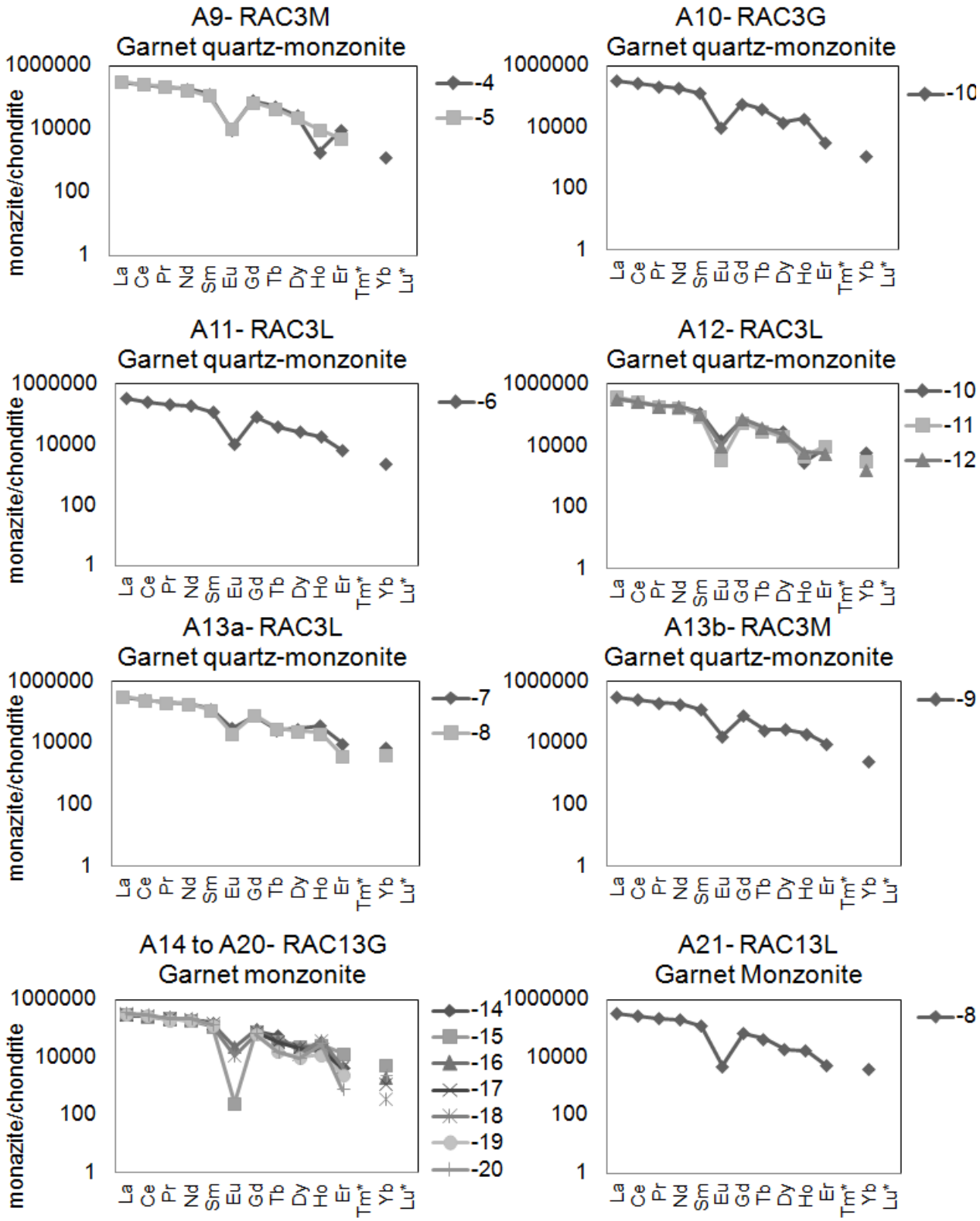

Figure 31 continued.

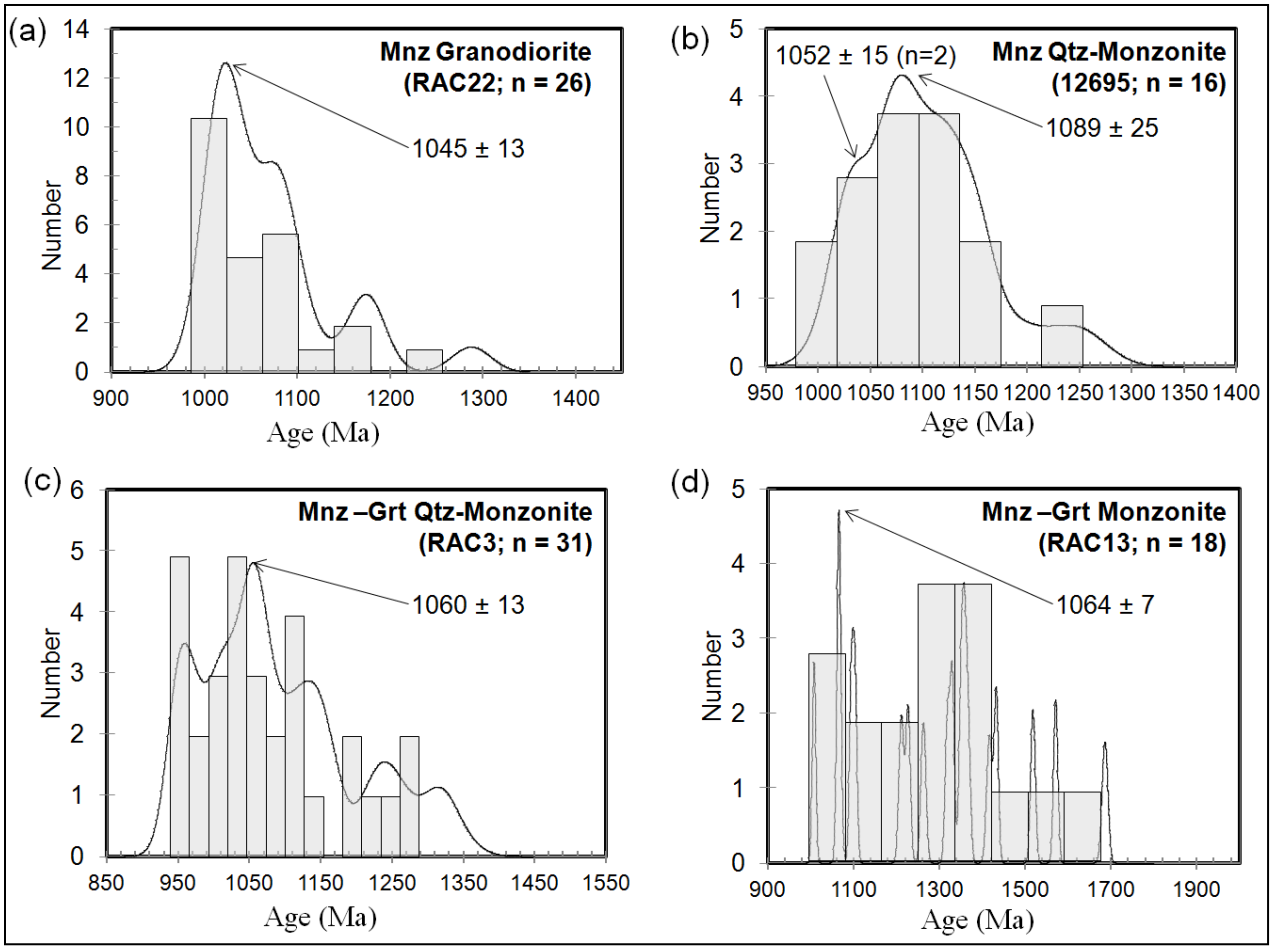

Figure 32: Probability density diagram and histograms for monazite ages from each monazite-bearing sample. The bold ages mark the monazite ages that fall between the 1040 to 1060 Ma range (a-b) injected monazites from RAC22 and 12695 (suites 1 and 3, respectively) and (c-d) in situ monazites from RAC3 and RAC13 (Suite 3). Probability density distributions calculated using *Isoplot* (Ludwig 2001) in excel, data from Tables 7 - 10.

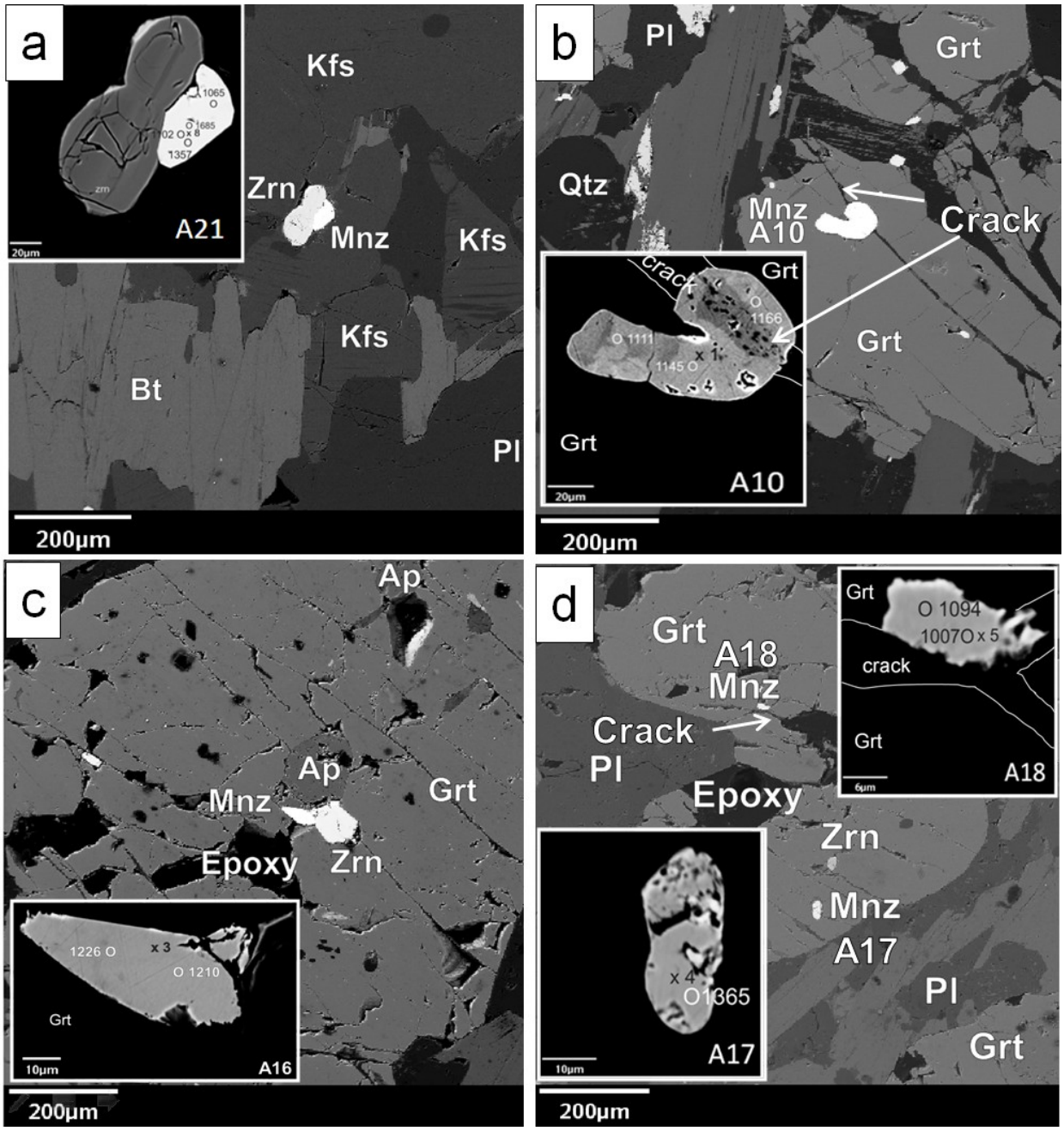

Figure 33: Electron backscatter images for various analyzed monazites. (a) A21 in leucosome from the in situ garnet monzonite (RAC13) adjacent to zircon and K-feldspar which records the oldest spot analysis 1685 ± 14 Ma. (b) A10 from the in situ garnet quartz-monzonite (RAC3) sample which shows evidence supporting this 'altered' monazite where possible fluids (white arrow) infiltrated along matrix-connecting cracks exposing the monazite to matrix-fluids potentially resetting the U-Th-Pb chronometer. (c) A16, included within garnet from the in situ garnet monzonite (RAC13), occurs along a matrix-connecting crack (1218 ± 16 Ma) also flanking to zircon and apatite, which are also included in the same garnet porphyroblast. (d) A18 is located near a crack in the garnet, where potential fluids could have passed through in turn resetting the geochronometer, whereas A17 in the same garnet is not near any cracks and preserves older ages. Mineral abbreviations are after Whitney and Evans (2010).

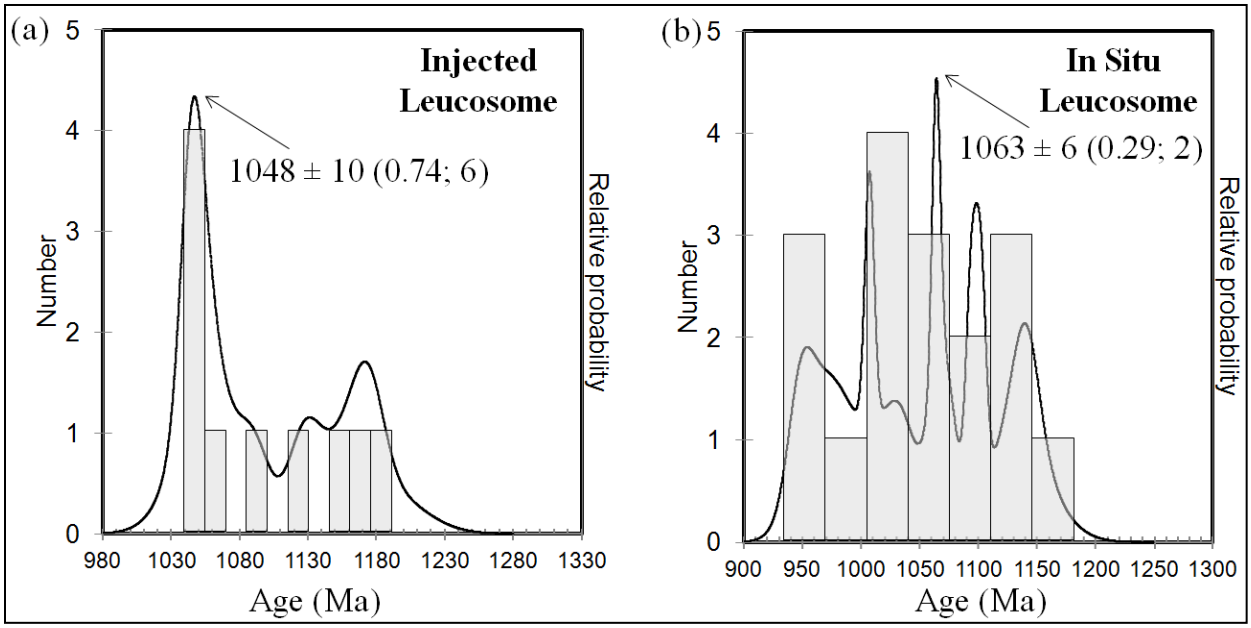

Figure 34: Histogram of monazite ages (Ma) determined from (a-b) garnet-absent monazites and (c-d) garnet-rich monazites. The peak ages for the ca. 1040- 1065 Ma, vales from Tables 7-10. Values in bracket are the mean standard weight deviation (MSWD) and number of analyses for pooled ages, respectively. Probability density distributions calculated using *Isoplot* (Ludwig 2003).

CHAPTER 8: DISCUSSION

Leucosome formation via partial melting of host rocks and/or magmatic injection: importance of element mobility during fluid-present anatexis in rocks at Otter Lake

At outcrop scale foliation in the amphibolite invariably becomes concordant with the sharp irregular contacts of the associated diorite migmatite and these bordering areas are either recrystallized or highly altered (Fig. 5c). In field and petrographic observations the injected granodiorite occupies the sub-vertical dilatant structure and has partial near-rim areas of highly altered and sericitized hornblende (Fig. 5a). Hornblende-rimmed pyroxenes could possibly be the result of cooling and melt crystallization and retrograde reactions between water-rich fluid and pyroxene (Timmermann et al. 2002; Stagslad et al. 2005). The anhydrous fluids that fluxed low temperature melting in these leucosomes were probably released by prograde metamorphic dehydration-type reactions occurring in adjacent rocks, which, because of their bulk compositions, had slightly higher solidus temperatures (e.g. Sawyer 2008; Nehring et al. 2009).

Petrographic evidence that might support low temperature melting fluxed by hydrous fluids is the presence of eye-shaped quartz porphyroblasts (augen) in the quartz-plagioclase felsic leucosome with fine-grained biotite defining the foliation (e.g. Sawyer 2002). The finer-grained amphibolite paleosome occurs as fragments (laths) in the coarser-grained leucosomes (Fig. 4a). This potentially indicates a further episode of dilatancy after some of the amphibolite had developed (e.g. Stagslad et al. 2005). In addition, the coarse-grained injected granodiorite could indicate that the magma and/or fluid pressure was high enough to cause fracturing of the amphibolite host rock as illustrated in Fig. 4 (e.g. Sawyer 2002; Stagslad et al. 2005).

Once produced, melts can either crystallize in situ or migrate over variable distances (injected) from their source regions (e.g. Bhadra et al. 2007). However the partial to complete

mobilization of layers with distinct leucosome forming diatexite migmatite (i.e. injected granodiorite) could possibly indicate that a considerable amount of melt was present at the time of late or post-peak metamorphic (anatectic) deformation where melt first formed as a thin film along grain boundaries (Fig. 6c; Sawyer 2002).

Nehring et al. (2009) modelled melting of amphibolite to generate magmas with an Archean tonalite-trondhjemite-granite (TTG) signature similar to the monazite-bearing leucosomes from this study (Fig. 17) requiring amphibole (and garnet) in the residue. Tiepolo and Tribuzio (2008) suggested that hornblende fractionation may lead to cumulates in the source giving rise to magmas with low HREE abundances and the concave-upward MREE to HREE pattern typical of TTGs. Although significant HREE depletion is most probably due to the removal of garnet, the concave-up REE pattern for both the in situ and injected leucosomes (Fig. 17) from the diorite migmatite suggest amphibole as another participating phase in the residue thus supporting the hypothesis of partial melting from the fractionated amphibole- (and garnet-) bearing amphibolite paleosome.

From melt formation to crystallization with Archean tonalite-trondhjemite-granite (TTG) signature, many processes can influence the melt and melt interaction with the surrounding rocks. Due to the various degrees of metamorphism previously recorded in the study area (e.g. Perkins et al. 1982; Kretz 1999, 2009; Schneider et al. 2013) the amphibolite and diorite migmatites and stromatic Grt-Bt-Sil gneisses samples may have undergone mobile elements changes. The observed geochemical changes of the S-type, peraluminous calc-alkaline and shoshonitic granitoids include alkalies (K_2O, Na_2O), CaO, and large ion lithophile elements (LILE: e.g. Rb, Sr, Ba, Th) and may not represent original pre-metamorphic concentrations (e.g. Bea et al. 1994; Bhadra 2007; Nehring et al. 2009). However, when used in conjunction with

major element discrimination, trace elements can be a powerful tool in determining the tectonic setting for the studied neosomes (e.g. Frost et al. 2001).

The enrichment of fluid-mobile Rb, Ba, K, and Pb and depletion of Nb, Ti, Y, and REE concentrations suggest metasomatism affected these samples (Fig. 14; e.g. Bea et al. 1994; Bhadra 2007; Nehring 2009). According to Stagslad et al. (2005), the resulting K-feldspar, plagioclase, quartz and accessory mineral (monazite and zircon) anatectic melts are enriched in K and Rb (and possibly other LILE) released from the alteration of amphibole and pyroxene (to sericite) and the associated enrichment of SiO_2, K_2O and Na_2O in the leucosomes is supporting evidence for the introduction of siliceous K-rich (alkaline) metasomatic fluids into these host rocks (e.g. Corriveau et al. 1998; Corriveau and van Breeman 2000; Corriveau and Gorton 2005).

Furthermore, the high Ba/La and elevated La/Yb ratios (Fig.18) for the injected granodiorite and quartz-monzonite are typical of magmas originating from convergent margins and are ascribed to the release of LILE- and LREE-enriched fluids or melts from the crustal slab (e.g. Morin et al. 2005) whereas the in situ neosomes are associated with mantle-derived arc magmas associated with fluid input (Fig. 16).

Grenvillian tectonism may enable hydrothermal fluids to be introduced marking the location of a magmatic-hydrothermal corridor (e.g. Corriveau et al. 1998; Corriveau and Gorton 1993; and Kretz 2009). Evidence that may support emplacement along a magmatic-hydrothermal shear zone (corridor) is provided by the presence of extensive and diverse peraluminous magmatic suites that have been previously documented in the Otter Lake area along the CDZ (e.g. Corriveau and Gorton 1993; Corriveau et al. 1998; Corriveau and Morin 2000; Corriveau and van Breeman 2000).

The variable peraluminous injected Chevreuil (1170 – 1160 Ma) and Kensington-Skootamatta (1090 – 1070 Ma) granitoid suites (Corriveau et al. 1990, 1996, 1998; Corriveau and Gorton 1993; Corriveau and Morin 2000; Morin et al. 2005) in the CMB-O and CMB-Q are derived from the partial-melting of the metasomatized-mantle during continent-continent collisional events prior to emplacement in the CMB-Q enriched in K, LILE and LREE (e.g. Corriveau et al. 1999; Morin et al. 2005).

Overall, the geochemical differences between the in situ and injected neosome could be linked to the difference in the composition of their sources and the probable contamination during transportation of the melting material (i.e. injection of magmatic liquid). As such, the source of the in situ leucosomes is most likely derived from partial melts of metasomatized mantle-derived arc rocks (i.e. metapelites). The injected leucosomes might originate from the influx of a mixed fluid during high-grade Grenvillian metamorphism (anatectic) melting of sediment-rich (i.e. garnet and amphibole) crustal rocks associated with later metasomatic alteration associated with the Chevreuil and Kensington-Skootamatta plutons in the Otter Lake area rocks as observed from the field, petrographic and geochemical data.

Fluid-mediated dissolution and reprecipitation of monazite relative to garnet growth and/or consumption within the Otter Lake area, CMB-Q

A proposed model is discussed for the behaviour of major, trace and rare-earth elements for monazite and garnet in an attempt to relate these changes to monazite growth, dissolution, and/or reprecipitation relative to garnet growth and/or consumption in the Otter Lake area, CMB-Q. Based on field, petrographic and geochemical results two compositionally distinct domains have been identified (1) Th- and LREE-rich injected domains and (2) Y- and HREE-rich in situ domains (Fig. 27). Complex compositional zoning of monazite in upper amphibolite-facies

rocks and in migmatites has been reported by many workers (e.g. Foster et al. 2000; Pyle et al. 2001; Spear and Pyle 2002; Kohn et al. 2005). Much of the compositional variations in metamorphic monazite is due to variations in Y distribution, and to a lesser extent Th. The most likely explanation for monazite Y variation is multiple stages of monazite growth in different whole-rock reaction settings (garnet growth/consumption, low T/ high T, xenotime absent/present, etc.).

Zoning in Y has been investigated because garnet and xenotime are the major sinks for Y and HREE in pelitic rocks. The partitioning of Y between the different minerals may permit conclusions regarding the timing of monazite growth relative to garnet growth (Pyle et al. 2001). Monazite from the in situ neosomes are typically enriched in Y+HREE concentrations possibly indicating growth prior to garnet formation or as a result of garnet breakdown (Pyle et al. 2001). If coexisting garnet were to breakdown Y+HREE would subsequently be released back into the bulk composition since major phases like plagioclase, biotite and quartz do not accommodate appreciable amounts of Y (Bea 1996; Yang 2002). Monazites that are enriched in Y+HREE (in situ neosomes) are most likely consistent with growth in a Y-rich environment and probably indicate high temperature formation (Pyle et al. 2001) due to xenotime or garnet breakdown (Pyle and Spear 1999). However, xenotime is absent from the studied samples and as such Y contents of monazite depend almost exclusively on reactions involving garnet (Pyle and Spear 1999; Foster et al. 2000; Kohn et al. 2005).

Monazites found as inclusions within garnet from the in situ neosomes are Y-poor relative to the leucosome and matrix monazites from the same samples. The youngest monazite (A16, Fig. 33c) grain, which is fully included in garnet, has two calculated ages of 1210 and 1226 Ma (Fig. 30d), and as such is inferred to have been shielded by garnet. Fully included

monazite has not been affected by partial or complete resetting of the U-Th-Pb geochronometer by subsequent metamorphic and/or hydrothermal events (Montel et al. 1996). This further supports that garnet acts as a shield inhibiting monazite against Pb loss or dissolution (e.g. Poitrasson et al. 1996). Therefore, shielded monazite could suggest crystallization occurred at or immediately prior to ca. 1218 Ma (pooled monazite age, Fig. 32d, Table 8) marking the upper boundary for initial garnet growth at or after ca. 1218 Ma (Fig. 35A).

Garnet generally grows during prograde metamorphism sequestering Y in its interior, which leads to later generations of monazite (and garnet) with lower Y contents (Kohn et al. 2005). Monazite grains in the injected leucosomes show Y- and HREE-poor and Th- and LREE-rich chemical compositions. The composition of these monazites suggests that they grew when garnet was present in the assemblage (e.g. Foster and Parrish 2003). This means that the Y- and HREE-rich in situ monazites, which grew before (i.e. monazite occurs as inclusions in the garnet) or at the expense of garnet breakdown, were dissolved prior to the formation of the Y- and HREE-poor injected monazites. This implies that garnet was most abundant (i.e. generally at the highest grade) during growth of the Y- and HREE-poor monazites from the injected neosomes (Kohn et al. 2005).

Supporting evidence for the abundance of garnet is the large (Grt1; Fig 35B), porphyroblastic anhedral garnet crystals. These garnets have undergone multiple periods of growth, the first being during prograde metamorphism and the onset of peak metamorphism during which time garnet growth was most abundant (e.g. Kohn et al. 2005). The Y- and HREE-poor and Th- and LREE-rich monazites from the injected neosomes could then have formed during melt recrystallization with the high Th-and LREE-contents being incorporated from an external source (i.e. Chevreuil-Kensington plutonic suites) or at the expense of phosphate

breakdown (i.e. allanite, apatite; Pyle et al . 2001; Pyle and Spear 2002; Kohn et al. 2005; Krenn et al. 2010). The recrystallization pooled age for these monazite grains in the injected leucosomes was calculated to be 1155 ± 14 Ma (Fig. 32d; Fig. 35B) most generally at the highest grade and when garnet growth was most abundant. This pooled ca. 1155 Ma monazite age for the injected leucosomes coincides with upper amphibolite to lower granulite peak regional metamorphism and magmatism during the Shawinigan Orogeny (1190 – 1140 Ma) recorded in the Otter Lake area (e.g. Schneider et al. 2013).

However, upon cooling, garnet growth ceases and/or dissolves while newly formed monazite continues to grow producing a post-melting generation of monazite because of melt crystallization during cooling (Kohn et al. 2005). These Y- and HREE-rich in situ monazite zones have been described by Dumond et al. (2010) to form during biotite-dehydration melting. The Y- and HREE-rich in situ monazites represent a new monazite generation which grew between 1139 ± 16 Ma (Fig. 32d; Fig. 37C) and 1063 ± 6 Ma (Fig. 32d; Fig. 35D) due to the breakdown of garnet. The onset of cooling and subsequent garnet breakdown at ca. 1139 Ma coincides with the end of the Shawinigan Orogeny (1190 – 1140 Ma) and the ca. 1063 Ma ages coincides with the end of the Kensington-Skootamatta magmatic suite (1090 – 1070 Ma).

Corriveau et al. (1998) interpreted the Kensington-Skootamatta K-rich alkaline magmatism as the initiation of the Ottawan Orogeny (1090 – 1020 Ma) in the CMB-Q. Inasmuch a second episode of garnet growth most likely occurred during peak Ottawan metamorphism recorded in the Y- and HREE-poor (injected) monazites at 1048 ± 10 Ma (Fig. 32d; Fig. 35E). These smaller (Grt2; Fig 35E), idioblastic garnet crystals are more almandine- + spessartine-rich relative to the larger pyrope-rich garnets. These smaller garnets exhibit reverse zoning with increasing Fe and Mn components from core to rim and decreasing Mg components

(Fig. 35E) while Ca remains constant which reflect the effects of retrograde metamorphism (Woodsworth 1977). Sharp rimward zoning in Mg, Fe and/or Mn is commonly attributed to diffusional exchange and/or network transfer reactions between garnet and biotite during cooling (e.g. Kohn et al. 2001). The Th- and LREE-rich monazites located within the injected leucosomes are interpreted to have grown during the crystallization of the partial melt where (K, LILE and REE)-rich metasomatic fluid alteration of monazite fluids infiltrating along the CDZ where partial or complete dissolution and resetting of monazite occurred during shear zone deformation and anatectic melt (peak Ottawan Metamorphism).

It should be emphasized that Grt1 and Grt2 represent different growth stages/periods, but I would like to emphasize there are two (geochemically distinct) types of garnets. The larger garnets (Grt1) are more pyrope-rich and almandine-depleted relative to the smaller almandine-rich garnets. A possible explanation for Grt2 showing more chemical zoning could possibly be due to its smaller size, and thus more susceptible to network cation reactions with matrix minerals, retrograde cooling reactions (Grt +Kfs + Liq → Bt + Sil + Pl + Qtz). This is supported by the near-rim zoning observed in the larger (Grt1) garnets.

Geological Implications and Summary

The studied amphibolite and associated diorite migmatite, K-feldspar gneiss and the stromatic Grt-Bt-Sil metapelitic gneiss from the Otter Lake area exhibit petrographical and chemical compositions characteristic of peraluminous, S-type (med-) high-K calc-alkaline amphibolite and associated diorite migmatite to shoshonitic granitoids for the K-feldspar and stromatic Grt-Bt-Sil gneiss. The K-feldspar gneiss represents a diatexite (injected neosome) migmatite, but due to the lack of monazite, geochemical emphasis is placed on the other samples. The absence of monazite where allanite and titanite are present could reflect the chemistry of the

host rock or it could indicate that monazite grew at the expense of allanite (and titanite) or vice versa (e.g. Bea 1996; Tomkins and Pattison 2007). The studied Otter Lake area rocks in this contribution in the Marble-domain of the CMB-Q are located < 10 km east of the Cayamant Deformation Zone (CDZ). Results from this study indicate that the injected leucosomes are petrographically and geochemical similar to the regionally extensive Chevreuil and Kensington-Skootamatta plutons along the N-S trending CDZ (Corriveau et al. 1990, 1996, 1998; Corriveau and Gorton 1993; Corriveau and Morin 2000; Morin et al. 2005).

The textural, geochemical, and geochronological data for monazite when combined with the textural and geochemical data for garnet growth help to constrain the tectonic evolution of Otter Lake area. The studied monazite ages (> ca.1245 Ma) that are older than the Elzevir Orogeny (1245 – 1220 Ma) are referred to as inherited for purposes of this study for their provenance is unknown. Garnet growth was initiated at or after ca. 1218 Ma (youngest fully-included monazite age in garnet) (Fig. 35A) during prograde metamorphism marking the end of the Elzevir Orogeny (1245 – 1220 Ma) and continued during the onset of the Shawinigan Orogeny (1190 – 1140 Ma). Monazite growth, coeval with garnet growth (Grt1; Fig. 35B) during peak Shawinigan metamorphism is recorded at ca. 1155 Ma from the injected Th- and LREE-rich monazites. The presence and abundance of almandine-rich garnet at high grade metamorphism (i.e. peak regional metamorphism during Shawinigan orogeny) reveals the Y+HREE affinity towards garnet compared to Th- and LREE-rich injected monazites (Fig. 35B). It is therefore believed that the studied injected monazites are produced by the partial to complete dissolution and resetting of pre-existing monazite (and new monazite growth) from alkali-rich fluid infiltration associated with the intrusive Chevreuil Suite (1170 – 1160 Ma).

Upon cooling, garnet growth ceased and/or breaks down (releasing Y+HREE) which subsequently were taken up by monazite precipitate (xenotime-absent assemblage) recorded in the Y- and HREE-rich in situ monazites is determined to be between ca. 1136 and 1063 Ma (Fig. 35C,D). Garnet growth ceased, at the end of the Shawinigan orogeny, and the in situ monazite leucosome crystallization ages (Fig. 35C,D) represent post-peak retrograde reactions between the matrix-defining biotite and sillimanite minerals replacing peritectic garnet (e.g. Pyle and Spear 2003). The younger ca. 1063 Ma in situ monazite neosome age within these two samples is coeval with the emplacement of the K-rich alkaline Kensington-Skootamatta plutonic (1090-1070 Ma) suite along the CDZ within the Marble-Domain, CMB-Q (Corriveau et al., 2000; Corriveau and van Breeman, 2000).

The onset of the Kensington-Skootamatta (1090 – 1070 Ma) intrusive suite initiated the second and final phase of garnet growth (smaller, almandine and spessartine-rich rims (Grt2, Fig. 35E)) recorded in the Th- and LREE-rich injected leucosome at ca. 1048 Ma (Fig. 35E). These smaller, almandine-rich garnets exhibit sharp, asymmetrical rimward reverse zoning in Mg, Fe and/or Mn (Fig. 35E) which reflect the effects of retrograde metamorphism (Woodsworth 1977) and are commonly attributed to diffusional exchange and/or network transfer reactions between garnet and biotite during cooling (e.g. Kohn et al. 2001). The ca. 1048 Ma leucosome crystallization age can be inferred as the peak Ottawan phase high-temperature metamorphism (anatexis) experienced in the area. Inasmuch, Barfod et al. (2005) recorded a crystallization age of 1031 ± 6 Ma for apatite from the Yates mine in the Otter Lake area in leucosomes within the study area. This evidence is contrary to Rivers' (2007, 2009, 2010) orogenic lid interpretation that states that rocks in this area did not experience temperature exceeding 500°C. Furthermore, Schneider et al. (2013) noted that protracted middle crustal residence of the Marble Domain

during thermally elevated conditions, is marked by post-Grenvillian cooling of the Otter Lake rocks through 500 °C, nearly 200 Ma after cooling of the Quartzite Domain, implying that portions of the orogenic lid remained warm (above 500 °C) during the Grenville Orogeny.

Late tectonic pegmatites, REE-rich with accompanied enrichments in U, Th, Mo, and Nb are widespread in the Central Metasedimentary Belt (CMB) and adjacent Central Gneiss Belt (CGB) in the southwest Grenville Province of ON and QC (Lentz 1996). Skarns in the marble-domain of the CMB-Q are commonly associated with these REE-rich pegmatites (e.g. Lentz 1996). They are interpreted to have originated by fractional crystallization of hydrous, S-type, granitoid magmas emplaced in the crust between ~1090-1050 Ma (Rivers 2012) concordant with the ca. 1063 ± 6 Ma crystallization ages of in situ leucosome (Fig. 35D). According to Lentz (1996), the fractionation of these magmas led to the formation of pegmatitic liquids and partitioning of REE into a fluid-phase, both of which eventually migrated to higher positions in the crust. The younger ages (ca. 1014 – 942 Ma; A11) in the in situ leucosome monazite could possibly be due to the late breakdown of monazite to apatite at low-temperatures or vice-versa (Spear and Pyle 2002). These younger outlier ages recorded in the Otter Lake area samples within the marble-domain can be attributed to the extensive hydrothermal alteration and are not metamorphism in the area (Lentz 1996). This implies that crystallization in the upper crust occurred after mid-crustal rocks underwent significant exhumation and cooling, compatible with a hydrothermal origin for the younger ca. 1014 – 942 Ma monazite leucosome crystallization ages during orogenic collapse (ca. 1020 Ma, Baskatong and Bancroft Shear zones; Corriveau et al. 1990; Rivers et al. 2002; McLelland et al. 2010).

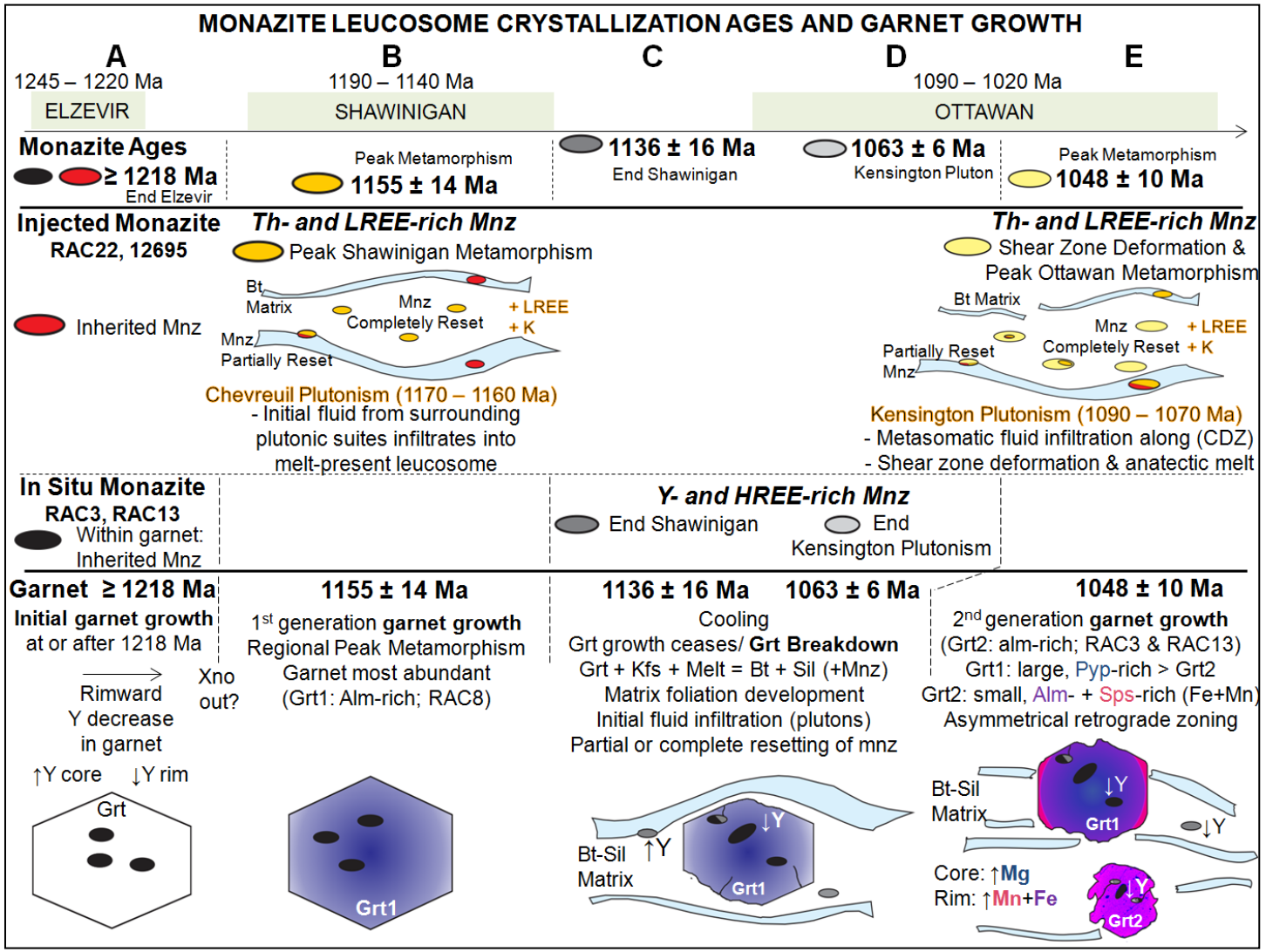

Figure 35: Schematic diagram displaying the relationship between the different stages of monazite and garnet growth and dissolution observed in the Otter Lake area rocks during the tectonic evolution of the Grenville Orogenic history for the interpreted metasomatic (injected) and anatectic (in situ) leucosome crystallization ages from monazite U-Th-Pb EMPA ages. Note that "injected monazite" and "in situ monazite" here are used to refer to both injected and in situ monazite-bearing neosomes, respectively. Injected leucosomes ages (RAC22 and 12695) show inherited monazites (red; A) completely to partially recrystallized by fluid-aided partial melting along the Cayamant Deformation Zone (CDZ) (orange, yellow; B,E). The inherited (black; A) in situ monazite leucosomes crystallization ages (RAC3, 13) and dissolution and reprecipitation (grey; C,D) ages are related to the geochemistry (end-members, Y content) for the two stages of garnet growth (Grt1, B; Grt2, E) and dissolution/breakdown (C,D). Mineral abbreviations are after Whitney and Evans (2010).

CONCLUSION

The study of rocks in Otter Lake (Marble domain of the CMB-Q), which range from upper amphibolite- to lower granulite-facies migmatites (amphibolite and diorite migmatite; Suite 1) and gneisses (stromatic grt-bt-sil gneiss; Suite 3), provide new petrographic, geochemical and monazite U-Th-Pb geochronology data that suggest the area was affected by numerous magmatic and/or metamorphic (anatectic) events during the tectonic evolution of the Grenville Orogeny:

- Two types of peraluminous S-type neosomes from Suites 1 and 3 have been recognized in this study (1) calc-alkaline injected neosomes and (2) shoshonitic in situ neosomes, respectively. The injected neosomes are typical of magmas originating from convergent margins ascribed to the release of K-, LILE- and LREE-rich fluids and melts from the crustal slab. The geochemical signatures from the injected neosomes result from the fractionation of amphibole-, pyroxene- and garnet-bearing basalt with some partial melting of the sediment-rich crustal rocks. The in situ leucosomes are most likely metasomatized mantle-derived arc magmas from partial melts from a metapelitic protolith;
- The injected leucosomes are petrographically and geochemical similar to the regionally extensive Chevreuil (1170 – 1160 Ma) and Kensington-Skootamatta (1090 – 1070 Ma) plutons along the N-S trending Cayamant Deformation Zone (CDZ). Fluid-present metasomatic alteration of these neosomes support the interpretation that continent-continent collision during the Grenville Orogeny caused shearing and deformation;
- Two generations of almandine-rich garnets are observed (Grt 1 & Grt 2). The large, porphyroblastic anhedral (Grt1), which are thought to be early nucleates formed during peak Shawinigan metamorphism at ca. 1155 ± 14 Ma. The smaller (Grt2) idioblastic

garnet are more almandine- + spessartine-rich relative to the larger pyrope-rich garnets formed during peak Ottawan Metamorphism at ca. 1048 ± 10 Ma;

- Both Grt1 and Grt2 show evidence of reverse zoning related to retrograde metamorphism. Sharp rimward zoning in Mg, Fe and/or Mn is commonly attributed to diffusional exchange and/or network transfer reactions between garnet and biotite during cooling;
- Two types of geochemically distinct monazites have been recognized (1) (Th+LREE)-rich monazites from the injected neosomes formed during melt recrystallization with the high (Th+LREE)-contents reflect the alkaline nature and presence of an external source (i.e. Chevreuil-Kensington plutonic suites), and (2) (Y+HREE)-rich monazites from the in situ neosomes formed at the expense of garnet resorption and dissolution that released Y and HREE into the melt and subsequently incorporated into the monazite structure;
- Garnet growth was initiated at or after ca. 1218 Ma (youngest fully-included monazite age in garnet) during prograde metamorphism marking the end of the Elzevir Orogeny (1245 – 1220 Ma);
- Upon cooling, garnet growth ceased. This is coeval with the end of the Shawinigan orogeny at ca. 1136 ± 16Ma and represents post-peak retrograde reactions between the matrix-defining biotite and sillimanite minerals replacing peritectic garnet. The younger ca. 1063 ± 6 Ma ages from the in situ neosomes is coeval with the emplacement of the K-rich alkaline Kensington-Skootamatta plutonic (1090-1070 Ma), a heat source necessary for subsequent complete or partial resetting of monazite;
- The ca. 1048 ± 10 Ma leucosome crystallization age represents the peak Ottawan phase, Grenvillian high-temperature (650 – 700 °C), fluid-rich metamorphism (1090 – 1020 Ma) experienced in the area. This is contrary to Rivers' orogenic lid interpretation that states

rocks in this area did not experience Ottawan metamorphism and temperature exceeding 500°C;

- The younger ca. 1014 – 942 Ma ages from the in situ leucosome monazite can be attributed to the extensive hydrothermal alteration that is unrelated to metamorphism in the area. Compatible with crystallization in the upper crust occurring after mid-crustal rocks underwent significant exhumation and cooling during orogenic collapse (ca. 1020 Ma).

REFERENCES:

Arculus, R.J., Johnson, R.W. (1981) Island arc magma sources: a geochemical assessment of the roles of slab-derived components and crustal contamination. Chemical Geology 15: 109-133.

Ayers, J.C., Miller, C., Gorisch, B., Milleman, J. (1999) Textural development of monazite during high-grade metamorphism: Hydrothermal growth kinetics, with implications for U, Th-Pb geochronology. American Mineralogist 84, 1766-1780.

Barfod, G.H., Krogstad, E.J., Frei, R., Albarède, F. (2005) Lu-Hf and PbSL geochronology of apatites from Proterozoic terranes: a first look at Lu-Hf isotopic closure in metamorphic apatite. Geochimica et Cosmochimica Acta 69, 1847-1859.

Bea, F., Pereira, M.D., Stroh, A. (1994) Mineral/leucosome trace-element partitioning in a peraluminous migmatite (a laser ablation-ICP-MS study). Chemical Geology, 117, 291-312.

Bea, F. (1996) Residence of REE, Y, Th and U in granites and crustal protoliths; implications for the chemistry of crustal melts. Journal of Petrology 37, 521 – 552.

Beaumont, C., Jamieson, R.A., Nguyen, M.H., Lee, B. (2001) Himalayan tectonics explained by excursion of a low-viscosity crustal channel coupled to focused surface denudation. Nature 414(6865): 738-742. doi:10.1038/414738a.

Bhadra, S., Das, S., Bhattacharya, A. (2007) Shear zone-hosted migmatites (eastern India): the role of dynamic melting in the generation of REE-depleted felsic melts, and implications for disequilibrium melting. Journal of Petrology, 49 (3), 435-457.

Blein, O., LaFlèche, M.R., Corriveau, L. (2003) Geochemistry of the granulitic Bondy gneiss complex: a 1.4 Ga arc in the Central Metasedimentary Belt, Grenville Province, Canada. Precambrian Research 120, 193-217.

Brown, M. (1984) The petrogenesis of some migmatites from the Presqu'ile de Rhuys, southern Britanny, France. Eds. Migmatites, melting and metamorphism, 174-200. Shiva Publishing Limited, Nantwich.

Boggs, K.J.E., Corriveau, L. (2004) Granulite-facies P-T-t paths and the influence of retrograde cation diffusion during polyphase orogenesis, western Grenville Province, Québec, *in* Tollo, R.P., Corriveau, L., McLelland, J., Bartholomew, M.J., eds., Proterozoic tectonic evolution of the Grenville orogen in North America: Boulder, Colorado, Geological Society of America Memoir 197, 35-64.

Brown, M. (1973) The definition of metatexis, diatexis and migmatite. Proceedings of the Geological Association 84, 371-382.

Brown, M., Solar, G.S. (1998a) Shear zone systems and melts: Feedback relations and self-organization in orogenic belts. Journal of Structural Geology 20, 211-227.

Brown, M., Solar, G.S. (1998b) Granite ascent and emplacement during contractional deformation in convergent orogens. Journal of Structural Geology 20, 1365-1393.

Brown, M., Solar, G.S. (1998) Shear zone systems and melts: feedback relations and self-organization in orogenic belts. Journal of Structural Geology 20, 211-227.

Brown, M. (2001) Orogeny, migmatites and leucogranites- a review. Earth and Planetary Science 110 (4), 313-336.

Brown, M. (2007) Metamorphic Conditions in Orogenic Belts: A Record of Secular Change. International Geology Review 43 (3), 193 – 234.

Busch, J.P., Mezger, K., van der Pluijm, B.A. (1997) Suturing and extensional reactivation in the Grenville orogen, Canada. Geology 25, 507-510.

Chappell, B.J., White, A.J.R. (1974) "Two Contrasting Granite Types". Pac. Geol., v8, pp.173-174.

Carr, S.D., Easton, R.M., Jamieson, R.A., Culshaw, N.G. (2000) Geological transect across the Grenville orogen of Ontario and New York. Canadian Journal of Earth Science 37, 193-216.

Castro, A., Garcia Moreno, O., El-Hmidi, H., Corretge, L.G. (2002) Dissolution of mafic microgranular enclaves by decompression melting in water-saturated granitic magma. EMPG IX, ETH Zurich. Journal of Conference Abstracts 7 (1), 23.

Chappell, B.W., White, A.J.R. (1974) Two contrasting granite types. Pacific Geology 8, 1-26.

Cocherie, A., Legendre, O., Peucat, J-J., and Kouamelan, A.N. (1998) Geochronology of polygenetic monazites constrained by in situ electron microprobe Th-U-total Pb determination: implications for lead behaviour in monazite. Geochimica Cosmochimica Acta 62, 2475–2497.

Condie, K.C. (1989) Growth and accretion of continental crust: inferences based on Laurentia. Chemical Geology 83, 183 – 194.

Corriveau, L. (1990) Proterozoic subduction and terrane amalgamation in the southwestern Grenville province, Canada: Evidence from ultrapotassic to shoshonitic plutonism. Geology 14, 614 – 617.

Corriveau, L., Heaman, L.M., Marcantonio, F., van Breeman, O. (1990) 1.1 Ga K-rich alkaline plutonism in the SW Grenville Province. Contributions to Mineralogy and Petrology 105, 473-485.

Corriveau, L., Gorton, M.P. (1993) Coexisting K-rich alkaline and shoshonitic magmatism of arc affinities in the Proterozoic: a reassessment of syenitic stocks in the southwestern Grenville Province. Contributions to Mineralogy and Petrology 113, 262-279.

Corriveau, L., van Breeman, O. (1994) The Central Metasedimentary Belt of Quebec: are terrane boundaries largely cryptic? Geological Association of Canada- Mineralogical Association of Canada Abstract Program, 19, A23.

Corriveau, L., Leblanc, D. (1995) Sequential nesting of magmas in marble, southwestern Grenville Province, Québec: from fracture propagation to diapirism. Tectonophysics 246, 183-200.

Corriveau, L., Tellier, M.L., Morin, D. (1996) Le dyke de minette de Rivard et le complexe gneissique cuprifère de Bondy; implications tectoniques et métallogéniques pour la région de Mont-Laurier, Province de Grenville, Québec. Commission géologique du Canada, Dossier public 3078.

Corriveau, L., Morin, D. (2000) Modelling 3D architecture of western Grenville from surface geology, xenoliths, styles of magma emplacement, and Lithoprobe reflectors. Canadian Journal of Earth Sciences 37, 235-251.

Corriveau, L., van Breeman, O. (2000) Docking of the Central Metasedimentary Belt to Laurentia in geon 12: evidence from the 1.17-1.16 Ga Chevreuil intrusive suite and host gneisses, Quebec. Canadian Journal of Earth Science 37, 253-269.

Corriveau, L., Heaman, L.M., Marcantonio, F., van Breeman, O. (1990) 1.1 Ga K-rich alkaline plutonism in the SW Grenville Province. Contributions to Mineralogy and Petrology 105, 473-485.

Corriveau, L., Tellier, M.L., Morin, D. (1996) Le dyke de minette de Rivard et le complexe gneissique cuprifère de Bondy; implications tectoniques et métallogéniques pour la région de Mont-Laurier, province de Grenville, Québec.

Corriveau, L., Rivard, B., van Breeman, O. (1998) Rheological controls on Grenvillian intrusive suites: implications for tectonic analysis. Journal of structural Geology 20 (9-10), 1191-1204.

Crowley, J.L., Chatterjee, N., Bowring, S.A., Sylvester, P.J., Myers, J.S., Searle, M.P. (2005) U-(Th)-Pb dating of monazite and xenotime by EMPA, LA-ICPMS, and IDTIMS: examples from the Yilgarn Craton and Himalayas. Proceedings of the 15th Annual Goldschmidt Conference Abstracts, pA19.

Culshaw, N.G., Jamieson, R.A., Ketchum, J.W.F., Wodicka, N., Corrigan, D., Reynolds, P.H. (1997) Transect across the northwestern Grenville orogen, Georgian Bay, Ontario: Polystage convergence and extension in the lower orogenic crust. Tectonics 16 (6), 966-982.

Dahl, P.S., Hamilton, M.A., Jercinovic, M.J., Terry, M.P., Williams, M.L., Frei, R. (2005) Comparative isotopic and chemical geochronometry of monazite, with implication for U-Th-Pb dating by electron microprobe: An example from metamorphic rocks of the eastern Wyoming Craton (U.S.A). American Mineralogist 90, 619-638.

Davidson, A. (1995) A review of the Grenville orogen in its North American type area, AGSO. Journal of Australian Geology and Geophysics. 16, 3-24.

Deer, W.A., Howie, R.A., Zussman, J. (1966) An introduction to the rock forming Minerals. Longman and Green, London 1 966: pp. 528.

Dewey, J.F., Burke, K.C.A. (1973) Tibetan, Variscan and Precambrian basement reactivation: products of continental collision. The Journal of Geology 81 (6), 683-692.

Doig, R. (1990) U-Pb zircon dates of Morin anorthosite suite rocks, Grenville Province, Quebec. Journal of Geology 99, 729 – 738.

Exley, R.A. (1980) Microprobe studies of REE-rich accessory minerals: Implications for Skye granite petrogenesis and REE mobility in hydrothermal systems. Earth Planetary Science Letters 48, 97-110.

Fornelli, A., Piccarreta, G., Del Moro, A., Acquafredda, P. (2002) Multi-stage melting in the lower crust of the Serre (Southern Italy). Journal of Petrology 43 (12), 2191-2217.

Foster, G., Kinny, P., Prince, C., Vance, D., Harris, N. (2000) The significance of monazite U-Th-Pb age data in metamorphic assemblages; a combined study of monazite and garnet chronometry. Earth and Planetary Science Letters 181, 327-340.

Foster, G., Parrish, R.R. (2003) Metamorphic monazite and the generation of P-T-t paths, from Vance, D., Muller, W., and Villa, I.M., (eds) Geochronology: Linking the Isotopic Record with Petrology and Textures. Geological Society, Special Publications 22, 25-47.

Frost, B.R., Calvin, C.G., Collins, W.J., Arculus, R.J., Ellis, D.J., Frost, C.D. (2001) A geochemical classification for granite. Journal of Petrology 42 (11), 2033-2048.

Harris, N.B.W., Duyverman, H.J. and Almond, D.C. (1983) The trace element and isotopegeochemistry of the Sabaloka igneouscomplex, Sudan. Jour. Geol. Soc. London,V. 140, pp. 245–256.

Harlov, D.E., Hetherington, C.J. (2010) Partial high-grade alteration of monazite using alkali-bearing fluids: experiments and nature. American Mineralogist 95, 1105-1108.

Heaumann, L.M., Machado, N., Krogh, T.E., Weber, W. (1986) U-Pb zircon ages for the Molson dyke swarm and the Fox River sill: Constraints for Early Proterozoic crustal evolution in northeastern Manitoba, Canada. Contributions to Mineralogy and Petrology 94, 82-89.

Heaman, L.M., Davis, D.W., Krough, T.E., Lumbers, S.B. (1987) Geological evolution of the Central Metasedimentary Belt (CMB), Ontario: a U-Pb perspective. Geological Association of Canada/Mineralogical Association of Canada. Progressive Abstract 12:54.

Hynes, A., Rivers, T. (2010) Protracted continental collision- evidence from the Grenville Orogen. Canadian Journal of Earth Science 47, 591-620.

Indares, A., Martignole, J. (1990) Metamorphic constraints on the evolution of the gneisses from the parautochtonous and allochthonous polycyclic belts, Grenville Province, western Quebec. Canadian Journal of Earth Science 27, 357-370.

Indares, A., Dunning, G., Valverde, C., Jenner, G. (2000) 1.4 to 1.2 Ga crustal evolution of the central Grenville Province: new insights from the Manicouagan – Baie Comeau transect. EOS Transactions of the American Geophysical Union. 90(22): Abstract GA71C-04.

Jung, S., Hoernes, S., Masberg, P., Hoffer E. (1999) The petrogenesis of some migmatites and granites (Central Damara Orogen, Nambia): Evidence for disequilibrium melting, wall-rock contamination and crystal fractionation. Journal of Petrology 40 (8), 1241-1269.

Kennedy, A.K., Kamo, S.L., Nasdala, L., Timms, N.E. (2010) Grenville Skarn Titanite: potential reference material for SIMS U-Th-Pb analyses. The Canadian Mineralogist 48, 1423-1443.

Ketchum, J.W.F., Heaman, L.M., Krogh, T.E., Culshaw, N.G., Jamieson, R.A. (1998) Timing and thermal influence of late orogenic extension in the lower crust: a U-Pb geochronological study from the southwest Grenville orogen, Canada. Precambrian Research 89 (1-2), 25-45.

Kohn, M. J., Spear, F.S. (2000) Retrograde net transfer reaction insurance for pressure-temperature estimates. Geology 28, 1127–1130.

Kohn, M. J. (2001) Timing of arc accretion in the southern Appalachians: Perspectives from the Laurentian margin. Geological Society of America. Abstract Program 33, A-262.

Kohn, M.J., Malloy, M.A. (2004) Formation of monazite via prograde metamorphic reactions among common silicates: Implications for age determinations. Geochimica et Cosmochimica Acta 68 (1), 101-113.

Kohn, M.J., Wieland, M.S., Parkinson, C.D., Upreti, B.N. (2005) Five generations of monazite in Langtang gneisses: inplications for chronology of the Himalayan metamorphic core. Journal Metamorphic Geology. 23, 399-406.

Krenn, E., Finger, F. (2007) Formation of monazite and rhabdophane at the expense of allanite during Alpine low temperature retrogression of metapelitic basement rocks from Crete, Greece: microprobe data and geochronological implications. Lithos 95, 130–147.

Krenn, E., Finger, F. (2010) Unusually Y-rich monazite-(Ce) with 6-14 wt.% Y_2O_3 in a granulite from the Bohemian Massif: implications for high temperature monazite growth from the monazite-xenotime miscibility gap thermometry. Mineralogical Magazine 74 (2), 217-225.

Kretz, R. (1959) Chemical study of Garnet, Biotite, and Hornblende from gneisses of southwestern Quebec, with emphasis on distribution of elements in coexisting minerals. The Journal of Geology 67 (4), 371-402.

Kretz, R. (1977) Geology of the Fort Coulonge - Otter Lake – Kazabazua area, Pontiac and Gatineau Counties, Quebec: Rept. in files, Ministère des Richesses Naturelles, Quebec.

Kretz, R. (1978) Distribution of Mg, Fe^{2+}, and Mn in some calcic Pyroxene-Hornblende-Biotite-Garnet Gneisses and Amphibolites from the Grenville Province. The Journal of Geology 86 (5), 599-619.

Kretz, R. (1980) Occurrence, mineral chemistry, and metamorphism of Precambrian carbonate rocks in a portion of the Grenville Province. Journal of Petrology 21: 573-620.

Kretz, R. (1990) Biotite and garnet compositional variation and mineral equilibria in Grenville gneisses of the Otter Lake area, Quebec. Journal of Metamorphic Geology 8, 493-506.

Kretz, R. (1994a) Petrology of veined gneisses of the Otter complex, southern Grenville Province. Canadian Journal of Earth Sciences 31, 835-851.

Kretz, R. (2005) Subsolidus evolution of gneissic biotite syenite and nepheline syenite, Otter Lake area, Quebec. The Canadian Mineralogist 43, 1107-1122.

Kretz, R. (2007) Geological Report, Otter Lake, Québec. Ministère des Ressources naturelles et de la Faune, Québec (unpubl. report).

Kretz, R. (2009) Metamorphic transformations in two metamorphic complexes dominated by heterogeneous Ca-Pyroxene-Hornblende granite and syenite, Otter Lake area, Quebec, Canada. The Canadian Mineralogist 47, 1137-1158.

Kretz, R. (2006) Shape, size, spatial distribution and composition of garnet crystals in highly deformed gneiss of the Otter Lake area, Quebec, and a model for garnet crystallization. Journal of Metamorphic Geology 24 (6), 431-449.

Kretz, R., Jones, P., Hatree, R. (1989a) Grenville metagabbro complexes of the Otter Lake area, Quebec. Canadian Journal of Earth Sciences, 26, 215-230.

Kretz, R., Campbell, J.L., Hoffman, E.L., Hatree, R., Teesdale, W.J. (1999) Approaches to equilibrium in the distribution of trace elements among the principle minerals in a high-grade metamorphic terrane. Journal of Metamorphic Geology 17, 41-59.

Lentz, D. (1996) U, Mo, REE mineralization in late-tectonic granitic pegmatites, Southwestern Grenville Province. Ore Geology Reviews 11, 197-227.

Linthout, K. (2007) Tripartite division of the system $2REEPO_4 – CaTh(PO_4)_2 – 2ThSiO_4$, discreditation of brabantite, and recognition of cheralite as the name for members dominated by $CaTh(PO_4)_2$. Canadian Mineralogist 45, 503-508.

Longerich, H.P. (1993) Application of a new treated LiF200 crystal to X-Ray fluorescence analysis of geological samples. X-Ray Spectrometry 22, 114-118.

Longerich, H.P., Jenner, G.A., Fryer, B.J., Jackson, S.E. (1990) Inductively coupled plasma-mass spectrometric analysis of geological samples: A critical evaluation based on case studies. Chemical Geology 83, 105-118.

Longerich, H.P., Jackson, S.E., Fryer B.J., Strong, D.F. (1993) The laser ablation microprobe-inductively coupled plasma-mass spectrometer. Geoscience Canada 20, 21-27.

Ludwig, K.R. (1993) A Computer Program for Processing Pb-U-Th Isotope Data. United States Geological Survey Open-File Report, 88-542.

Ludwig, K.R. (2000) User Guide- Isoplot/Ex- A geochronological toolkit for Microsoft Excel. Excel Add-in.

Martignole, J., Calvert, A. J., Friedman, R., Reynolds, P. (2000) Crustal evolution along a seismic section across the Grenville Province (western Quebec). Canadian Journal of Earth Sciences 37, 291–306.

McFarlane, C.R.M., Connelly, J.N., Carlson, W.D. (2005) Monazite and xenotime petrogenesis in the contact aureole of the Makhavinekh Lake Pluton, northern Labrador. Contributions to Mineralogy and Petrology 148, 524–541.

McLelland, J.M., Selleck, B.W., Bickford, M.E. (2010) Review of the Proterozoic evolution of the Grenville Province, its Adirondack outlier, and the Mesoproterozoic inliers of the Appalachians, *in* Tollo, R.P., Bartholomew, M.J., Hibbard, J.P., and Karabinos, P.M., eds., From Rodinia to Pangea: The Lithotectonic Record of the Appalachian Region: Geological Society of America Memoir 206, 1–29. doi: 10.1130/2010.1206(02)

Middlemost, E.A.K. (1994) Naming minerals in magma/igneous rock system. Earth Science Review 37, 215-224.

Miller, C.F. (1985) Are strongly peraluminous magmas derived from pelite sedimentary sources?" Journal of Geology 93 (6), 673-689.

Milord, I., Sawyer, E.W., Brown, M. (2001) Formation of diatexite migmatite and granite magma during anatexis of semi-pelitic metasedimentary rocks: an example from St. Malo, France. Journal of Petrology 42, 487-505.

Montel, J.M. (1993) A model for monazite/melt equilibrium and application to the generation of granitic magmas. Chemical Geology 110, 127-146.

Montel, J.-M., Foret, S., Veschambre, M., Nicollet, C., Provost A. (1996) Electron microprobe dating of monazite. Chemical Geology 131, 37-53.

Montel, J.-M., Kornprobst, J., Vielzeuf, D., (2000) Preservation of old U-Th-Pb ages in shielded monazite: example from Beni Bousera Hercynian kinzigites (Marocco). Journal of Metamorphic Geology 18, 335–342.

Moore, J., Thompson, P. (1980) The Flinton Group; A late Precambrian metasedimentary sequence in the Grenville Province of eastern Ontario. Canadian Journal of Earth Sciences 17, 1685-1707.

Morin, D., Hébert, R., Corriveau, L. (2005) Mesoproterozoic deep K-magmatism recorded in a megacryst- and xenoliths-bearing minette dyke, western Grenville Province. Canadian Journal of Earth Sciences 42, 1881-1906.

Nehring, F., Foley, S.F., Holtta, P., Van Der Kerkhof, A.M. (2009) Internal differentiation of the Archean continental crust: fluid-controlled partial melting of granitlutes and TTG-amphibolite associations in central Finland. Journal of Petrology 50, 3-35.

Overstreet, W.C. (1967) The geological occurrence of monazite. U.S. Geological Survey Progress Paper. 530pp.

Pan, Y (1997) Zircon- and Monazite-forming metamorphic reactions at Manitouwadge, Ontario. The Canadian Mineralogist 35, 105-118.

Parrish, R.R. (1990) U-Pb dating of monazite and its application to geological problems. Canadian Journal of Earth Sciences 27, 1431-1450.

Passchier, C.W., Trouw, R.A.J. (1996) Microtectonics. Springer – Verlag, Berlin Heidelberg.

Pearce, J.A., Harris, N.B.W., Tindle, A.G. (1984) Trace element discrimination diagrams for the tectonic interpretation of granitic rocks. Journal of Petrology 25, 956 – 983.

Peccerillo, A., Taylor, S.R. (1976) Geochemistry of Eocene calc-alkaline volcanic rocks from the Kastamonu area, northern Turkey. Contributions to Mineralogy and Petrology 58, 63 – 81.

Peck, W.H., Clechenko, C.C., Hamilton, M.A., Valley, J.W. (2010) Oxygen isotopes in the Grenville and Nain AMCG Suites: Regional aspects of the crustal component in massif anorthosites: Canadian Mineralogist 48, 764-786.

Perkins III, D., Essene, E.J., Marcotty, L.A. (1982) Thermometry and barometry of some amphibolite-granulite facies from the Otter Lake area, southern Quebec. Canadian Journal of Earth Sciences 19, 1759-1774.

Petrik, I., Konecny, P. (2009) Metasomatic replacement of inherited metamorphic monazite in a biotite-granite from the Nizke Tatry Mountains, Western Carpathians, Slovakia: chemical dating and evidence for disequilibrium melting. American Mineralogist 94, 957-974.

Poitrasson F., Chenery S., and Bland D. J. (1996) Contrasted monazite hydrothermal alteration mechanisms and their geochemical implications. Earth and Planetary Science Letters 145, 79–96.

Pouchou, J.L., Pichoir, F., (1991) Quantitative analysis of homogeneous or stratified microvolumes applying the model "PAP", in "Electron Probe Quantitation", Ed Heinrich and Newbury, Plenum Press, New York. 31-75pp.

Pyle, J.M., Spear, F.S. (1999) Yttrium zoning in garnet: coupling of major and accessory phases during metamorphic reactions. Geological Mineral Research 1 (6), 1-49.

Pyle, J.M., Spear, F.S. (2000) An empirical garnet (YAG) – xenotime thermometer. Contributions to Mineralogy and Petrology. 138, 51-58.

Pyle, J.M., Spear, F.S., Rudnick, R.L., McDonough, W.F. (2001) Monazite-Xenotime-Garnet equilibrium in metapelites and a new Monazite-Garnet thermometer. Journal of Petrology 42 (11), 2083-2107.

Pyle, J.M., Spear, F.S. (2003) Four generations of accessory phase growth in low-pressure migmatites from SW New Hampshire. American Mineralogist 88, 338-351.

Rapp, R.P., Watson, E.B. (1986) Monazite solubility and dissolution kinetics: implications for the thorium and light rare earth chemistry of felsic magmas. Contributions to Mineralogy and Petrology 94, 304-216.

Rivers, T. (1997) Lithotectonic elements of the Grenville Province: review and tectonic implications. Precambrian Research 86, 117-154.

Rivers, T. (2008) Assembly and preservation of lower, mid, and upper orogenic crust in the Grenville Province- Implications for the evolution of large hot long-duration orogens. Precambrian Research 167, 237-259.

Rivers, T. (2009) The Grenville Province as a large hot long-duration collisional orogen- insights from the spatial and thermal evolution of its orogenic fronts. Geological Society, London, Special Publications 327, 405-444. doi: 10.1144/SP327.17

Rivers, T. (2012) Upper-crustal orogenic lid and mid-crustal core complexes: signature of a collapsed orogenic plateau in the hinterland of the Grenville Province. Canadian Journal of Earth Sciences 49, 1-42. doi:10.1139/E11-014

Rivers, T., Ketchum, J., Indares, A., Hynes, A. (2002) The High Pressure belt in the Grenville Province: architecture, timing, and exhumation. Canadian Journal of Earth Sciences 39, 867-893.

Roeder, P.L. (1985) Electron-microprobe analysis of minerals for rare-earth elements: use of calculated peak-overlap corrections. Canadian Mineralogist 23, 263–271.

Sawyer, E.W. (2008) Atlas of migmatites. Canadian Mineralogist Special Publication 9, Mineralogical Association of Canada, Quebec, Canada, 373p.

Scherrer, N. C., Engi, M., Gnos, E., Jakob, V., Lietchi, A. (2000) Monazite analysis: from sample preparation to microprobe age dating and REE quantification. Schweizer Mineralogische und Petrographische Mitteilungen 80, 93-105.

Scherrer, E., Munker, C. & Mezger, K. (2001) Calibration of the lutetium–hafnium clock. Science 293, 683–687.

Schneider, D.A., Cope, N., Holm, D.K. (2013) Thermochronology of the Mont Laurier terrane, southern Canadian Grenville Province, and its bearing on defining crustal architecture. Precambrian Research 226,43-58.

Searle, M.P., Parish, R.R., Hodges, K.V., Hurford, A., Ayres, M.W., Whitehouse, M.J. (1997) Shisha Pangma Lecogranite, South Tibetan Himalayan: Field relations, geochemistry, age, origin and emplacement. Journal of Geology 105 (3), 295-317.

Seydoux-Guillaume, A.M., Wirth, R., Nasdala, L., Gottschalk, M., Montel, J.-M., and Heinrich, W. (2002b) An XRD, TEM and Raman study of experimentally annealed natural monazite. Physics and Chemistry of Minerals 29, 240–253.

Seydoux-Guillaume, A.M., Goncalves, P., Wirth, R., Deutsch, A. (2003) TEM study of polyphasic and discordant monazites: site specific specimen preparation using the Focused Ion Beam technique. Geology 31, 973-976.

Seydoux-Guillaume, A.M., Wirth, R., Deutsch, A., Schärer, U. (2004) Microstructure of 24 - 1928 Ma concordant monazites: implications for geochronology and nuclear waste deposits. Geochimica et Cosmochimica Acta 68, 2517-2527.

Seydoux-Guillaume, A.M., Wirth, R., Ingrin, J. (2007) Contrasting response of $ThSiO_4$ and monazite to natural irradiation. European Journal of Mineralogy 19, 7-14.

Shand, S.J. (1927) Eruptive Rocks, Murby, London.

Solar, G.S., Brown, M. (2001) Petrogenesis of migmatites in Maine, USA: possible source of peraluminous leucogranite in plutons. Journal of Petrology 42, 313-345.

Spear, F.S. (1991) On the interpretation of peak metamorphic temperatures in light of garnet diffusion during cooling. Journal of Metamorphic Geology 9, 379-388.

Spear, F.S. (1993a) Metamorphic phase equilibria and pressure-temperature-time paths: Washington, D.C., Mineralogical Society of America, 799pp.

Spear, F. S. (1993b) Inverted metamorphism, P-T paths and tectonic history of west-central New Hampshire, in Cheney, J. T., et al., eds., Field trip guidebook for the northeastern United States: Boston, University of Massachusetts, D28–D33pp.

Spear, F., Daniel, C. (1998). Three-dimensional imaging of garnet porphyroblast sizes and chemical zoning: Nucleation and growth history in the garnet zone. Geological Materials Research, Vol. 1, pp. 1-42.

Spear, F.S., Kohn, M.J. and Paetzold, S. (1995) Petrology of the regional sillimanite zone, west-central New Hampshire, U.S.A. with implications for the development of inverted isograds. American Mineralogist 80, 361-376.

Spear, F.S., Kohn, M.J., Cheney, J.T. (1999) P-T paths from anatectic pelites. Contributions to Mineralogy and Petrology 134, 17-32.

Spear, F.S., Pyle, J.M. (2002) Apatite, monazite, and xenotime in metamorphic rocks. In M.J. Kohn, J. Rakovan, and J.M. Hughes, Eds. Phosphates: Geochemical, Geobiological, and Materials Importance 48, 293-335. Reviews in Mineralogy and Geochemistry, Mineralogical Society of America, Washington, D. C.

Pyle, J.M., Spear, F.S. (2003) Four generations of accessory phase growth in low-pressure migmatites from SW New Hampshire. American Mineralogist, 88, 338-351.

Stagstad, T., Jamieson, R.A., Culshaw, N.G. (2005) Formation, crystallization, and migration of melt in the mid-orogenic crust: Muskoka Domain migmatites, Grenville Province, Ontario. Journal of Petrology 46 (5), 893-919. doi:10.1093/petrology/egi004

Stern, R.A., Berman, R.G. (2000) Monazite U-Pb and Th-Pb geochronology by ion microprobe, with an application to in situ dating of an Archean metasedimentary rock. Chemical Geology, 172, 113-130.

Suzuki, K., Adachi, M. (1991) The chemical Th-U-total Pb isochron ages of zircon and monazite from the Gray Granite of the Hida Terrane, Japan. Nagoya University 38, 11-38.

Suzuki, K., Adachi, M., Kajizuka, I. (1994) Electron microprobe observations of Pb diffusion in metamorphosed detrital monazites. Earth and Planetary Science Letters 128, 391-405.

Taylor, S. R., McClennan, S. M. (1985) The Continental Crust: Its Composition and Evolution. Blackwell, Oxford. 312. http://meteorites.wustl.edu/goodstuff/ree-chon.htm

Tiepolo, M., Tribuzio, R. (2008) Petrology and U-Pb zircon geochronology of amphibole-rich cumulates with sanukitic affinity from Husky Ridge (northern Victoria Land, Antartica); insights into the role of amphibole in the petrogenesis of subduction related magmas. Journal of Petrology 49, 937-970.

Timmerman, H., Jamieson, R.A., Parrish, R.R., Culshaw, N. (2002) Coeval migmatites and granulites, Muskoka domain, Southwestern Grenville Province. Canadian Journal of Earth Sciences 39, 239-258.

Tollo, R.P., Corriveau, L., McLelland, J., Bartholomew, M.J., eds. (2004) Proterozoic tectonic evolution of the Grenville orogen in North America: Boulder, Colorado, Geological Society of America Memoir 197, 820pp.

Tomkins, H.S., Pattison, D.R.M. (2007) Accessory phase petrogenesis in relation to major phase assemblages in pelites from the Nelson contact aureole, southern British Columbia. *Journal of Metamorphic Geology* 25, 401-421.

Tuccillo, M. E., Essene, E. J., van der Pluijm, B. A. (1990). Growth and retrograde zoning in garnets from high-grade metapelites: implications for pressure–temperature paths. Geology 18, 839–842.

van Breemen, O., Davidson, A. (1988) U-Ph zircon ages of granites and syenites in the Central Metasedimentary Belt, Grenville Province, Ontario. In: Radiogenic Age and Isotope Studies, Rep. 2. Geological Survey of Canada Papers 88 (2), 45-50.

Vernon, R., 2000. Review of microstructural evidence of magmatic and solid and solid-state flow. Electronic Geosciences 5 (2).

Ward, C., McArthur, J., Walsh, J. (1992) Rare-earth element behaviour during evolution and alteration of the Dartmoor Granite, SW England. Journal of Petrology 33, 785-815.

Whitney, D.L., Evans, B.W. (2010) Abbreviations for names of rock-forming minerals. American Mineralogist 95, 185-187.

Williams, M.L., Jercinovic, M.J. (2002) Microprobe monazite geochronology: putting absolute time into microstructural analysis. Journal of Structural Geology 24, 1013-1028.

Williams, M.L., Jercinovic, M.J., Hetherington, C.L. (2007) Microprobe monazite geochronology: Understanding geological processes by integrating composition and geochronology. Annual Reviews of Earth and Planetary Sciences 35, 137–175.

Whittington, A.G., Harris, N.B.W., Butler, R.W.H. (1999) Contrasting anatectic styles at Nanga Parbat, Northern Pakistan. Geological Society of America Special Paper 328 p. 129-143.

Wynne-Edwards, H. R. (1972) The Grenville Province. In: Price, R. A., Douglas, R. J. W., (eds) Variations in Tectonic Styles in Canada. Geological Association of Canada Special Paper 11, 263–334.

Yang, P., Rivers, T. (2002) Trace element zoning in pelitic garnet, apatite and epidote group minerals: The origin of Y annuli and P zoning in garnet. Geological Materials Resources 4, 1-35.

Zhu, X.K., O'Nions, R.K. (1999) Monazite chemical composition: some implications for monazite geochronology. Contributions to Mineralogy and Petrology 137, 351-363.

APPENDIX I: FIGURES

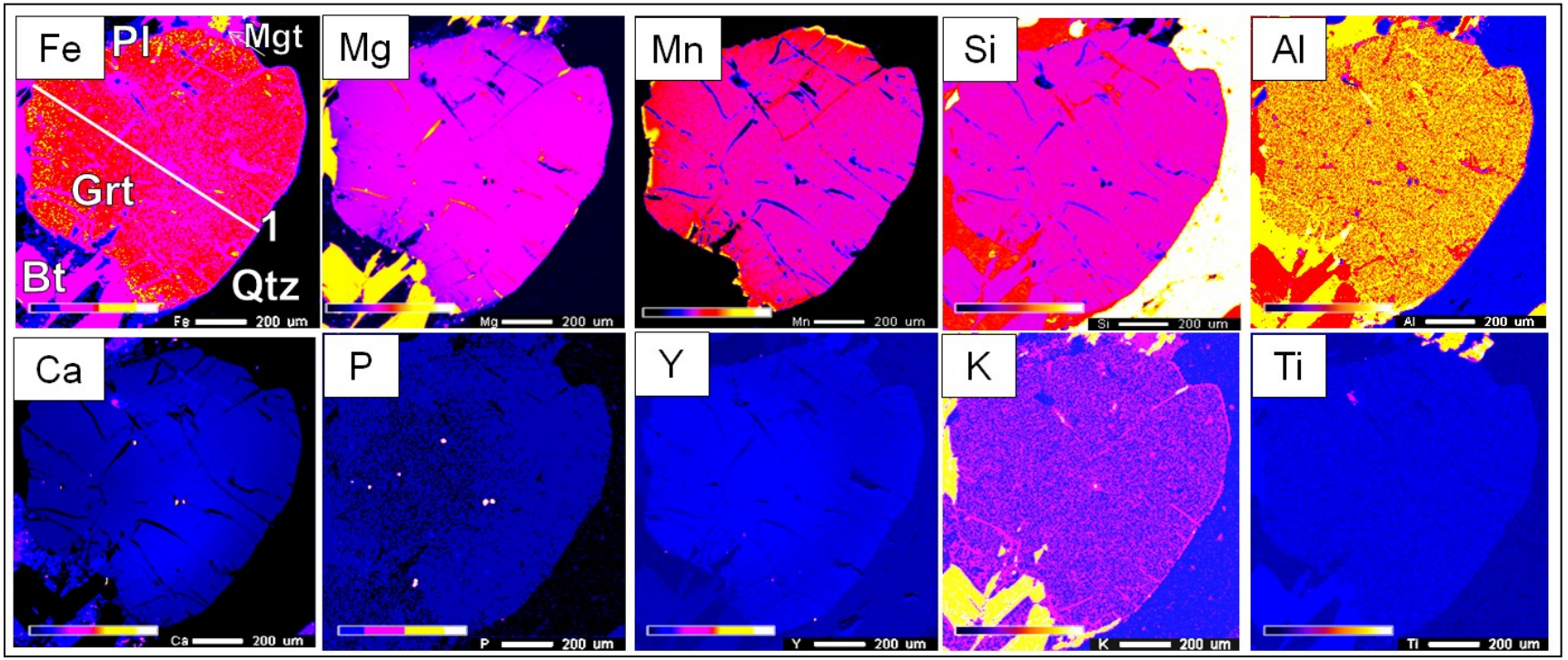

Figure A1: X-ray compositional maps for Fe, Mg, Mn, Si, Al, Ca, P, Y, K, and Ti in garnet RAC3-1 from stromatic Grt-Bt-Sil gneiss, Suite 3. Mg map showing a slight decrease along the rim in contact with biotite whereas Mn shows a slight increase in the Mn along the garnet rim in contact with biotite. A white line in the Fe map (a) marks the locating of the zoning profile in Fig. 20. Mineral abbreviations are after Whitney and Evans (2010).

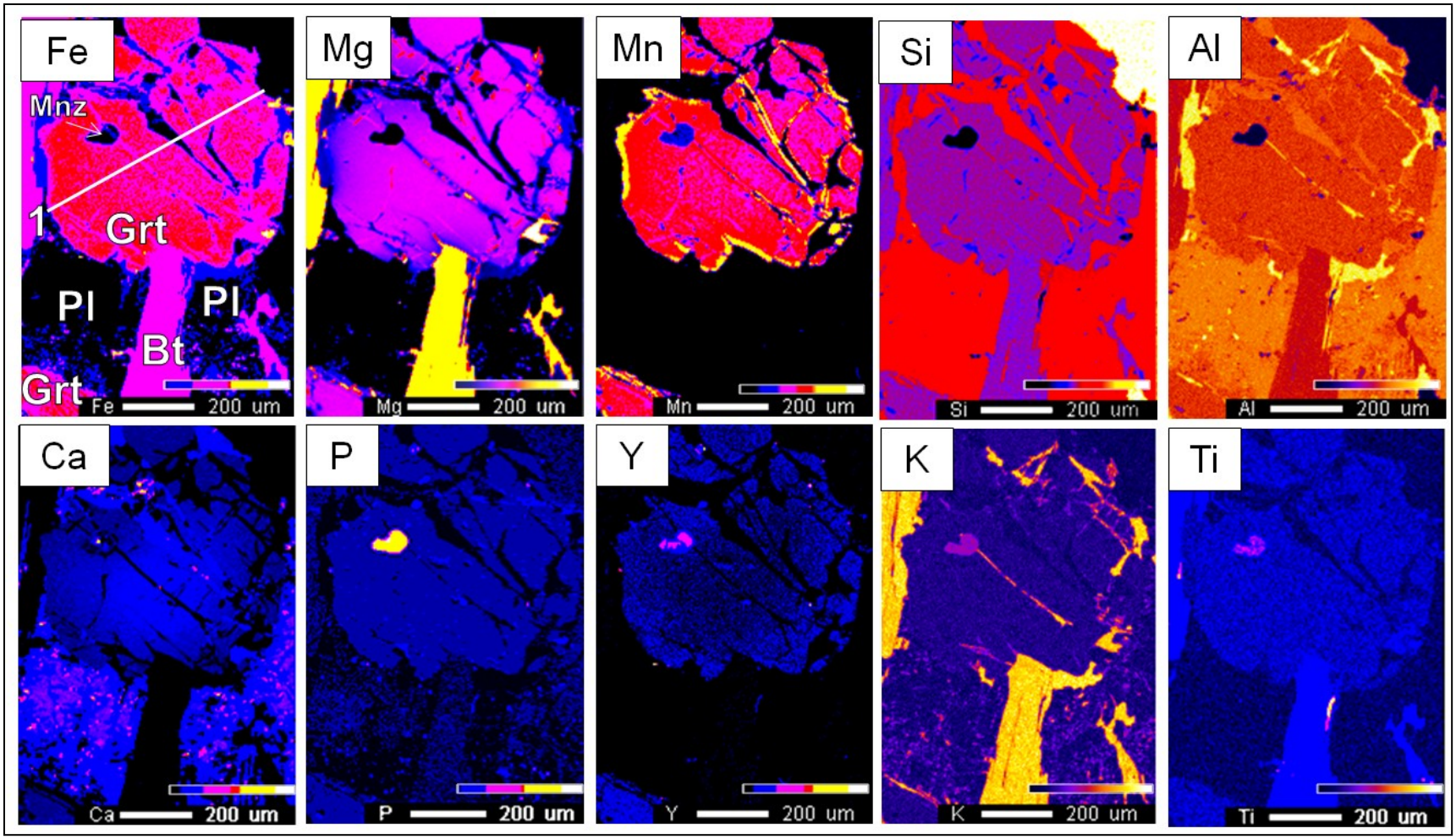

Figure A2: X-ray compositional maps for Fe, Mg, Mn, Si, Al, Ca, P, Y, K, and Ti in garnet RAC3-2 from stromatic Grt-Bt-Sil gneiss, Suite 3. Mg map showing a slight decrease along the rim in contact with biotite whereas the Mn map shows a slight increase in Mn along the garnet rim in contact with biotite. A white line in the Fe map marks the locating of the zoning profile in Fig. 20. Mineral abbreviations are after Whitney and Evans (2010).

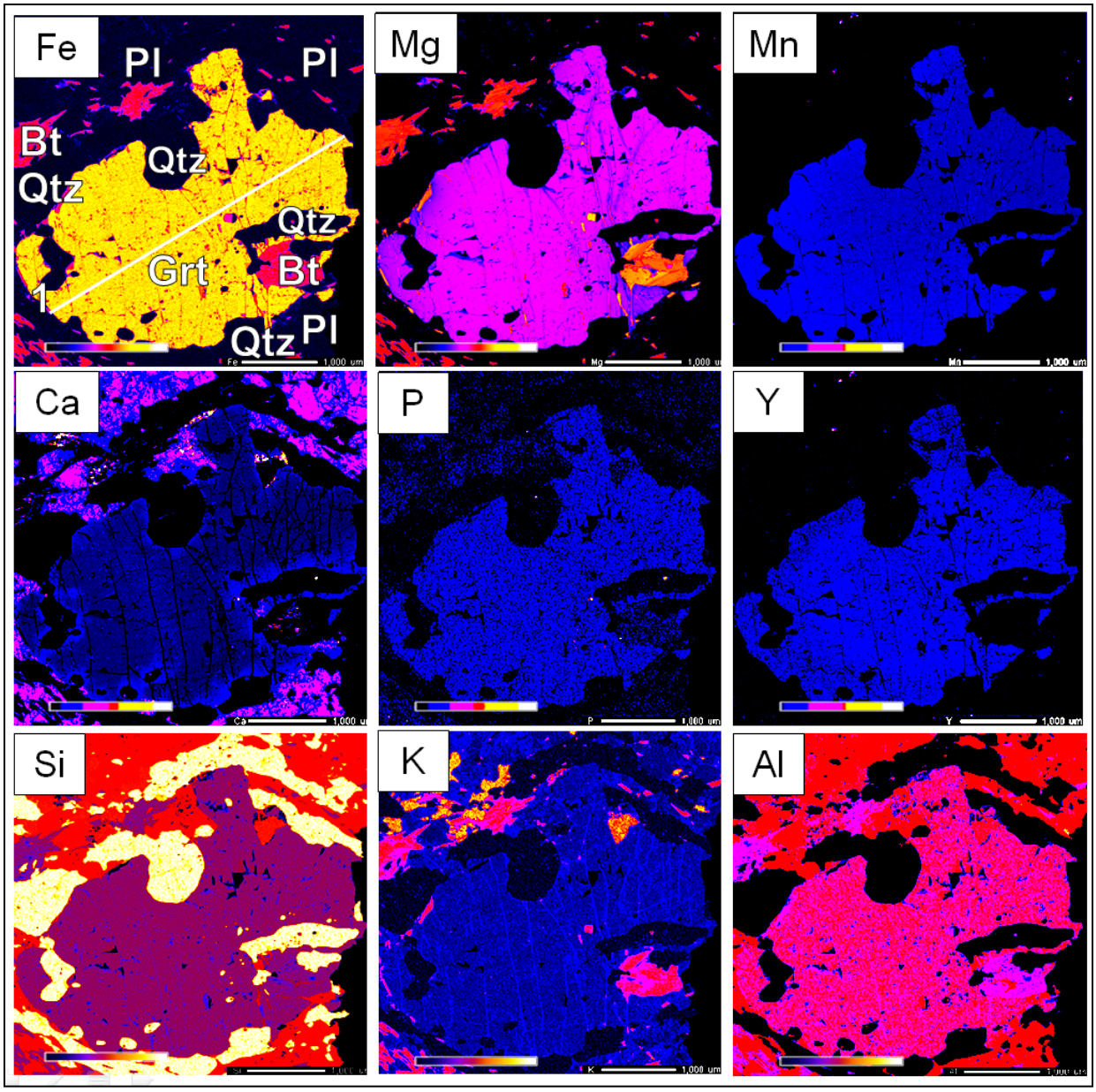

Figure A3: X-ray compositional maps for Fe, Mg, Mn, Si, Al, Ca, P, Y, K, and Ti in garnet RAC8-1 from stromatic Grt-Bt-Sil gneiss, Suite 3. Mg map showing a slight decrease along the rim in contact with biotite whereas the Mn map shows a slight increase in Mn along the garnet rim in contact with biotite. A white line in the Fe map marks the locating of the zoning profile in Fig. 21. Mineral abbreviations are after Whitney and Evans (2010).

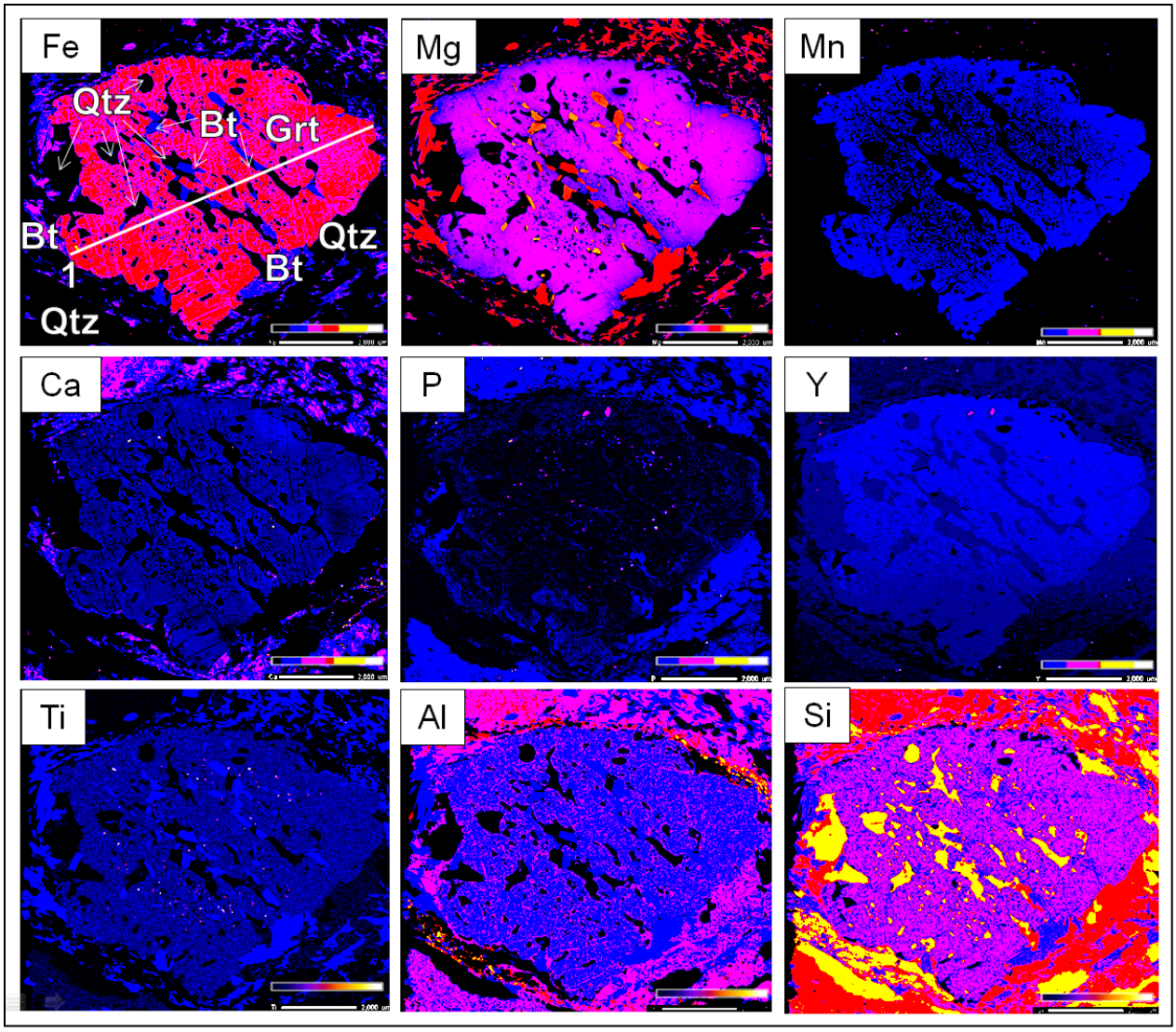

Figure A4: X-ray compositional maps for Fe, Mg, Mn, Si, Al, Ca, P, Y, K, and Ti in garnet RAC8-2 from bt-sil-grt gneiss, Suite 3. Slight decrease in Mg in matrix biotites relative to bt inclusions within the homogeneous garnet. A white line in the Fe map marks the locating of the zoning profile in Fig. 21. Mineral abbreviations are after Whitney and Evans (2010).

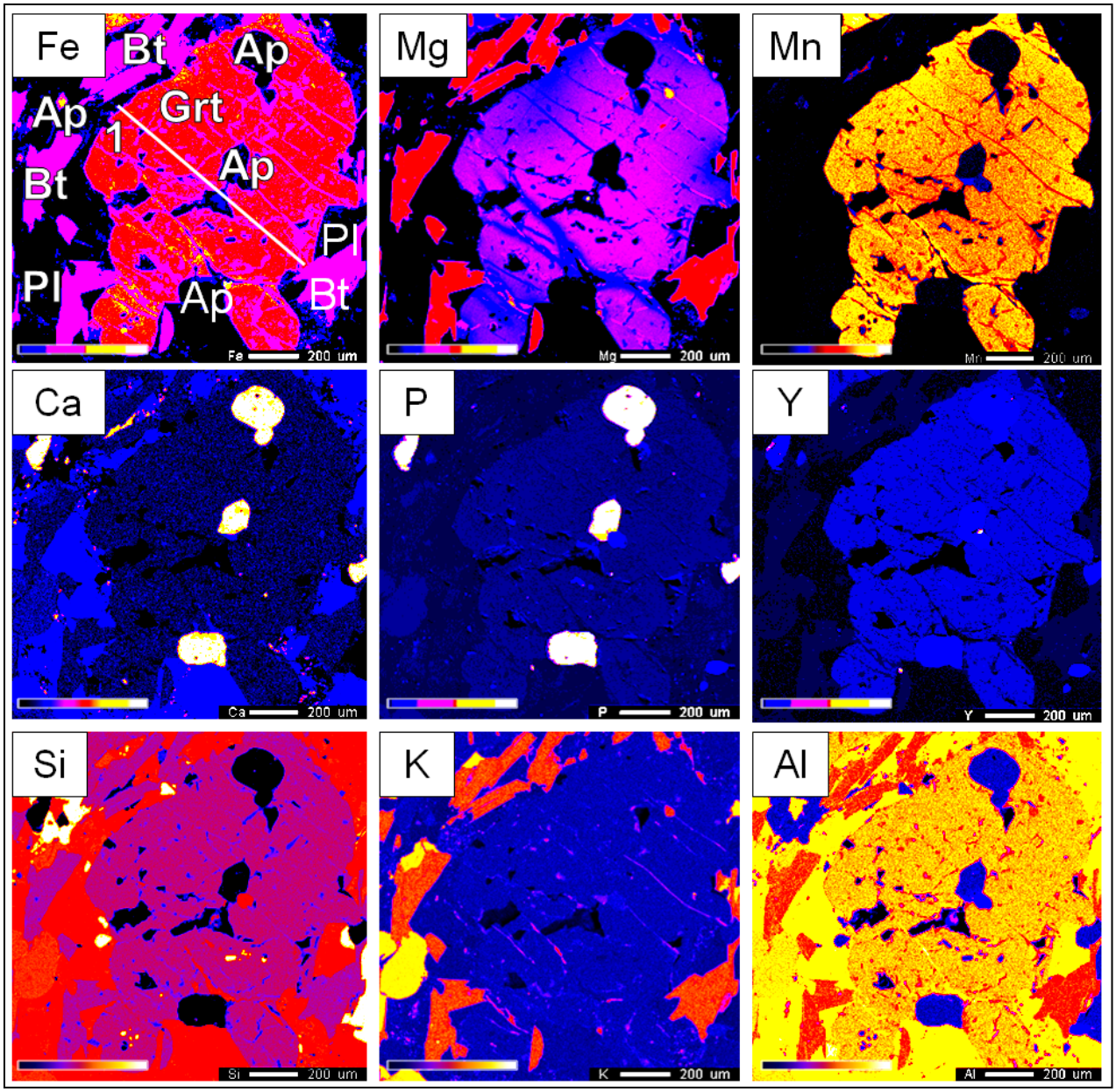

Figure A5: X-ray compositional maps for Fe, Mg, Mn, Si, Al, Ca, P, Y, K, and Ti in garnet RAC3-1 from bt-sil-grt gneiss, Suite 3. Mg map showing a slight decrease along the rim in contact with biotite whereas the Mn map shows a slight increase in Mn along the garnet rim in contact with biotite. A white line in the Fe map marks the locating of the zoning profile in Fig. 22. Mineral abbreviations are after Whitney and Evans (2010).

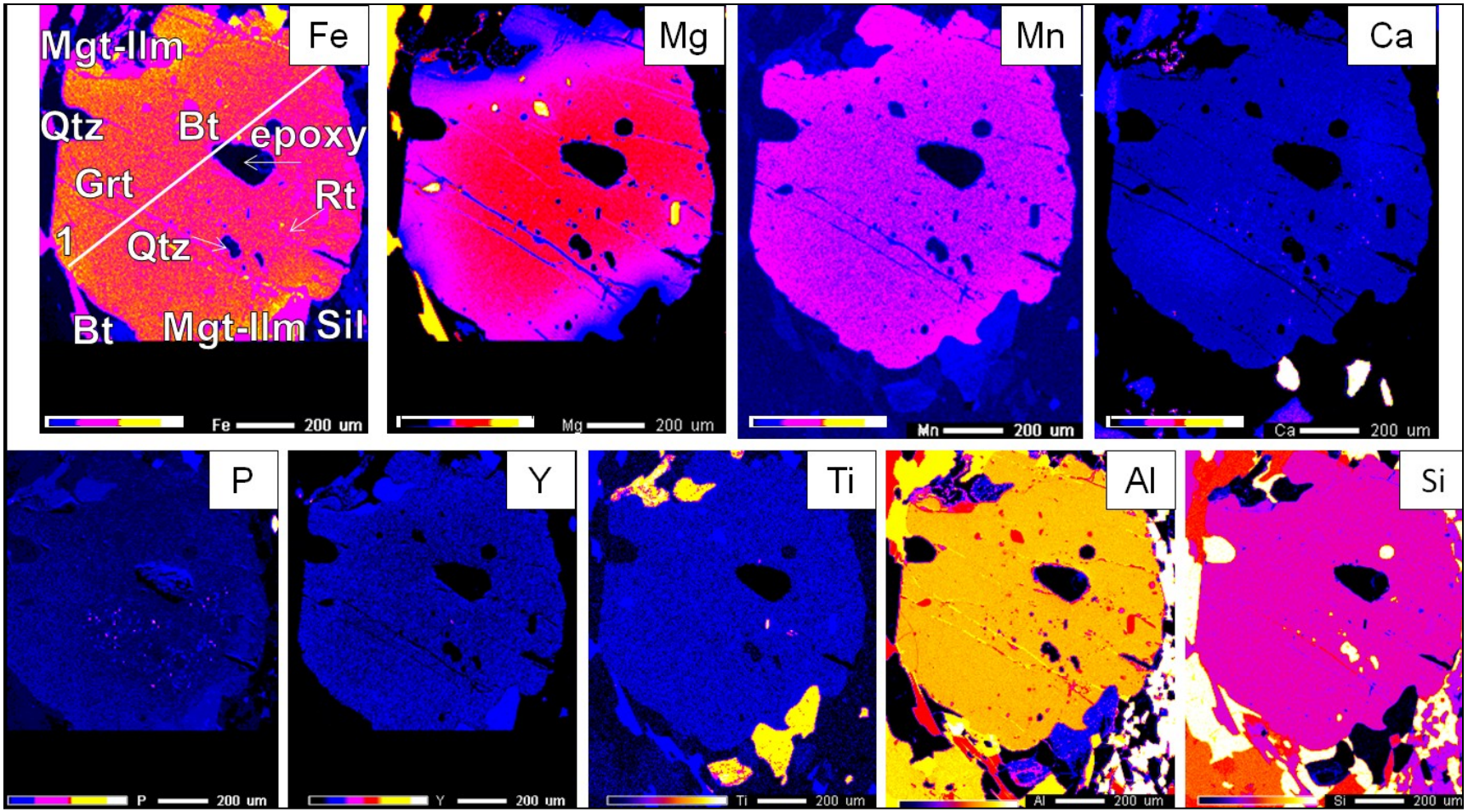

Figure A6: X-ray compositional maps for Fe, Mg, Mn, Si, Al, Ca, P, Y, K, and Ti in garnet RAC3-1 from bt-sil-grt gneiss, Suite 3. (b) Mg map showing a slight decrease along the rim in contact with biotite whereas the Mn map shows a slight increase in Mn along the garnet rim in contact with biotite. A white line in the Fe map marks the locating of the zoning profile in Fig. 22. Mineral abbreviations are after Whitney and Evans (2010).

APPENDIX II: TABLES

Table A1: Collected hand sample and thin section identification along with brief descriptions including UTM coordinates. *Samples were too coarse-grained for thin section analysis. Mineral abbreviations after Whitney and Evans (2010).

SUITE 1	**Section #**	**Sample #**	**Field Observation**	**18N-UTM E**	**18N-UTM N**
	RAC 23	12-06-09-1A	Quartz-Plagioclase- Kfs grey granodiorite leucosome (neosome) near amphibolite contact	399687	5084542
	RAC 22	12-06-09-1B	Quartz-Plagioclase- Kfs grey granodiorite leucosome (neosome) near amphibolite contact	399687	5084542
	RAC 21	12-06-09-1C	Quartz-Plagioclase- Kfs grey granodiorite leucosome (neosome) near amphibolite contact	399687	5084542
	RAC 20	12-06-09-1D	Quartz-Plagioclase- Kfs grey granodiorite leucosome (neosome) near amphibolite contact	399687	5084542
	*	08-07-09-1	Coarse-grained leucocratic diatexite pegmatite	399687	5084542
	8792	08-07-09-2	Mesosome- contact between leucosome and melanosome (amphibolite)	399687	5084542
	8793	08-07-09-3	Granitic leucosome (neosome)	399687	5084542
	8794	08-07-09-4	Amphibolite (melanosome)	399687	5084542
	RAC 6/ 9	08-07-09-5A/B	Tonalite	399687	5084542
SUITE 2	**Section #**	**Sample #**	**Field Observation**	**18N-UTM E**	**18N-UTM N**
	RAC 2	08-07-09-6	Granitic part of leucosome (neosome)	391554	5082687
	RAC 1	08-07-09-7	Mafic part of granitic neosome (melanosome)	391554	5082687
	*	08-07-09-8	Coarse grained Kfs-rich doming pegmatitic skarn (diatexite)	391554	5082687
SUITE 3	**Section #**	**Sample #**	**Field Observation**	**18N-UTM E**	**18N-UTM N**
	12695	12-06-09-5	Medium-grained grey granitic vein (leucosome)	394186	5085027
	RAC 18	12-06-09-6	Medium- to coarse-grained granitic migmatite (leucosome)	394186	5085027
	RAC 10	09-07-09-1A	Fine-grained Kfs-Grt granite (leucosome)	394186	5085027
	RAC 13	09-07-09-2	Medium-grained stromatic Grt-Bt-Sil gneiss- near contact between stromatic gneiss and Kfs gneiss (melanosome)	394186	5085027
	RAC 3	09-07-09-3aA	Medium-grained stromatic Grt-Bt-Sil gneiss (melanosome)- near contact with Kfs gneiss	394186	5085027
	RAC 8	09-07-09-3aB	Medium-grained stromatic Grt-Bt-Sil gneiss (melanosome)- near contact with Kfs gneiss	394186	5085027

Table A2: A suite of well characterized natural and synthetic (syn.) minerals and compounds were used as calibration standards for electron microprobe analysis.

Calibration Standards			
Element	**Line**	**Std.**	**Counting Time (peak-sec)**
P	Kα	syn. Gd phosphate	15
Ca	Kα	syn. REE glass Roedder	15
Pr	Lβ	syn. PrF_3	40
Fe	Kα	syn. Yittruim iron garnet	15
Y	Lα	syn. Yittruim iron garnet	30
Th	Mα	Th bearing Ca, Al, Si glass	30
Nd	Lβ	syn. $NdAlO_3$	40
Tb	Lβ	syn. Tb phosphate	60
Sr	Lα	syn. $SrTiO_3$	30
Ce	Lα	syn. REE glass Roedder	40
Sm	Lβ	syn. $SmAlO_3$	60
Eu	Lβ	syn. Eu phosphate	60
Si	Kα	syn. REE glass Roedder	15
La	Lα	syn. REE glass Roedder	40
Yb	Lα	syn. Yb phosphate	60
Gd	Lβ	syn. Gd phosphate	60
U	Mβ	syn. Brannerite	30
To	Lβ	syn. Ho phosphate	60
Er	Lα	syn. Er phosphate	60
Tm	Lβ	syn. Tm phosphate	60
Dy	Lβ	syn. Dy phosphate	60
Lu	Lβ	syn. Lu phosphate	60

Table A3: Quantitative analytical conditions for garnet compositional x-ray maps and garnet rim-to-rim traverses.

Type: Quantitative Analysis

EOS
Conditions

AccvL 20.0kV

Target Probe Current: 4.01e-008

WD: 11.122

WDS Element Conditions

No. Of Elements 11

	Elem-1	Elem-2	Elem-3	Elem-4	Elem-5	Elem-6	Elem-7	Elem-8	Elem-9	Elem-10	Elem-11
Elements	**K**	**Ca**	**Na**	**Al**	**Y**	**P**	**Ti**	**Fe**	**Mn**	**Mg**	**Si**
Xray name	Kα	Kα	Kα	Kα	Lα	Kα	Kα	Kα	Kα	Kα	Kα
Order	1	1	1	1	1	1	1	1	1	1	1
Channel	1	1	2	2	2	3	3	4	4	5	5
Crystal	PETJ	PETJ	TAP	TAP	TAP	PETJ	PETJ	LIFL	LIFL	TAP	TAP
Spc.Pos(mm)	119.619	107.358	129.499	90.519	69.826	197.184	87.975	134.192	145.704	107.511	77.454
Back(+)(mm)	3.000	3.000	3.000	3.000	1.300	3.000	3.000	3.000	3.000	3.000	3.000
Back(-)(mm)	3.000	3.000	3.000	3.000	1.500	3.000	3.000	3.000	3.000	3.000	2.000
Peak Seek W	1	1	1	1	1	1	1	1	2	1	1
Time/Count	Time	Time	Time	Time	Time	Time	Time	Time	Time	Time	Time
Mes.Time(sec)	20.0	10.0	10.0	10.0	20.0	20.0	10.0	10.0	10.0	10.0	20.0
Bac.Time(sec)	5.0	5.0	5.0	5.0	10.0	10.0	5.0	5.0	5.0	5.0	10.0
Mes.Count	10000	10000	10000	10000	10000	10000	10000	10000	10000	10000	10000
Bac.Count	500	500	500	500	500	500	500	500	500	500	500
PHA gain	16	16	32	32	16	64	64	32	32	8	32
High V. (V)	1700	1700	1662	1662	1612	1678	1664	1622	1622	1700	1676
Base L. (V)	2.50	3.00	0.70	0.70	0.70	0.70	0.70	0.70	0.70	0.50	0.70
Window (V)	7.50	7.00	9.30	9.30	9.30	9.30	9.30	9.30	9.30	9.50	9.30
Dif/Int	Int	Int	Diff	Diff	Diff	Int	Int	Int	Int	Diff	Diff
Sequence	1	2	1	2	3	1	2	1	2	1	2

Table A4: A suite of well characterized natural and synthetic (syn.) minerals and compounds were used as calibration standards for garnet electron microprobe analysis, University of Ottawa.

Standard Condition			
Element	Signal	Name	Meas
K	WDS	Sanidine	0016_STD
Ca	WDS	Diopside	0147_STD
Na	WDS	Albite	0019_STD
Al	WDS	Almandine2	0144_STD
Y	WDS	YIG	0044_STD
P	WDS	Apatite	0022_STD
Ti	WDS	Rutile	0017_STD
Fe	WDS	Almandine2	0144_STD
Mn	WDS	Tephroite	0081_STD
Mg	WDS	Almandine2	0144_STD
Si	WDS	Almandine2	0144_STD
Correction Condition			
Material:	Oxide		
Correction Method:	ZAF		
Valence Condition			
K(1) Ca(2) Na(1) Al(3) Y(3) P(5) Ti(4) Fe(2) Mn(2) Mg(2) Si(4) O(-2)			
Measurement Mode			
WDS-EDS Parallel			
Peak Search: none			
Background Measurement: Always			
Asyncronous Measurement			

Table A5: The following elements were measured using the following x-ray lines (lines), on the following standards where peak counting times were measured in seconds. (Scherrer 2008; Table 8)

Element	Line	Standard	Counting Time (peak-s)
Th	Mα	Th bearing Ca, Al, Si glass	50
U	Mβ	U bearing Ca, Al, Si glass	200
Pb	Mβ	$PbCrO_4$	200

Table A6: Periodically monazites of known ages were analyzed using the following standards from the authors listed above to ensure proper calibration of the microprobe during analyses.

Author	**Monazite Standard ID**	**Comments**
Stern & Berman (2000)	Mz1409 (1768 Ma) Mz2908 (1795 Ma)	Stern & Berman (Table 2, 2000)
Montel (1996)	557 Ma	called Suzuki in our analyses, should be called Montel- which is the Madagascar monazite, Fig 1(b) and Table 2

APPENDIX III: GARNET ELECTRON MICROPROBE DATA (CD-ROM)

Contents of enclosed CD-ROM:

The enclosed CD-ROM contains the quantitative analyses of the six garnets (RAC3-1, -2; RAC8-1, -2; and RAC13-1, -2) from the monazite-garnet quartz-monzonite (RAC3 & RAC8) and monazite-garnet monzonite (RAC13) thin sections using an automated 5 spectrometer JEOL 8230 SuperProbe electron microprobe by the wavelength dispersive X-ray analysis method (WDX), at the University of Ottawa. Results are presented in both weight percent (wt %) and atoms per formula unit (apfu). The red highlighted spot analyses represent inclusions which were omitted for the garnet compositional profiles (Figs. 20 to 22).